Universitat Jaume I

Escuela Superior de Tecnología y Ciencias Experimentales

Departamento de Física

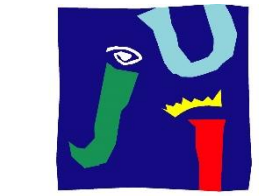

Optical microscopy techniques based on structured illumination and single-pixel detection.

PhD Thesis by

Ángel David Rodríguez Jiménez

Supervisors:

Dr. Jesús Lancis Sáez

Dr. Enrique Tajahuerce Romera

Castellón, Julio 2017

UNIVERSITAT JAUME·I

D. Jesús Lancis Sáez, Catedrático del área de Óptica de la Universidad Jaume I de Castellón, y D. Enrique Tajahuerce Romera, Profesor Titular de Óptica de la Universidad Jaume I de Castellón,

CERTIFICAN:

> Que la presente memoria "OPTICAL MICROSCOPY TECHNIQUES BASED ON STRUCTURED ILLUMINATION AND SINGLE-PIXEL DETECTION DETECTION", resume el trabajo realizado, bajo su dirección, por D. Ángel David Rodríguez Jiménez y constituye su Tesis para optar al Grado de Doctor.

Para que así conste, en cumplimiento de la legislación vigente, firman el presente certificado en Castellón, a dieciocho de julio de dos mil diecisiete.

Fdo.: Jesús Lancis Sáez Fdo.: Enrique Tajahuerce Romera

A mis padres y a mi hermana.

A Natalia.

“A book is made from a tree. It is an assemblage of flat, flexible parts (still called "leaves") imprinted with dark pigmented squiggles. One glance at it and you hear the voice of another person, perhaps someone dead for thousands of years. Across the millennia, the author is speaking, clearly and silently, inside your head, directly to you. Writing in perhaps the greatest of humans inventions, binding together people, citizens of distant epochs, who never new one another. Books break the shackles of time - proof that humans can work magic.”

Carl Sagan

Agradecimientos

7 meses pasaron desde el final de master y comienzo en la UJI. 7 meses preguntándome e imaginándome cómo serían los siguientes 4 años de mi vida en un nuevo grupo de investigación, en una nueva ciudad. Además de descansar, esos meses los empleé, entre otras cosas, en aprender chino (al menos todo el que la anatomía de la lengua de un murciano permite) y, cómo no, en ver series. Especial mención a los *11 días y 48 minutos* empleados en ver las 17 temporadas de *Stargate*. 4 años después puedo decir (y no es poco decir) que hubiera cambiado esas 17 temporadas por conoceros 7 meses antes.

En primer lugar, me gustaría agradecer enormemente a mis directores de tesis. A Jesús, por la confianza que depositó en mí desde el principio, ayudándome en todos los trámites necesarios para solicitar la ayuda predoctoral para la formación de personal investigador de la Universitat Jaume I, que finalmente conseguí. Muchas gracias por eso y por todo lo que vino después. Todos estos años, momentos y amistades se los debo a la oportunidad que me dio. A Enrique, por hacerme sentir en casa desde el primer momento y por hacer posible el llegar hasta aquí. Y aprovecho para agradecer también a Juanma, quien escribió las primeras líneas de esta historia, poniéndome en contacto con Jesús.

Un especial agradecimiento a Simón García, que ha sido mi mayor maestro y quien me enseñó a amar el universo y la ciencia, no como un simple instrumento, sino como una herramienta de progreso cultural y moral.

Gracias a mis primeros compañeros de despacho. Rocío, de las personas más agradables que he conocido. Siempre es un ejemplo a seguir. Jorge, por otro lado, es más de los *kurruki* (lo de Balsicas sigue pendiente, por cierto). Gracias también a Omel, Gladys y Lluis, con los que no sólo he compartido experiencia de laboratorio, sino también docencia. A Merche, por amenizar los almuerzos con comentarios sobre cine *indie* que debíamos evitar ver. A Vicente, con el cual me hubiera gustado compartir mucho más tiempo. Por cierto, muchas gracias por tus clases magistrales sobre *egiptología*. Y gracias, por supuesto, a Pere por todo lo que me ha ayudado a sacar adelante este trabajo. Gracias.

Thank you very much to Dr. Lei Tian for welcome me to his laboratory at Boston University. Thanks also to Waleed, Alex and Ling. It was an unforgettable experience. I hope we meet again soon.

Thank you Mahdi for all your dedication, your work, and for the typical Iranian food that you brought to us.

También dar las gracias a Humberto y Vero. Os deseo lo mejor para el futuro. A Omar, que trajo el *GOC* a nuestras vidas. A Yessenia, que siempre podrá contar conmigo para una foto de grupo. A Miguel, un tipo que es posible que haya estado en Burgos y puede hacer a pie la ruta UJI-Grao en 10 minutos. Cuando no esté, siéntete libre de poner la temperatura del aire acondicionado a tu gusto (a +3, imagino). A Carlos, embajador del glutamato en España. Siempre será mi fiel compañero en el equipo amarillo. A Eva, que me enseño su casa y la recreativa un año después de mudarse. Espero que disfrutes la *maquinita* durante muchos años. A Esther, aunque sé que se le olvidarán pronto estas palabras. Por cierto, ha sido un placer verte encontrar un nuevo uso a una de mis mayores fuentes de proteínas. De Fernando, qué decir. Hay pocas personas de las que haya aprendido tanto como de él. Además, siempre se preocupa de que no falte *Nesquick* en casa. Al dúo Eva-Fernando le tengo que agradecer también la integración en mi código fuente de conversaciones tales como:

—Pero… ¿es instantáneo? —preguntó Eva acerca del *Cola Cao* con curiosidad y cierta picaresca.

—¡Tú sí que eres instantánea! —contestó Fernando con tono de enfado.

Gracias a mis tíos, tías y primos que, aunque en estos años los he visto muchísimo menos de lo que me hubiera gustado, me han transmitido su cariño y apoyo constantemente. Nunca olvidaré la fiesta sorpresa de despedida que me hicisteis. Gracias también a Alex, Fina y José, por preocuparse siempre de cómo estoy y de acogerme siempre en su casa como a uno más de la familia.

A mis padres y a mi hermana, que siempre me han apoyado en todas mis decisiones y siempre están ahí cuando los necesito. El haber podido llegar hasta aquí es gracias a ellos. Por último, a Natalia. Ella es la voz de la

responsabilidad, la que me mantiene en la buena dirección, la que me pone los pies en la tierra, la luz que me guía.

Cuando estar cerca de los tuyos no es una opción, es cuando te das cuenta de lo que realmente importa en la vida. No sé dónde me llevará la siguiente etapa, pero sé que será en un lugar donde pueda estar con vosotros en cualquier momento.

CONTENTS

Acronyms List

APD	Avalanche photodetector
CCD	Charge-Coupled Devices
CDI	Coherent Diffractive Imaging
CLSM	Confocal Laser Scanning Microscopy
CMOS	Complementary Metal-Oxide-Semiconductor
CS	Compressive Sensing
DLP	Digital Light Processing
DMD	Digital Micromirror Device
DPM	Diffraction Phase Microscopy
EMCCD	Electron Multiplying Charge-Coupled Devices
FFT	Fast Fourier Transform
FLC	Ferroelectric Liquid Crystal
FOV	Field Of View
FP	Fourier Ptychography
FPM	Fourier Ptychography Microscopy
ISM	Image Scanning Microscopy
JPEG	Joint Photographic Experts Group
LC	Liquid Crystal
LCOS	Liquid Crystal On Silicon
NA	Numerical Aperture
NIR	Near-infrared
MEMS	Micro Electrical Mechanical System
MRI	Magnetic Resonance Imaging
PAM	Programmable Array Microscope
PD	Photodetector
PDA	Amplified Photodetector
PET	Positron Emission Tomography
PIE	Ptychographical Iterative Engine
PMT	Photomultiplier Tube
PNLC	Parallel Nematic Liquid Crystal
PSF	Point Spread Function
PSNR	Peak Signal-to-Noise Ratio
PTS	Photonic Time-Stretch
RGB	Red Green Blue
SH	Second Harmonic
SIF	Structured Illumination and Fourier filtering

SIM	Structured Illumination Microscopy
SLM	Spatial Light Modulator
SMLM	Single Molecule Localization Microscopy
SNR	Signal-to-Noise Ratio
SPFP	Single-pixel Fourier Ptychography
SPI	Single-pixel Imaging
SPM	Single-pixel Microscopy
STED	Stimulated Emission Depletion
STEAM	Serial Time-Encoded Amplified Microscopy
TNLC	Twisted Nematic Liquid Crystal
wDPM	White Light Diffraction Phase Microscopy

Chapter 1. Introduction

1.1 OPTICAL MICROSCOPY

Light is of paramount significance in industrial, artistic, scientific and medical settings and optical imaging is, perhaps, the oldest technique used to gather a wealth of information about our environment, our health, and our universe [1–3]. Within this context, optical microscopy is a fundamental tool in pathology imaging for medical diagnoses [4], in fundamental biology research, or in materials inspection in industrial manufacturing.

A compound microscope consists of a light source, a condenser lens, a sample to be imaged, an objective lens and an eyepiece. This basic design has been proved as highly robust and versatile. As a matter of fact, the vast majority of microscopy performed today still relies on these elements and, in particular, on the microscope objective lens used to image directly the sample. Like many other inventions in our days, the name of the inventor of the microscope is not clear, although the first compound microscope is attributed to Zacharias Janssen (1585-1632). The first microscopes were more a novelty gadget than a scientific tool due to the low magnification of around 9x and the images obtained had very poor quality. In the 17th century, Antonio Van Leeuwenhoek managed to manufacture lenses powerful enough (magnification of 270x) to observe bacteria, fungi, and protozoa, which he called "animalcules". He was the first to see and describe bacteria, yeast plants, and the circulation of blood cells in capillaries, among others. Later, Robert Hooke (1635-1703) discovered plant cells by observing a sheet of cork under the microscope, realizing that it was formed by small polyhedral cavities that reminded him the cells of a honeycomb. This is why each cavity was called a cell. He could not prove what these cells were the constituents of living things. What he was seeing were dead plant cells with their characteristic polygonal shape.

In spite of the great achievements of these first microscopes, they did not change much in 200 years due to strong limitations imposed by chromatic aberrations of the lenses. In 1850, the German engineer Carl Zeiss began to make improvements. In 1880, he hired a glass specialist, Otto Schott, who carried out investigations on lens crystals, greatly contributing to the improvement of the optical quality of the microscope. In addition, Ernst Abbe, also hired by Zeiss, contributed to the improvement of the construction of optical instruments. Abbe carried out theoretical studies of optical principles, for instance, discovering the resolution limit of the microscope. These studies demonstrated the importance of the theoretical study in microscopy.

Since then, many hardware advancements have been incorporated to the basic design, including additional optical components. Much of the innovation has been fostered by the exponential growth of pixel counts on charge coupled devices (CCD, Nobel Prize in 2009 [5]) or complimentary metal-oxide-semiconductor (CMOS) image sensors. Because of its optical sensitivity and molecular specificity, fluorescence microscopy [6] is employed in an increasing number of applications which, in turn, are continuously driving the development of advanced microscopy systems. In fluorescence microscopy the sample is illuminated with light of a specific wavelength which is absorbed by the fluorophores, causing them to emit light of longer wavelengths.

Confocal microscopes [7] have become widespread because they allow to handle three-dimensional (3D) information and visualize samples in deep positions within tissue from light emitted by differentially labelled fluorescent objects which are subsequently detected through multiple channels (see Figure 1.1) . Aimed to reject out of focus light, a pinhole, an aperture located in front of the detector, prevents the passage of the fluorescence signal from regions of the sample that are not in focus enabling optical sectioning; that is, the capability to get 2D slices of the 3D sample with high signal-to-noise ratio (SNR). Multiphoton microscopy imaging systems, such us two-photon excitation microscopy [8] achieve penetration

depths of up to a few millimeters at the expense of more sophisticated equipment based on femtosecond laser excitation.

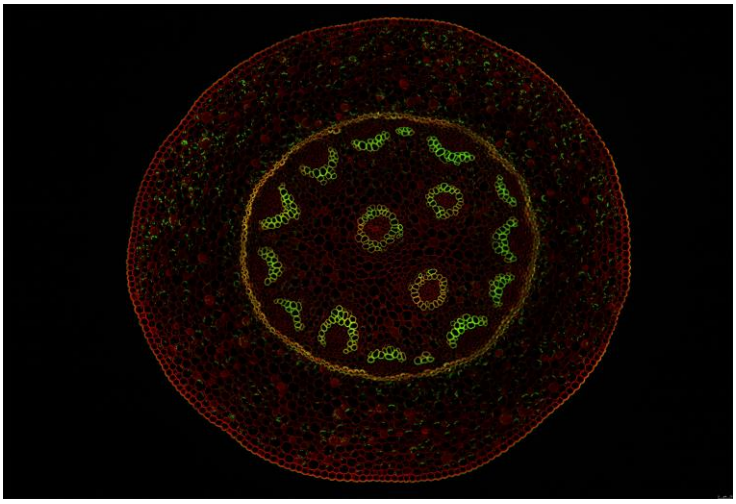

Figure 1.1. False color image of a plant stem obtained with confocal microscopy. Different colors represent different emission wavelengths produced by different excitation beams. Image obtained at the confocal microscope facility of the "Central Services of Scientific Research (SCIC)" at University Jaume I.

After four centuries since the invention of the microscope, the need to break frontiers is still a fact. The field of super-resolution microscopy, the so-called nanoscopy, was recognized in 2014 with the award of the Nobel Prize in Chemistry to the inventors of stimulated emission depletion microscopy (STED) [9–11] and single molecule localization microscopy (SMLM) [12,13]. The winners, Stefan Hell, William Moerner, and Eric Betzig, were among the first to recognize that the classical resolution barrier established by the works of Abbe can be overcome by different mechanisms that control the switching of fluorophores between "on" and "off" states.

In parallel with these developments, structured illumination microscopy (SIM) [14–18] was developed as an alternative method to achieve optical super-resolution and optical sectioning and today it has evolved into one of the most powerful and versatile microscopy techniques available. Here, limitations imposed by optical diffraction are overcome by encoding details corresponding to high spatial frequencies in the sample in low-frequency signals via spatial frequency mixing (see Figure 1.2).

Structured illumination is usually implemented either by projecting the image of a mask onto the sample, by making an image of the sample over the mask or through two-beam interference. In the first two cases, the masks can be created using a spatial light modulator (SLM), such as a digital micromirror device (DMD) or a liquid crystal on silicon (LCOS) display, whose operation will be discussed later. In the third case, two coherent beams (normally generated by a beam splitter or a grid) are made to interfere to form a sine wave. SLMs produce great benefits as opposed to interference methods, as they have an excellent ability to produce orientation changes and flexible structured lighting patterns, thus replacing the use of fixed grids and masks that have to be moved mechanically. By moving and rotating the illumination pattern in different positions and orientations, taking each time a wide-field image, a final image with roughly double the resolution of a conventional image alone is composed.

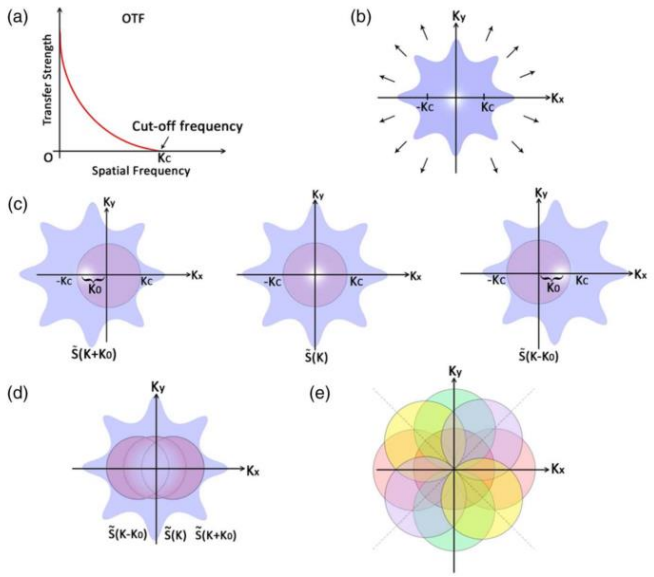

Figure 1.2. (a) Frequency spectrum of the point spread function (PSF) of the imaging system, (b) frequency spectrum of the object (arrows indicate the infinite extent of the spectrum), and (c) shifted frequency spectrum components of the object collected by the imaging system for a fringe pattern projected in one orientation. (d) The region mapped by the circles indicates the reconstructed frequency spectrum of the object after appropriately assembling the parts in (c). (e) Extended frequency spectrum of the object after assembling the similar parts in (d) for four different orientations of the projected fringe pattern. Extracted from [14].

Additionally to the improvement of the spatial resolution, there are a number of applications for studying dynamical phenomena that demand high frame rates. High-speed imaging is becoming increasingly important in microscopy because on the micrometric scale even slow-moving phenomena require high temporal resolutions. Light sheet microscopy [19,20] uses a thin plane of light to illuminate a sample orthogonally to the detection objective such that the axial resolution of the microscope is determined by the thickness of the light sheet. It allows fast volumetric imaging with reduced sample irradiation compared to conventional light microscopy methods. Also multifocal capture has been implemented to reach the millisecond time scale required to monitor the activity of neurons in the brain circuitry [21–23]. Another key application is in the field of flow cytometry where high-speed cameras are required. Within this realm, serial time-encoded amplified microscopy (STEAM) [24] has emerged as a new approach for imaging fast events.

1.2 PROGRAMMABLE OPTICS IN MICROSCOPY

With the availability of high-resolution SLMs new methods in optical microscopy have become feasible [25]. SLMs consist of hundreds of thousands of individual pixels defined by the individually addressable SLM pixel elements. Originally developed as display devices for video projection, high-resolution SLMs have been integrated into optical microscopes. They can be implemented to shape the illumination beam of the microscope to produce sophisticated illumination patterns as in SIM, as well as in the imaging path of the microscope.

Various devices are embraced by the term SLM. Liquid crystal SLMs can dynamically influence the amplitude and/or phase of light transmitted through or reflected from the panel [26]. Both amplitude and phase modulation arise from the birefringence of the liquid crystal. Amplitude modulation intrinsically originate from polarization modulation and are performed using a polarizer. For phase modulation, it has to be considered that the achievable phase retardation is in the range of 2π. Most

displays employ parallel aligned nematic (PN) or twisted nematic (TN) liquid crystal. Basically, pixel sizes are in the range of several microns over a panel with active area of the order of the squared centimeter and with response times of about 20 ms.

Placing an LCOS in a microscope gives one local control of the phase and amplitude of the optical beam. This allows to implement the wavefront shaping requirement demanded in adaptive optics to correct optical aberrations [27–29]. The corrections implemented by adaptive optics drastically improve the sharpness of the focus in optical microscopy [30]. By combining adaptive optics with confocal or multiphoton microscopy it is possible to improve imaging of thick specimens, especially at deeper locations [31,32]. In turbid materials, conventional imaging only works at a limited depth as the amount of ballistic signal decreases exponentially. The scattered light presents a background that reduces contrast. Rapid and label-free imaging at moderate depth is accomplished by gated imaging methods, such as the famous optical coherence tomography (OCT) [33,34]. Gated imaging methods selectively detect ballistic light by measuring the travel time of the light pulses. These methods are useful to a depth of about 10 mean free paths (typically 1mm), after which the diffuse light overwhelms the signal [35]. Adaptive optics typically uses a small number of degrees of freedom, on the order of 10-100, so that it can correct for aberrations but not for scattering. Also, LCOS have been successfully to implement wavefront shaping that uses hundreds of thousands of degrees of freedom to control scattered light [36–38].

On the other hand, the DMD is a micro-electrical-mechanical-system (MEMS) consisting of hundreds of thousands of tiny individually switchable mirrors with two stable mirror states [39,40]. The micromirrors can rotate about a hinge. Every micromirror is positioned over a CMOS memory cell. The angular position of a specific micromirror admits two possible states (+12 degrees and -12 degrees) depending on the binary state of the corresponding CMOS memory cell content. In this way, the light can be locally reflected at two angles depending on the signal applied to the

individual mirror. The mirrors are highly reflective and have higher refreshing speed and broader spectral response compared with ordinary liquid crystals. These features make DMDs attractive for many applications in microscopy.

DMDs have been applied in digital microscopy for different microscope configurations, including digital aperture control and dynamic illumination, spatial multiple-aperture scanning, and illumination pattern generation and detection [41–43]. A good example for improving luminous efficiency in comparison with the confocal microscope while maintaining optical sectioning capabilities using a structured illumination technique, is the programmable array microscope (PAM) [44] that uses a DMD to generate arbitrary patterns. Placing the DMD in the primary image plane of the optical system allows to use it in both illumination and collection stage (see Figure 1.3). This configuration permits only the backscattered light from the focal plane of the system to reach the camera, producing optical sectioning [45] in a similar way as the system based on rotating Nipkow disks [46,47].

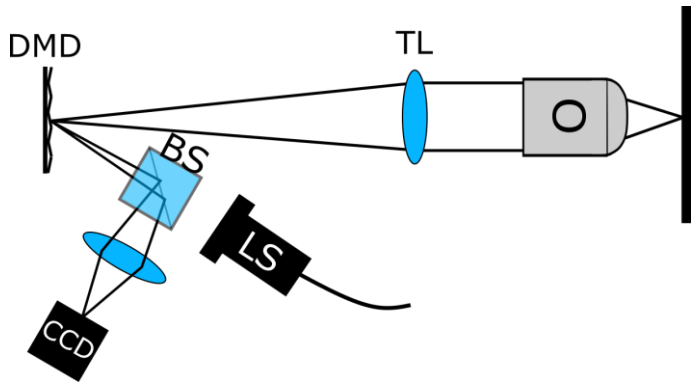

Figure 1.3. Diagram of PAM configuration. The DMD is placed in the primary image plane directing light to and from the object plane. (LS) Light source. (CCD) Camera. (BS) Beam splitter. (DMD) Digital micromirror device. (TL) Tube lens. (O) Objective.

1.3 COMPUTATIONAL TECHNIQUES IN OPTICAL MICROSCOPY

During the past decade, several unconventional methods of imaging have been developed that break the paradigm of direct imaging

with a lens. In computational approaches, the imaging system does not record a direct image of the sample, but rather raw data that must be computationally processed to recover an image. This computational techniques are aimed to address some of the limitations of conventional microscopes [48]. Lens-free holographic microscopes are designed to battle against the bulkiness and cost of the microscopy system [49].

Light-field microscopes [50], microscopes with active illumination control [51], and single-pixel based microscopes are examples of computational microscopes. Light-field microscopic imagers provide the capability to reconstruct 3D volumes of data via computational refocusing. Ptychographic Fourier microscopy projects a uniform plane-wave illumination, but one that comes from different well-defined angles with respect to the sample, to tackle the trade-off between spatial resolution and field-of-view (FOV) in conventional microscopy [52,53]. Ultimately, ptychography is aimed to increase the space-bandwidth product of the microscope [54].

The single-pixel imaging (SPI) scheme introduced in 2007 at Rice University [55] has gained considerable attention during the past few years thanks to the advent of spatial light modulators with intriguing features in terms of spatial resolution and frame speed. In SPI the complexity to retrieve the spatial information of a sample is shifted away from the design of an array of light sensors on to the spatial light modulator enabling the use of practically any kind of bucket (single-photosensor) detector. In this sense, SPI is closely related to different computational imaging technologies like ghost imaging [56,57] or dual photography [58]. Hyperspectral imaging [59,60], polarimetric imaging [61], temporal imaging [62], or time-of-flight imaging [63,64] are some typical examples of technologies that benefit from the above idea. Applications fields range from optical encryption [65] to 3D imaging [66,67], ophthalmology [68], infrared microscopy [69], microfluidics microscopy [70] or terahertz [71] and X-ray imaging [72].

In short, in SPI a set of masks are optically projected onto the sample and the whole intensity is collected onto a bucket sensor.

Measurements are sequential by change of the spatial mask. If many different masks are used, their shapes and the intensity signals are combined to retrieve the sample. To battle against the intrinsic limitation in frame speed imposed by sequential masking, single-pixel cameras acknowledge fast spatial light modulators, such as the DMD, to codify the projecting masks. DMDs permit highly flexible codification of binary masks at frame rates above 20 kHz and enable single-pixel video applications. Also, ultrafast pattern generation has been demonstrated through spectral pulse shaping based on photonic time-stretch (PTS) and wavelength-to-space conversion [73]. Alternatively, the use of a diffuser to generate speckle patterns enables to sample the object in one-shot but at the expense of a tedious calibration procedure [74].

Finally, given some reasonable assumption about the sparsity of the object, the use of smart sensing strategies based on compressive [75,76] or adaptive sensing [77–79] makes it possible to get rid off the measurement of the full-length signal to save time. Compressive sensing (CS) has triggered a major revolution in the omnipresent information theory outlined in the seminal paper by Claude E. Shannon, "*A Mathematical Theory of Communication*" published in the *Bell System Technical Journal* as early as 1948. CS consists of sampling a sparse signal at low rate and later using computational power for the exact reconstruction of the signal, so that only the necessary information is measured. CS allows one to acquire less data though still recover the same amount of information as traditional techniques, meaning less resources such as time, detector cost, power, data processing, and storage. The idea is that, for natural scenes, many of the measurements provide little to no useful information. A striking consequence of this fact in everyday's world is the ability of consumer cameras with several megapixel detectors to routinely reduce the number of bits in a raw data file by one or two order of magnitude without substantial information lost. To quote David Brady: "*if it is possible to compress measured data, one might argue that too many measurements were taken*". From a sampling perspective this implies that we may be able to acquire a signal with fewer measurements, usually 10% of the measurements required by the Nyquist sampling rate [75,80,81]. CS

applications extend well beyond imaging and include computed tomography, electrocardiography, seismology, analog-to-digital conversion, radar, astronomy, DNA sequencing, and genotyping (Rice Compressed Sensing Resources; http://dsp.rice.edu/cs).

1.4 MOTIVATION FOR THE THESIS WORK

In microscopy, it is possible to distinguish different kinds of imaging approaches in terms of their excitation and detection modalities (see Table 1.1). On the one hand, in wide-field microscopy, a large sample area is illuminated and light is spread over an array of photosensors mounted onto a digital platform, like the CCD or the CMOS sensor. In contrast, in raster scan microscopy, a light spot is scanned through the sample and a single photosensor is used to detect the signal on a pixel-wise manner. Also, in image scanning microscopy (ISM) the point detector in a conventional confocal microscope is replaced with a detector array to increase the extremely low SNR [48,82].

The single-pixel imaging (SPI) scheme [83] has proved to be a very effective sensing mechanism and has triggered diverse applications where conventional cameras equipped with millions of pixels fail to give an adequate response, including optical microscopy. In single-pixel microscopy (SPM), the sample is excited with a patterned illumination projected through the objective lens and the signal is collected on a single photosensor [69,70,84–90]. The images are computationally reconstructed from the photocurrents corresponding to a set of appropriately chosen patterns. SPM has allowed hyperspectral imaging across the visible spectrum in a fluorescence microscope and imaging of microfluids [60,70]. Also, a prototype microscope system based on SPI to image simultaneously in the visible and the short-wave infrared has been recently demonstrated [69]. Moreover, wavelength plays an important role in biological imaging. For instance, wavelengths located in the near-infrared have their maximum depth of penetration in biological tissue. This window, also known as therapeutic window or near-infrared (NIR window) is

primarily limited by the light absorption of blood at shorter wavelengths and water at longer wavelengths.

		Excitation	
		Wide-field	**Pixel-wise**
Detection	**Array of detectors**	Wide-field microscopy	Image scanning microscopy
	Single-pixel	**Single-pixel microscopy**	Raster scan microscopy

Table 1.1. Classification of microscopy modalities attending to illumination and detection settings.

In this thesis, we explore SPM to design and develop proof-of-principle experiments where the single-pixel detection strategy outperforms conventional optical array detection in wide-field microscopy. The ability of the single-pixel detection strategy to generate a spatially resolved image of an object hidden by arbitrary scattering media has been recently demonstrated. Strikingly, a sensor without spatial resolution is able to retrieve a high-resolution image of a sample hidden by a turbid media, a problem that cannot be solved with conventional CCD or CMOS cameras equipped with millions of pixels. In this way, we fix the fundamental trade-off between penetration depth, sensitivity and imaging speed of current microscopes by a shift in the paradigm of the detection strategy.

Also, we develop the counterpart for single-pixel imaging of Fourier ptychography. This method is a clever combination of phase retrieval and synthetic aperture techniques. In this method, an array of LEDs is placed in a relatively far position from the object, which illuminates sequentially the object from different angles and a low NA objective is used to image the object on to a camera. As the distance of the LEDs is assumed far enough from the object, the illumination of each LED can be regarded as a tilted plane wave with a different angle. These tilted plane waves will cause a shift in the spectrum of the object in Fourier domain. So, each captured image will carry information from different

areas of the Fourier spectrum of the object. By using an iterative algorithm, similar to those used in phase retrieval, it is possible to combine the information from these areas all together and get a high-resolution image with a large FOV at the same time. In addition to high resolution and large FOV, the method provides the phase distribution of the object.

The structure of the Thesis is the following:

I. In **Chapter 2** we introduce the basic concepts and mathematical tools for understanding SPI and CS, analysing the main differences between conventional and single-pixel cameras. Also, we review the main features of the different spatial light modulators and photodetectors used to build our SPM. Then, in **Chapter 3**, we describe the SPM and perform a detailed analysis of the spatial resolution, both in the transversal and in the axial coordinates, using Fourier optics.

II. In **Chapter 4** we demonstrate a dual-mode microscope that can image specimens both in reflection and transmission modes simultaneously. The majority of optical microscope designs make the simultaneous imaging of a sample in transmitted and reflected modes inefficient, restrictive, or even impossible. Here, we demonstrate that the SPM architecture is particularly well-fitted for this dual operation, as both images belong, unequivocally, to the same plane of the sample. Further, the system is based on the use of an off-the-shelf DMD from a cost-effective digital light processing projector that utilizes an offset diamond pixel layout. To this end we demonstrate an algorithm to precisely allocate pixels in memory to deal with geometrical artifacts generated by the diamond layout.

III. In **Chapter 5**, we extend the capabilities of raster scanning and SPI by combining those techniques with adapted Fourier ptychography algorithms in a single-pixel microscope working in transmission. In these experiments, we virtually extend the numerical aperture of the system by using an array of photodetectors placed in the Fraunhofer

plane. Finally, in **Chapter 6** we summarize the main conclusions of this doctoral thesis and outline the main avenues for future work.

Chapter 2. Single-pixel imaging and compressive sensing

As we discussed in section 1.3, despite ongoing improvements in optical array detector technologies such as charge-coupled devices (CCDs) or electron multiplying charge-coupled devices (EMCCDs), single-pixel imaging (SPI) has gained considerable attention in the last years. SPI has triggered diverse applications where conventional cameras equipped with millions of pixels fail to give an adequate response, including optical microscopy. For instance, point scanning techniques, which work with single-pixel detectors, provide the method of choice in several imaging devices as, for instance, in confocal or multiphoton microscopy [7,91].

In this chapter, we describe imaging as a sampling process and how this is carried out in a conventional camera. Then, we describe the raster scanning technique and introduce the concept of image multiplexing used in single-pixel cameras. Next, we list the devices that allow to perform experimentally single-pixel imaging and in what situations is more suitable to use one or other according to their properties. Finally, we describe the mathematical principles of compressive sensing.

2.1 SINGLE-PIXEL IMAGING

The word "sampling" refers to both the process of obtaining discrete measurements of a signal and the representation of a signal using discrete numbers [92]. A digital image given by a conventional camera is the result of a sampling process because it is a representation of the light distribution at the object scene by discrete numbers at discrete coordinates [93]. These numbers are normalized values of irradiance in the

pixels of the camera. In digital image processing it is usual to consider the 2D image as a 1D vector, which expresses the set of rows of an image concatenated in a single vector. Thus, if we consider the two-dimensional object as a column vector O which contains N components of the object, the sampling done by the camera can be expressed as

$$Y = P \cdot O = \begin{pmatrix} f_i^T \\ \vdots \\ f_N^T \end{pmatrix} \cdot \begin{pmatrix} O_1 \\ \vdots \\ O_N \end{pmatrix}, \tag{2.1}$$

where each row of P is a vector of the basis $\mathcal{N} \equiv \{f_i\}_{i=1}^{N}$ and Y is a column vector containing the projections of the object on each vector of the basis. The problem of estimating O from equation (2.1) is called inverse problem and can be addressed with different mathematical techniques, for example, by a simple matrix inversion operation, $O = P^{-1}Y$. For the particular case where a camera is used, P is the identity matrix.

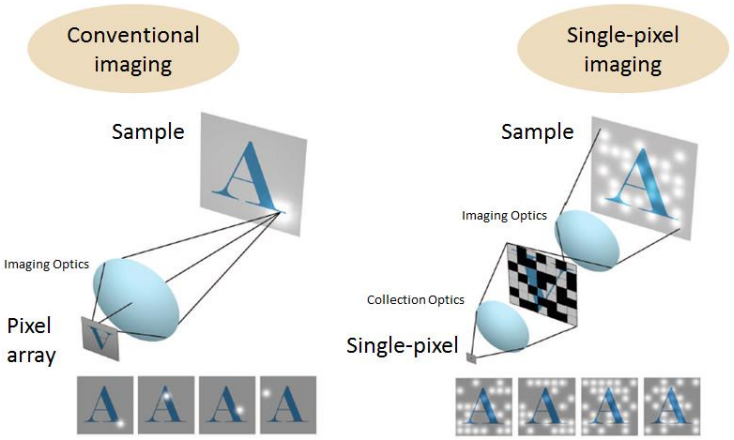

Figure 2.1 Comparison between conventional imaging (left) and single-pixel imaging (right). Extracted from [94].

When the camera starts operating, the irradiance is measured in all the pixels at the same time, that is, the sampling of the object is performed in one shot. However, it is possible to acquire the information following a sequential process with just a single-pixel detector. One way is by raster scanning, by measuring the irradiance produced by each local area of the object one by one. This method would be equivalent to activate only one

pixel of the camera in each measurement. Another approach for single-pixel imaging, usually the one named single-pixel camera, consist on illuminating the object with microstructured light patterns or imaging the object onto a test mask. In this case, all the intensity transmitted or reflected through the mask pattern is integrated by a photodetector. Measurements are again sequential, by changing the illumination patterns. But now each one gathers global information from the sample. This represents an advantage in terms of signal-to-noise ratio. A comparison between conventional imaging and single-pixel imaging schemes is shown in Figure 2.1 [94].

The projection of an object onto a set of functions can be performed experimentally by using a SLM. This device allows encoding a set of functions (P) while a single-pixel detector measures the projections of the object (Y) onto that set of functions. In our experiments, Walsh-Hadamard functions are chosen as the projection basis (see Annex).

2.2 PATTERN CODIFICATION DEVICES

In contrast to conventional cameras, in which spatial information is given by the 2D structure of the pixelated array, in single-pixel systems, spatial information is shifted to the illumination stage. The devices most commonly used to encode spatial information in the illumination stage are spatial light modulators based on liquid crystal on silicon technology (LCOS) and spatial light modulators based on controllable micromirrors (DMD). Most of these technologies were developed for industries such as consumer electronics for TV and movie projectors, making them very affordable nowadays.

2.2.1 Liquid crystal on silicon

The use of SLMs based on liquid crystals has expanded significantly in recent years, particularly in the field of optics [26]. They are frequently used in applications such as coding of diffractive optical elements for signal processing and optical tweezers [95–98], optical microscopy [25], digital holography [99], pulse shaping [100,101],

generation of polarization patterns [102,103], and adaptive optics for focusing radiation through scattering media [36,38,104], among others.

The ability of LCOS to modulate phase is given by the physical properties of liquid crystal molecules. Liquid crystal materials have several common characteristics such as rod-like molecular structure, rigidness of the long axis, and strong dipoles and/or easily polarizable substituents. The orientation of liquid crystal molecules can be manipulated with mechanical, magnetic or electric forces. These crystals are optically anisotropic and behave as uniaxial birefringent media. These properties result in the material having two main refraction indices, ordinary and extraordinary.

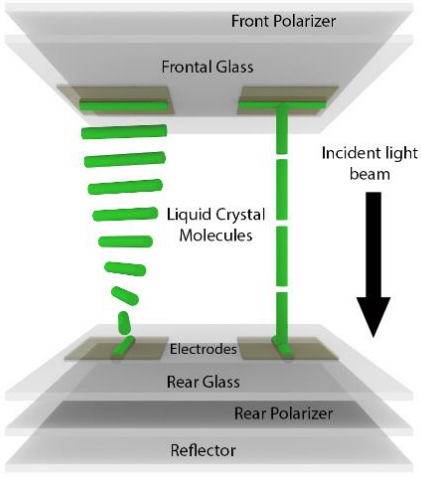

Figure 2.2. Operation of a classic cell TNLC molecular twist of 90º as binary amplitude modulator with two possible states, reflection (left) and absorption (right).

Liquid crystal light modulators can be constructed in several ways, resulting in different types of displays. The most common are PNLC (*Parallel Nematic Liquid Crystal*), TNLC (*Twisted Nematic Liquid Crystal*), and FLC (Ferroelectric Liquid Crystal). PNLC and TNLC have frame rates under 180Hz while FLC SLMs allow higher reflectivity and frame-rate (≈ 1kHz) working as binary amplitude or phase modulators. In Figure 2.2, the operation of two TNLC cells is shown. When no electric field is applied to the liquid crystal molecule, the cells are oriented helically (left side). Then, if an electric field is applied perpendicular to the substrate

glass, liquid crystal molecules tend to align in this direction (right side). By this way, it is possible to control the birefringence of these material by an external electric field, and therefore to control the phase delay of light traveling through them.

It must be taken into account that, in order to use liquid crystal devices to modulate phase or amplitude, linear polarizers, and frequently retarder wave plates, have to be used in combination with the liquid crystal cells. This can lead to a notable loss of efficiency, particularly when the light source is not linearly polarized by nature. A mathematical description of the SLM used in this work can be found in Reference [105], where the effects of diattenuation, retardance and depolarization are explained in detail. In order to obtain an amplitude modulation the input and output polarizers must be oriented parallel to the input and output director axis, respectively. Once this configuration is set, it is necessary to calculate the operating curve to calibrate the intensity output for each voltage applied to the liquid crystal molecules. In many cases, the manufacturer provides this operating curve, also called look-up-table.

2.2.2 Digital micromirror devices

A digital micromirror device is a pixelated screen in which each pixel is composed of a mirror capable of switching between two states of ± 12 degrees. If the DMD display is illuminated with a light source, the two different positions of the micromirrors work as ON/OFF states. The high frame rate of these devices is capable of changing the state of each mirror at frequencies of 22 kHz.

Extensive applications of the DMD to microscopy have been reported in the past few years, including conventional structured illumination microscopy with fringe projection [106], super-resolution and optical sectioning microscopy [41,107] and programmable array microscopes [44,45,108]. Furthermore, fast DMD and pattern illumination is at the core of optogenetics, a tool for noninvasive activation and silencing of neurons and muscles [109].

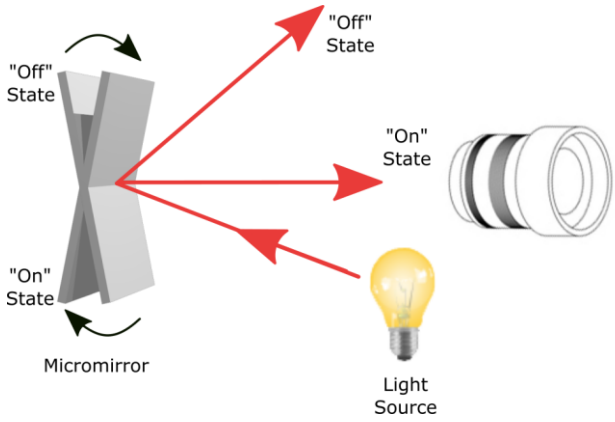

Figure 2.3. Schematic view of the two controllable states of a DMD micromirror.

DMDs can be divided in two categories, commercial grade and scientific grade, although their operation principle is the same. Commercial grade DMDs are regular video projectors devices created for consumer electronics. They work only at video rates (60-120 Hz for color RGB images). On the other hand, scientific grade DMDs are devices created to achieve professional performance and used for scientific and engineering applications. They have higher resolution and higher refreshing rates, up to 22.7 kHz. However, they are complex to control and more expensive. Their simplicity and lower price make commercial DMDs very interesting for certain applications.

2.3 DETECTION DEVICES

As we already mentioned, the fundamental reason why the bucket detection strategy can outperform conventional optical array detection is the use of a single channel detector that simultaneously integrates all the photons transmitted or reflected by the sampled scene. In addition, in general, for each measurement half of the available light on average is used, which leads to an improvement in the signal-to-noise ratio compared to systems such as raster scanning in which only one point of the scene is illuminated in each measurement (Fellgett's advantage). This makes this technique very suitable for experiments with low light levels. This approach

has been demonstrated to work at sub-picowatt light levels by using photomultiplier tubes and Geiger-mode avalanche photodiodes that provide shot-noise limited detection [110]. Another main difference between the serial scanning and global illumination approaches is related to the temporal resolution. Serial excitation is mainly limited by the dwell time at a given position, that is, the time needed to induce a detectable response in the detector. However, in global illumination schemes, due to the increase of the global intensity, the dwell time is significantly reduced. Consequently, in these systems, the total acquisition time is not limited by the dwell time but by the speed at which patterns can be projected. If a DMD is used as SLM, it is possible to arrive to fast refreshing rates as high as tens of kilohertz. The multiplex advantage in single-pixel cameras has been successfully employed to acquire in less than 1 minute the collection of chemical images in multivariate hyperspectral Raman imaging [111]. This represents a speed advantage of the order of 100.

The choice between different single-pixel detectors depends on the application. Next we make a brief comparison of the main characteristics of photodiodes (PDs) and photomultipliers tubes (PMTs) taking into account properties of different commercial models. We discuss the main features of each of them and the reasons for choosing one instead of another, taking into account experimental conditions.

Figure 2.4. Si biased detector model DET36A from Thorlabs, Inc.

Photodiodes. A silicon photodiode is a solid-state device which converts incident light into an electric current. When photons of energy

greater than the bandgap of silicon reach the detector, they are absorbed and electron-hole pairs are created. Silicon photodiodes are typically sensitive to light in the spectral range from about 200 nm (UV) to 1100 nm (near IR). Another biased PDs, non-silicon-based (such as GaP, Ge, and InGaAs detectors), can extend the spectral wavelength range from the UV to the mid-IR (150 nm to 2.6 µm). Amplified photodiodes (PDA) have the same properties we just mentioned plus a gain factor. The photocurrent generated by a PD is calculated as $I_{PD} = P \cdot R_\lambda$, where P is the incident power and R_λ the responsivity as a function of the wavelength, λ, while the photocurrent generated by an amplified PD is $I_{PDA} = G \cdot P \cdot R_\lambda$ where G is the gain factor that can go from 1 to 100. However, if more gain is needed, avalanche photodiodes (APD) can be used. From a functional point of view, they can be regarded as the semiconductor analog to photomultipliers. APDs show an internal current gain effect (around 100) due to impact ionization (avalanche effect). However, some silicon APDs employ alternative doping and beveling techniques compared to traditional APDs that allow greater voltage to be applied before breakdown is reached and hence a greater operating gain ($\approx$ 1000).

Photomultiplier modules. The development of photomultipliers (PMT) [112] was a consequence of the first studies of secondary emission. The use of secondary emission as a means for signal amplification was proposed in 1919 (U.S. Patent 1, 450, 265, April 3, 1923). In 1935, the first single-stage photomultiplier was developed [113]. Because of its better frequency response, the single-stage photomultiplier was intended for replacement of the gas-filled phototube as a sound pickup for movies. Despite its advantages, it saw only a brief developmental sales activity before it became obsolete. One year later, the multistage photomultiplier was reported [114]. This tube used a combination of electrostatic and magnetic fields to direct electrons from stage to stage. Although the magnetic-type photomultiplier provided high gain, it presented several problems. Fine adjustment of the magnetic field was critical, and to change the gain by reducing the applied voltage, the magnetic field also had to be adjusted. The dark current was another problem of these devices. For these reasons, and because of the development of electrostatically focused

photomultipliers, commercialization did not follow. The first commercially successful photomultiplier was described by Zworykin and Rajchman [115]. The Rajchmann design with some modifications eventually was, and still is, used in photomultipliers, particularly for high-gain wide-bandwidth requirements.

Early applications of the photomultiplier tube were in astronomy and spectroscopy. Because the actual quantum efficiency of the photomultiplier was at least ten times that of photographic film, astronomers quickly realized the advantages of PMTs. Furthermore, because the output current of the photomultiplier is linear with incident radiation power, the tube could be used directly in photometric and spectrophotometric astronomy. Today, the PMT is an essential tool for research in many fields, including analytical chemistry, particle physics, medical imaging, industrial process control, astronomy, and atomic and molecular physics.

Figure 2.5. . Photomultiplier tube model PMM01 from Thorlabs, Inc. Courtesy of Y. Jauregui Sánchez.

Spectral response. Photomultiplier tubes can be obtained with good spectral sensitivity in the range 185 to 920 nm. Silicon cells have a spectral response going from 200 to 1100 nm although the response below 400 nm is less than 10%. However, non-silicon based photodiodes, such as extended InGaAs detectors, allow responses up to 2.6 μm. In general, then,

the photomultiplier tube is to be preferred for applications involving shorter wavelengths, although other factors may override this consideration.

Temporal response. Photomultipliers are available with rise times (10 to 90%) of 1 or 2 ns using a 50Ω load. The inherent rise time of silicon cells may be in the range 1 to 43 ns, depending upon the area of the cell. However, because of the cell's capacitance, the effective rise time is much longer depending upon the choice of load resistance. For example, with a 1MΩ load resistance, the rise time may be of the order of 20 μs. Silicon avalanche photodiodes can have rise times as short as 2 nanoseconds. In general, if a fast temporal response is needed, PMTs and APDs are a good choice. Furthermore, if the amount of light is good enough, a silicon PD with a small cell area can be used.

Signal-to-noise ratio. At very low light levels, the limitation of detection and measurement is generally given by the signal-to-noise ratio. For a photomultiplier tube such as one used for spectroscopy, the noise equivalent power (NEP), which is the power level into the device which provides a signal level just equal to the noise level, at room temperature, at 400 nm, is about $7x10^{-16}$ watts while for a silicon photocell, the NEP at 900 nm is about $2x10^{-13}$ watts. Thus, the photomultiplier is clearly superior in this category. Also it should be pointed out that the silicon diode must be coupled into a load resistance of about 5 MΩ in order to avoid noise domination from the coupling resistor, increasing its rise time to about 100μs. So it is clear in this point that, if the signal-to-noise ratio has to be improved, the photomultiplier is the most suitable option.

Gain. Like a photodiode (amplified photodiode), a photomultiplier tube can have a gain factor, by which the fundamental photocathode signal is multiplied. The gain of a PMT can go from 10^3 to 10^8 while silicon PDA have a gain of about 100 and APD can go up to 1000. Therefore, if the experimental conditions demand a higher gain, an intermediate solution would be the use of an APD and an extreme solution, the use of a PMT.

Dynamic range. One of the key points in a SPI detector is its ability to distinguish differences in intensity levels between measures of different

projections. Depending on the experimental conditions these differences between intensity levels can be very low. Although for experiments with very low light levels, the use of a PMT may be that the only option, it must be taken into account that the dynamic range of a PD is two orders of magnitude higher [116], being more convenient to use the latter if the light conditions allow it.

2.4 COMPRESSIVE SENSING

The technique of image multiplexing requires time to acquire data, which represents one of its major limitations. A current single-pixel camera milestone is to reduce measurement times to values comparable to conventional cameras. The approaches to achieving this are two: the use of faster devices (detectors and modulators) and to reduce the total number of projections. The time needed for acquire one image using image multiplexing can be calculated as follows:

$$t_s = Nt_R + (N-1)\cdot {}^{1}/_{R_e} \cong N(t_R + {}^{1}/_{R_e}) \qquad (2.3)$$

where N is the number of projections, t_R is the response time of the detection device and R_e is the refresh rate of the SLM. For detection devices such as PD and PMT, $1/R_e \gg t_R$, that is, the response time of the detectors is much faster than the time needed for the SLM to change the projection pattern. Then, the bottle-neck of the technique is the speed of the SLM, R_e. To reconstruct an uncompressed image, it is necessary to send a number of patterns equal to the number of pixels of the final image. As is shown in Table 2.1., at the speed of current SLMs, to acquire an image of 64x64 pixels, the shortest time that can be achieved is 200 ms per image, this is, 5 fps. This can be achieved when using a scientific grade DMD at 22.7 kHz, allowing single-pixel video applications [117,118].

Image size (pixels)	LCOS-SLM (60Hz)	DMD (22,7kHz)
64x64	70 s	200 ms
512x512	70 min	10 s

Table 2.1. Time needed for projecting the full set of test patterns as a function of the type of SLM and image size.

The techniques for image compression consist of representing these images on a different basis than the *natural* one. An image can be compressed if it can be expressed on a basis with only a small number of coefficients, less than the dimension of the image, without substantial loss of information. Then it is said that the image is sparse on this basis. Taking this into account, compressive sensing explores the estimation of sparse images by compressing the signal in the sensing stage, rather than in the storage stage.

One of the benefits of single-pixel imaging is that it can take advantage of the compressive sensing approaches, allowing to reduce the number of sent patterns without a substantial loss of quality or resolution. Let us suppose that an N-pixel image has only k non-zero significant coefficients in a given basis (we suppose the image is sparse in that particular basis). CS proposes that an M-random subset of coefficients of the image contains enough information for an accurate image reconstruction [76]. CS asserts the image can be retrieved if $M \geq k \log N$, overcoming the Nyquist sample rate and achieving a compression ratio of $CR = N/M$. The range of applications of CS is very wide, covering such different areas as analog-to-information conversion [119,120], computational biology [121,122], analysis of geophysical data [123,124], radar [125,126], astronomy [127,128], communications [129,130], surface metrology [131], remote sensing [132,133], computer engineering [134], graphics [58], robotics [135], neuroscience [136], quantum physics [137,138], and medicine [139,140].

The set of measurements obtained by projecting the object O, expressed in some basis $\Phi \equiv \{\phi\}_{i=1}^{N}$ on a specific set of functions can be written as [93]

$$Y = \mathcal{S} \cdot O_{\Phi}, \tag{2.4}$$

where each row of the $measurement\ matrix\ \mathcal{S}$ corresponds to a function of the set. Later we will see how to design the $measurement\ matrix$ to recover the image. If Ψ is the basis where the image is sparse, considering the relationship between both representations, $O_{\Phi} \equiv M_{\Phi}^{\Psi} O_{\Psi}$, equation (2.4) can be written as

$$Y = \mathcal{S} \cdot M_{\Phi}^{\Psi} \cdot O_{\Psi} = \Theta \cdot O_{\Psi}, \tag{2.5}$$

where $\Theta = \mathcal{S} \cdot M_{\Phi}^{\Psi}$ is called $detection\ matrix$.

When the number of measurements is less than the size of the image, the system of equations (2.5) is compatible undetermined and has infinite solutions. The theory of optimization solves these problems by using convex optimization algorithms.

The theory of CS requires: 1) to design a $measurement\ matrix$ $\mathcal{S}$; and 2) to ensure that the optimization problem has a high probability of a single solution. To guarantee the reconstruction of the image three requirements have to be fulfilled [141]: that the image is sparse in the basis Ψ, that the $measurement\ matrix\ \mathcal{S}$ is random, and that basis Φ and Ψ are incoherent.

The coherence between two basis, $\mu(\Phi, \Psi)$, quantifies the highest correlation between any two elements of Φ and Ψ. The case of maximum coherence occurs when the two basis share a vector. In this case $\mu(\Phi, \Psi) = \sqrt{N}$. Coherence cannot be zero because both basis represent the same vector space. The range of possible values is $\mu(\Phi, \Psi) \in [1, \sqrt{N}]$. When coherence is minimum, it said that the basis Ψ and Φ are incoherent.

Then, if an object is k-sparse in Ψ (has $k < N$ non-zero coefficients), if the $measurement\ matrix$ is random, and if is true that

$$M \geq kC\mu(\Phi, \Psi)\log(N), \tag{2.6}$$

where C is a positive constant, then the image estimated from

$$O_{\Psi_e} = \arg\min_{O_\Psi} \|O_\Psi\|_1 \quad \text{such that } \Theta \cdot O_{\Psi_e} = Y, \tag{2.7}$$

satisfies that $O_{\Psi_e} = O_\Psi$ with a high probability [142].

The objective function used in the optimization problem for the estimation of the image is the l_1-norm $\|O_\Psi\|_1 = \sum_{i=1}^{N} |o_i|$. According to equation (2.6), we can say that the more incoherent the measurement basis Φ and Ψ are, less measures must be made to recover the image. The classical approach to solve such optimization problems is by least squares adjustment, minimizing the l_2-norm, $\|O_\Psi\|_{1_2} = \sum_{i=1} |o_i|^2$. However, when the image is sparse the minimization of this norm is almost never achieved [143].

Another design option for the $measurement\ matrix$ is performing a random subsampling of the image in its sparse representation O_Ψ [141]. Then, the $measurement\ matrix\ \mathcal{S}$ consists of rows which are vectors of the basis Ψ randomly chosen. This design choice, which is similar to the one used in Magnetic Resonance Image (MRI) [144], has been chosen in this thesis when CS has been applied.

The quality of the compressed images was tested in a simulation using a 2D object with $N = 4096$ by using the standard peak signal-to-noise ratio, $PSNR = 10\log(I_{max}^2/MSE)$, where I_{max} is the maximum pixel intensity value of the reference image and $MSE = \frac{1}{N}\left\|I_{ref}^{in} - I_{rec}^{in}\right\|^2$, where I_{rec}^{in} is the undersampled image and I_{ref}^{in} is the image recovered without compression. The result of this analysis for the case of the reflection mode is shown in Figure 2.6. The figure shows a plot of the PSNR together with the reconstructed image for different compression ratios. It can be seen that when only 50% of the total number of patterns are used for the reconstruction, that is, CR=2, the value of the PSNR indicates a high image

fidelity while the acquisition time required for the sensing stage would be reduced by a factor of 2.

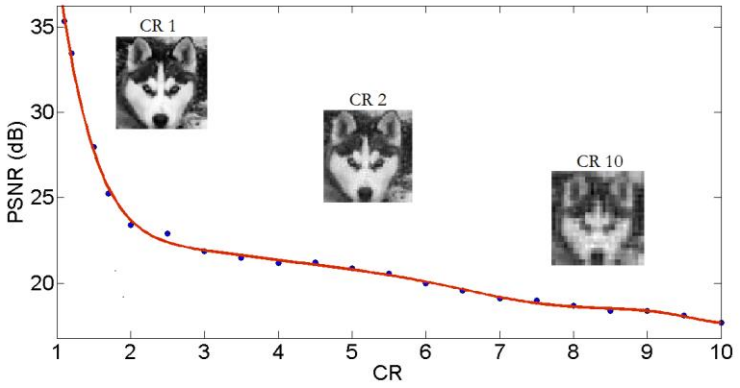

Figure 2.6. Example of the PSNR of a single-pixel image as a function of the compression ratio (CR=N/M).

Until now, it has been considered that the acquired measurements are noise-free and, therefore, the restriction on the optimization problem in expression (2.8) is just $Y = \Theta \cdot O_{\Psi_e}$. In other words, we require that the final estimation be compatible with the measurements. A more realistic model takes into account the errors in the measurements and considers that $Y = \Theta \cdot O_{\Psi_e} + n$, where n is an unknown disturbance limited by a known amount $\|n\|_2 \leq \epsilon$. This allows to establish the optimization problem as

$$O_{\Psi_e} = \arg\min_{O_\Psi} \|O_\Psi\|_1 \quad \text{such that } \left\|\Theta \cdot O_{\Psi_e} - Y\right\|_2 \leq \epsilon. \tag{2.8}$$

In this chapter we have seen how single-pixel imaging consists in measuring the projections of an object onto each vector of a basis, in our case, the Walsh-Hadamard basis. These projections are carried out experimentally by an SLM, while the measurements Y are carried out by a detector with no spatial resolution. We have described also different types of SLM which are commonly used today, emphasizing their frame-rate, a key feature for single-pixel imaging systems. Then, we have described the most common bucket detectors used in single-pixel imaging configurations,

comparing point-by-point characteristics such as spectral and temporal response, signal-to-noise ratio, gain and dynamic range. Finally, we have introduced the concept of compressive sensing, a mathematical tool that allows us to reduce the number of projections necessary to reconstruct an image of the object with fidelity, thus trying to improve the bottle-neck that supposes the limited speed of SLMs.

Chapter 3. Single-pixel Microscopy

In this chapter we develop a microscope able to capture images of a sample at the same time with a conventional camera and with a single-pixel camera. We give proof of principle of the robustness of the collection stage on single-pixel cameras compared with conventional imaging by studying the transversal and axial resolution of both systems. The transversal resolution of the single-pixel system is shown to be not limited at all by the optical quality of the collection optics. This result is proved by using a low NA microscope. Spatial frequencies that are not transmitted through this low quality optics in conventional imaging are demonstrated to be present in the retrieved image through patterned illumination. This is possible because the information required by the single-pixel detector is just the total intensity transmitted by the objective and the deviation from the mean for different sampling patterns. This is closely related to speckle illumination and second-order correlation, whose measurements have shown to provide sub-Rayleigh limit imaging [145,146]. We also demonstrate experimentally the capability of our technique to properly recover an image even when an optical diffuser is located between the sample and the single-pixel detector. This property can be relevant in microscopy for biomedical applications as scattering is the main parameter limiting penetration depth in tissue samples. To study these properties we have built an open-air microscope based on liquid crystal on silicon SLM. The optical setup is capable of projecting amplitude binary patterns onto a sample and collecting the transmitted light simultaneously by a conventional imaging system and a single-pixel detector.

3.1 OPTICAL SETUP

The key part of our optical system is a spatial light modulator system based on a reflective LCOS micro-display (Holoeye LC-R 2500). This device is the optical element responsible for sequentially coding the Walsh-Hadamard patterns. The amplitude binary patterns encoded on the SLM screen, just like in any commercial microscope, are demagnifed and projected onto the sample plane by a tube lens and an objective lens. The light transmitted by the sample is then collected by a second objective. Then, the light is divided into two optical paths. In one of these paths, a tube lens generates an image on the sensor of a conventional camera. In the other path, the light is integrated onto a single-pixel detector.

The experimental setup is shown in Figure 3.1. The setup can be divided into two parts: illumination system and collection system, both of them separated by the object sample (OB), which in our case consists of an USAF resolution test chart (USAF 1951, $2" \times 2"$, Edmund Optics). This resolution chart consists on groups of three elements (Ronchi rulings) with different sizes. The largest bar the optical image cannot discern correspond to the limit of its resolving power.

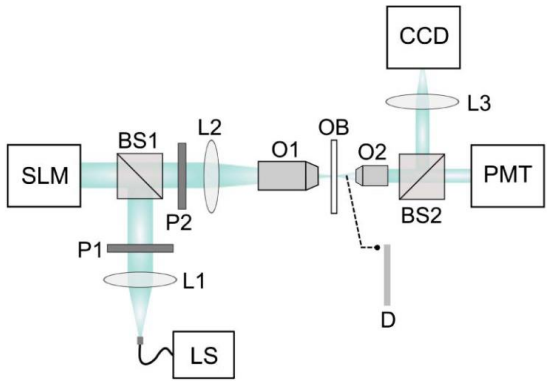

Figure 3.1. Experimental setup for image resolution analysis via Walsh-Hadamard illumination with simultaneous conventional camera and SPI detection. (LS) Light source. (SLM) Spatial light modulator. (P1 and P2) Linear polarizers. (BS1 and BS2) Beam-splitters. (O1) Projection objective. (OB) Sample object. (L1-L3) Lenses. (D) Diffuser. (O2) Collection objective. (CCD) Camera. (PMT) Photomultiplier tube.

The light source used for this experiment consists of a white light source (LS, Nikon, Intensilight C-HGFI) filtered with a green passband filter (part of Pasco AP-9368). As already mentioned in section 2.2.1, in order to use this reflection phase-modulator as a binary amplitude modulator, it must be sandwiched between two linear polarizers. Taking this into account, the light source is first collimated by L1 and linearly polarized by P1. The polarized light beam travels through a beam-splitter (BS1), which allows the SLM to work at normal incidence. The light reflected by the SLM goes through BS1 again and then through the second polarizer (P2). Lens L2 (tube lens) and objective O1 (Nikon LU Plan 20X/0.40 WD 13) constitute the microscopy system and create an image of the amplitude pattern coded onto the SLM over the sample object OB.

The collection system consists of an objective (O2, Nikon E Plan 4X/0.1 WD 30) that collects the light transmitted by OB. A second beam splitter (BS2) allows to form, altogether with L3, an image of the sample on to a CCD sensor (Basler A102fc) and, at the same time, collects the transmitted intensity into a PMT (PMM01, Thorlabs Inc.).

The pattern projection system has been design in such a way that its resolution limit is given by the projection optics and is not restricted geometrically by the size of the pixels of the SLM. This limit can be calculated using the Rayleigh criterion as

$$\delta p \ = 0.61 \cdot \frac{\lambda}{NA_p} = 0.61 \cdot \frac{525^{-9} nm}{0.4} = 0.8 \mu m, \qquad (2.1)$$

where λ is the central wavelength given by the green passband filter and NA_p is the numerical aperture of the projection objective O1. By using equation (2.1) again, the resolution limit given by the collection optics, with a numerical aperture $NA_c = 0.1$, is $\delta c = 3.2\ \mu m$. The pixel size of the SLM is $19\ \mu m$. Due to the magnification of L1 and O1, the pixel size at the sample plane is $1.68\ \mu m$. Thus, the size of the projected pixels is bigger than δp but smaller than the resolution limit given by the collection optics δc. In other words, the whole system is designed in such a way that the

higher frequencies of the Walsh-Hadamard patterns are able to go through the projection objective O1 but not through the collection objective O2.

3.2 STUDY OF THE TRANSVERSAL RESOLUTION

The part of the resolution test used for the study of the transversal resolution is shown in Figure 3.2(a). These elements correspond to resolutions ranging from 7.81 μm (group 6, element 1) to 2.19 μm (group 7, element 6).

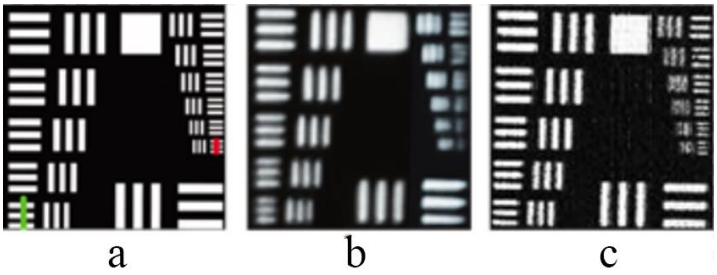

Figure 3.2. Experimental results for image resolution analysis. (a) Part of the USAF test resolution chart. (b) Image obtained with CCD camera. (c) Reconstructed image of 128 × 128 pixels via single-pixel imaging (CR = 2).

To obtain an image with the conventional camera system, we illuminate the whole sample with a uniform light beam. To this end, we encode an all-white pattern on the SLM screen. On the other hand, the image reconstructed by the SPI system has been obtained by using compressive sensing with only 50% (CR=2) of the total Walsh-Hadamard patterns obtained from Hadamard matrix $\mathcal{H}_{16384}$. In principle, the theoretical resolution of the conventional system is limited by diffraction to 3.2 μm, given by the lowest aperture of the system, determined by objective O2. As a matter of fact, Figure 3.2(b) shows that the image taken by the CCD resolves up to element 6-5 of the USAF test chart, corresponding to a resolution of 4.9 μm. As shown in Figure 3.1, the collection objective O2 is common for both conventional and single-pixel systems. However, as the single-pixel system is based on measuring integrated intensities, instead of resolving the spatial information, the

collecting system has no influence on the resolution. It can be seen that the resolution achieved by the single-pixel system in Figure 3.2(c) reaches element 7-6, which corresponds to a resolution of 2.19 μm. In this sense, this system resembles to some extent to Type I scanning optical microscopes but with wide-field illumination [1]. As a matter of fact, if the objective O2 is removed and the PMT is located directly behind the sample, the resolution of the final image would be the same.

It can be observed in Figure 3.2(b) and Figure 3.2(c) corresponding to CCD and single-pixel imaging, respectively, an asymmetry between horizontal and vertical lines. This might be due to cylindrical aberration induced by the SLM.

The improvement of resolution is clearly noticeable in Figure 3.3. For both group 6-6 (left) and group 7-6 (right) the intensity profiles for the single-pixel camera allow us to discriminate the lines of both elements while this is not possible for the conventional imaging system. These results show that the image obtained by single-pixel imaging contains frequencies of the object that are above the frequency limit associated with the low-quality objective lens when it is used in conventional imaging.

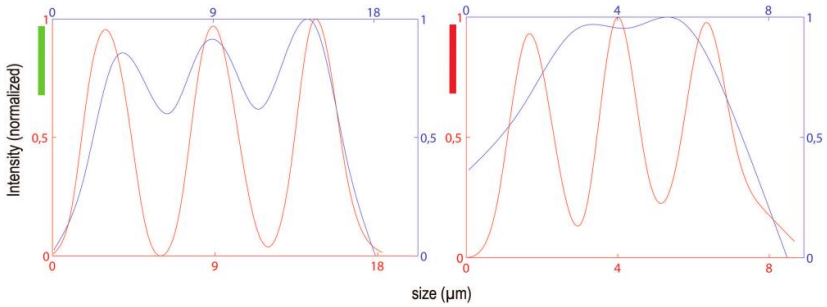

Figure 3.3. Panels (left) and (right) show intensity profiles for USAF elements 6-6 and 7-6, respectively (green and red lines in Figure 3.2). Blue lines correspond to the CCD camera and red lines to the single-pixel image. The curves have been interpolated.

In other words, our single-pixel imaging system is able to provide images with a resolution below the Rayleigh criterion of the collection optics, being limited just by diffraction in the projection system. This is due to the spread of the spatial spectrum of the object produced by the projection of the high-

frequency Walsh-Hadamard patterns. In other words, while in a traditional illumination microscopy system high-frequencies of the object are lost because they exceed the maximum angle of the collection system, defined by the NA, in single-pixel imaging techniques, the information of all frequencies are present at lower angles, been able to travel though the low NA optics. This effect is similar to that produced by structured illumination in super-resolution approaches based on spatial-frequency multiplexing [147].

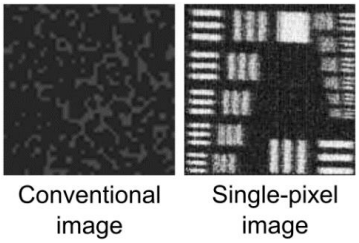

Figure 3.4. Images taken through a commercial diffuser placed between OB and O2 (see Figure 3.1). (a) Image obtained with CCD camera. (b) Reconstructed image via single-pixel imaging (CR = 2).

To emphasize the fact that the resolution of the single-pixel system only depends on the projection system and that it is tolerant to some optical aberrations in the collection stage, next we prove that the system is able to recover images even when a diffuser distorts the light diffracted by the object. Figure 3.4(a) shows the image of the USAF resolution test chart provided by the conventional imaging system when a commercial diffuser (D, Edmund Optics T54-497, see Figure 3.1) is placed between the sample and the collection system. Note that the image is completely blurred by the action of the diffuser. Interestingly, the SPI approach based on single-pixel detection is able to reconstruct the image as can be seen in Figure 3.4(b). In fact, the presence of the diffuser in the optical system in Figure 3.1, could be advantageous due to an improvement in the average ratio between the low and high frequencies that reach the detector. This improvement result from the angular and spatial spread of light by multiple scatterings in the diffuse media [148]. The combined action of the high-frequency patterns projected onto the object and the frequency mixture provided by the diffuser

allow us to record frequencies of the object not resolved by conventional imaging systems.

The total time required to take the image data increases with the number of measurements. Using CS, the exact number M depends on the features of the object under consideration. As in this work a low frame-rate LCOS has been used, to reduce the number of projected patterns and, therefore, the time necessary to project these patterns, is a very interesting objective. For this reason, as explained in section 2.4, in this experiment we tested the quality of the recovered images evaluating the standard peak signal-to-noise ratio (PSNR). The results are shown in Figure 3.5. As in the simulation shown in Figure 2.6, it can be seen that when $CR = 2$, the PSNR is still higher than 20 dB, which indicates a high image fidelity while the acquisition time required for the sensing stage is reduced by a factor of 2. It exists then a trade-off between image quality and acquisition time. Thus, for example, if the object does not contain high frequencies, perhaps a higher compression ratio can be used. This could allow to recover this object without losing important information while increasing the speed of the experiment. On the other hand, if the object is composed mostly by high frequencies, it is possible that the compression factor has to be reduced and, therefore, the projection requires more time.

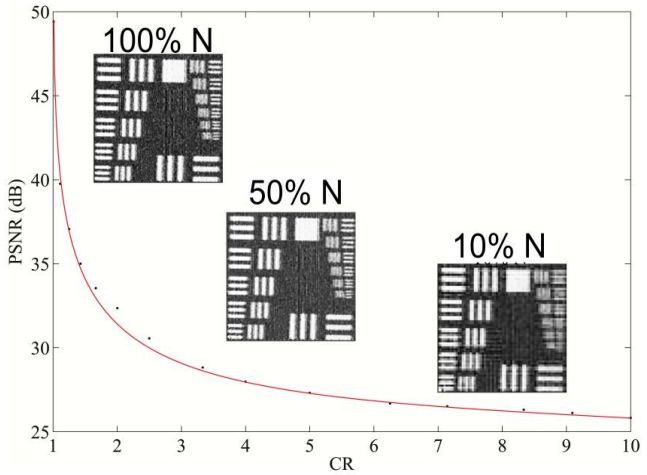

Figure 3.5. Experimental example of the PSNR of a single-pixel image as a function of the compression ratio (CR=N/M).

3.3 STUDY OF THE AXIAL RESOLUTION

In addition to the transversal resolution study, we have performed a study of the axial resolution. We analyze numerically the result of defocusing the projection system of a single-pixel camera with respect to the position of the object sample. We also compare the result with that obtained by defocusing the imaging system of a conventional camera.

The simulated single-pixel imaging system can be divided into projection system and detection system as shown in Figure 3.6. The projection system consists of two lenses that projects patterns onto an object. These patterns may or may not be out of focus (Δz). The projection optics is defined by the pixel size of the pattern, the NA and magnification of the optics and by the wavelength of the illumination. The magnification of the projection optics allow us to calculate the effective pixel size of the projected pattern on the object plane while the NA of the projection system works as a low pass filter on the patterns.

The detection system consists of a lens and a single-pixel detector. In the collection system we define a NA that allows us to calculate the maximum spatial frequency of this collection system, as has been shown in the previous section.

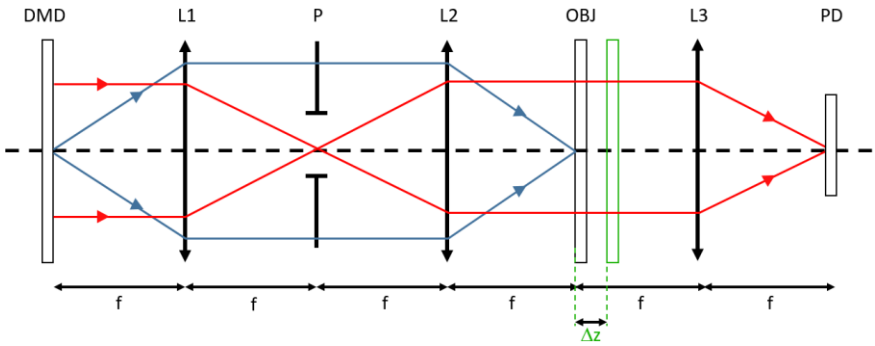

Figure 3.6. Ray tracing for a single-pixel imaging system. The sample object (OBJ) is illuminated with a plane wave while the 4f system (lens L1 and L2) projects the patterns codified on the DMD screen onto the object plane. The photodiode (PD) integrates all the intensity transmitted on each projection. (P) Pupil of the 4f system.

The projection optics is composed by a 4f system that forms an image of the DMD on the plane of the object while illuminating the sample with a plane wave. If we introduce a displacement of the object Δz with respect to the image plane of the pattern projection system, the intensities measured by the PD are

$$I_i^D = \sum_{x,y} \{[WH_i(x,y) \circledast |a(x,y)|^2] \cdot O(x,y)\}, \tag{3.1}$$

where $WH_i(x,y)$ are the projected patterns and $a(x,y)$ is the PSF of the projection system at the object plane.

If we use the intensities I_i^D to recover the image by single-pixel imaging techniques, it can be shown that the result would be

$$\sum_i I_i^D WH_i(x,y) = O(x',y') \circledast |a(x',y')|^2, \tag{3.2}$$

which means that a displacement of the object with respect to the image plane of the pattern projection optics is equivalent to defocusing the object.

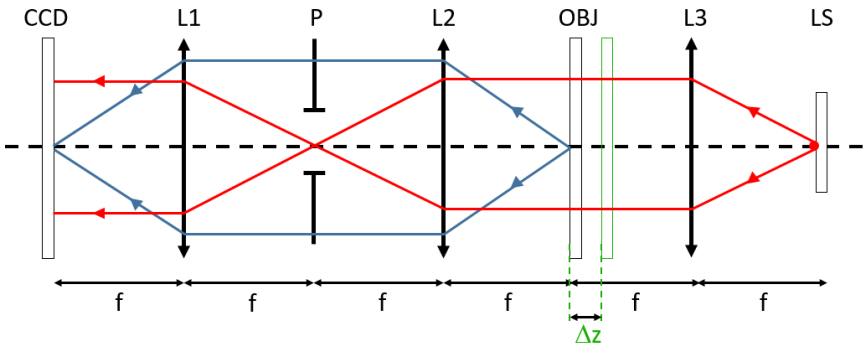

Figure 3.7. Ray tracing for a conventional imaging system. The sample object (OBJ) is illuminated with a plane wave by the light source (LS) while the 4f system (lens L1 and L2) creates an image of the object onto the sensor plane. (P) Pupil of the 4f system.

On the other hand, in Figure 3.7 we show the geometrical ray tracing for a conventional imaging system with a CCD camera. In this system a light source illuminates the object while a 4f system creates an image of this object onto the CCD sensor. The ray direction is considered from right to left on purpose, to emphasize the analogy among the optical system in

Figure 3.6 and Figure 3.7. In this system, if we move the object Δz with respect to the position of the focus of L2, the PSF of the defocused 4f, if coherent illumination is used, would be

$$a(x,y) = \left| \mathfrak{F}\left\{ p(x',y') \cdot e^{j\frac{\pi}{\lambda}\left(\frac{1}{d_0}+\frac{1}{d_i}-\frac{1}{f}\right)\left(x'^2+y'^2\right)} \right\} \right|^2, \qquad (3.3)$$

where $p(x', y')$ is the pupil of the system and $d_i = \Delta z + f$. Then,

$$a(x,y) = \left| \mathfrak{F}\left\{ p(x',y') \cdot e^{j\frac{\pi}{\lambda f}\left(\frac{\Delta z}{f(f+\Delta z}\right)\left(x'^2+y'^2\right)} \right\} \right|^2. \qquad (3.4)$$

It can be shown that this expression of the PSF is the same as in equation (3.2). Therefore, it can be concluded that moving the image plane of the projected patterns Δz in a single-pixel imaging system is equivalent to moving the object itself Δz with respect to the object plane in a conventional imaging system, reconstructing in both cases a defocused object.

The study of the axial resolution has also been performed through computer simulations in MATLAB®. The simulation has been performed following the schemes described in Figure 3.6 and Figure 3.7 for the SPI and conventional camera system, respectively. For the SPI system, first we Fourier filter the patterns, simulating the loss of frequencies caused by the numerical aperture of the projection optics. The filtered image of the DMD screen is propagate a distance Δz to the plane of the object using a conventional fast Fourier transform (FFT) algorithm for Fresnel propagation. Then, this filtered and propagated pattern is multiplied by the object. This projection is then propagated a distance Δz_1 and a Fourier transform is made to simulate the collection optics. The intensity associated to the sampling pattern is obtained by summing the square modulus of the values computed in the pixels of the central region of the Fourier transform. This process is repeated for each pattern of the basis and, from them, we reconstruct the image using the SPI algorithm.

A similar simulation is performed for the conventional imaging system. In this case, the object is propagated a distance Δz and then imaged by the same 4f optical system as in the previous simulation.

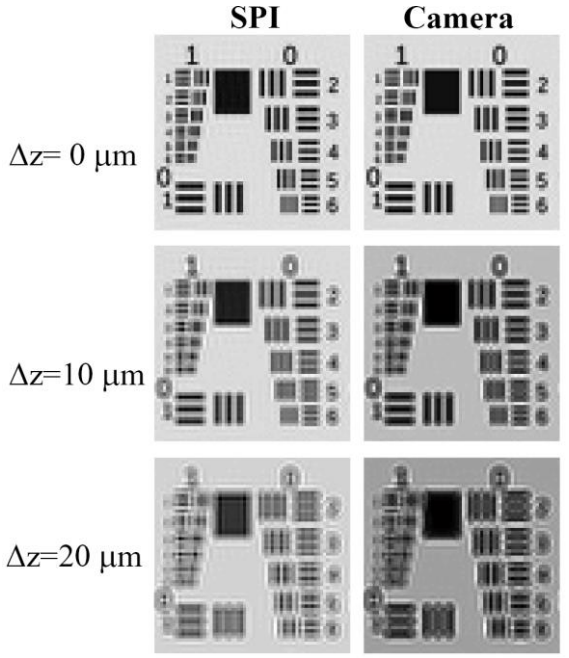

Figure 3.8. Simulation of the images obtained by SPI (left) and conventional camera (right) as a function of defocus. Defocus has been achieved by moving the patterns away from the sample plane (SPI case) and by moving the imaging optics (camera case) the same amount.

The results of these simulations are shown in Figure 3.8. It can be seen that the loss of resolution caused by the defocus is equivalent in both cases. It can then be concluded that, if the NA of the projection optics of the patterns is the same as the NA of the imaging optics for the conventional camera ($NA = 0.25$ in this simulation), the displacement of the object produce the same defocus in SPI and conventional imaging.

In summary, in this chapter we have built an open-air microscope capable of taking images with a camera and with a single-pixel detector at the same time. This comparison has shown that our single-pixel system is able to provide images with a transversal resolution below the diffraction limit of the detection system, proving that spatial frequencies that are not

present in the conventional optical system are present in the retrieved image through patterned illumination. This is due to the spread of the spatial spectrum of the object produced by the projection of the high-frequency Walsh-Hadamard patterns. Therefore, SPI systems are able to reconstruct the object with the maximum resolution provided by the projection. Among high-frequency patterns, the differences of intensity with respect to the average value of the projections may be very small. Hence, as the single-pixel system is based on measuring integrated intensities, instead of resolving the spatial information, it is necessary to use detectors with a high dynamic range, capable of measuring at very different levels of intensity, but also capable of detecting small intensity fluctuations.

On the other hand, the study of the axial resolution shows that a shift of the image plane of the pattern projection system in a SPI system is equivalent to the defocus produced by the shift of the focus plane of the imaging system of a conventional imaging system (camera). Furthermore, as expected, we have also verified that the image obtained by SPI is the same regardless of the position of the collection optics.

Finally, there is a very interesting point related to axial resolution not covered in this work that is worth mentioning. In our single-pixel imaging systems we have considered the measurements Y as the projection of the elements of a basis onto an object so that $Y = S \cdot O$, were each row of S is an element of an orthogonal basis and O is the object. However, just as happens in our simulation, the patterns projected by an optical system are filtered due to the cut-off frequency of the projection optics, given by its NA. Thus, one could argue that instead of calculating O as $Y \cdot S^{-1} = O$, a new matrix, let's say S', calculated from the propagation of S through the optical system, should be use. However, this propagation could cause S' to be not orthogonal and therefore, not invertible. This would cause the final result of O to be found by mathematical approximations. However, these ideas make us think that the study of these propagation properties of Walsh-Hadamard patterns could be of great interest for the improvement of axial resolution and optical sectioning in single-pixel imaging systems.

Chapter 4. Dual-mode optical microscope

Conventional optical microscope designs make simultaneous imaging of a sample in transmitted and reflected modes inefficient, restrictive or even impossible. In general they need different light sources for transmission and reflection, thereby preventing that both images be simultaneously measured in a single sensor. Alternatively they can work with several digital cameras, but then a careful calibration and geometric adjustment of both sensors is necessary. However, in this chapter we demonstrate that the SPI architecture is particularly well-fitted for this dual operation recording both reflection and transmission information simultaneously with a single light source and a simple light sensor configuration constituted by two single-pixel detectors. This is done with no need of calibration procedures since the field of view, resolution, and focusing plane are controlled exclusively by the properties of the light patterns generated by the optical projection system. The usefulness of dual-mode microscopy for histopathology studies of skin tissue has been recently reported based on a lensless holographic setup [149,150] and near-field scanning optical microscopy [151].

The proposed optical system consist of a dual-mode single-pixel microscope capable of obtaining images of biological specimens in transmission and reflection simultaneously from the same plane of the sample, revealing structures not visible easily by conventional microscopy techniques. To increase the versatility of the system, for this experiment we have used an inverted commercial microscope to which we have attached a commercial grade DMD. This allows us to use different ports of the commercial microscope to locate photodetectors in transmission and reflection.

By recording transmitted and reflected information simultaneously, loss of data by self-shadowing is minimized which can be advantageous in non-uniform samples containing transparent and opaque regions. Additionally, the simplicity of the detection system would allow us to record different spectral channels or polarization states in each imaging mode very easily, increasing the versatility of the dual-microscope system.

4.1 SINGLE-PIXEL IMAGING DUAL-MODE MICROSCOPY

In a dual-mode SPI microscope, the forward and backscattered light components are simultaneously collected onto two single-pixel photodetectors located at the transmission and reflection ports of the microscope, respectively. In the same way as discussed in section 2.4, a sequence of N sampling patterns is codified onto the DMD so that the irradiance striking the photodetector at the transmission is

$$Y = \mathcal{S} \cdot \mathrm{O_T}, \tag{4.1}$$

where $\mathcal{S}$ is the $measurement\ matrix$ whose ith row is a one-dimensional reshaping of the ith sampling mask $\mathcal{H}_i$, and $\mathrm{O_T}$ and Y are N-dimensional vectors representing a one-dimensional reshaping of the unknown object transmittance distribution and the result of the measurements at the transmission photodetector, respectively.

Equivalently, the measurements at the reflection port are concisely represented by the series of linear equations

$$Z = \mathcal{S} \cdot O_R, \tag{4.3}$$

where O_R and Z are N-dimensional vectors representing a one-dimensional reshaping of the unknown reflectance distribution and the result of the measurements at the reflection photodetector, respectively.

As in section 2.1, in the easiest implementation of the retrieval algorithm, which is possible for well-conditioned measurements systems, a number of measurements M equal to the number of pixels of the sample is

required and both the transmission and the reflection images are retrieved through the inverse matrix as

$$O_T = \mathcal{S}^{-1}Y, \qquad O_R = \mathcal{S}^{-1}Z. \tag{4.4}$$

In the same way as in section 2.4, compressive sensing allows us to take samples of the *N*-dimensional transmission vector T using an $M \times N$ matrix $\mathcal{S}'$, where $M < N$, obtaining under sampled measurements $Y' = \mathcal{S}'O_T$. And the same operation can be performed for the case of reflection. Then, the object for both modes is recovered using compressive sensing algorithms.

4.2 PATTERN CODIFICATION ON DIAMOND SHAPED DMDS

As already mentioned in section 2.2.2, DMDs can be divided in two categories, commercial grade and scientific grade. Commercial grade DMDs are regular video projectors, created for consumer electronic, while scientific grade DMDs are devices created to achieve professional performance and used for scientific and engineering applications. Scientific grade DMDs have higher resolution and higher refresh rates, up to 22.7 kHz, but they are complex to control and more expensive. On the other hand, commercial grade DMDs work only at video rates (60-120 Hz for RGB images). Our intention in this approach is to use commercial devices for both the SLM and the microscope. Commercial grade DMDs use a diamond structure for the periodic configuration of micromirrors, instead of an orthogonal configuration, as is shown in Figure 4.1. The diamond pixel layout is commonly used in these devices to reduce the size of the optical system. This is because each micromirror tilts along its diagonal axis when operated to modulate the incident beam. Therefore, this configuration of the micromirrors allows to contain the incident beam, the reflected beam, and the horizontal axis of the DMD in the same plane. However, the direct implementation of an $N \times N$ image onto the diamond pixel layout differs from the implementation onto the conventional orthogonal pixel layout (used in scientific grade DMDs). In an orthogonal layout the rows and the

columns are straight lines, so the aspect ratio is preserved. However in the diamond layout, if an image is sent directly to the device, meanwhile the rows are interpreted as straight lines, the columns become zigzag lines. Thereby the direct implementation changes the original aspect ratio of the image. Moreover, straight edges are transformed on zigzag edges. Both consequences are shown in Figure 4.1.

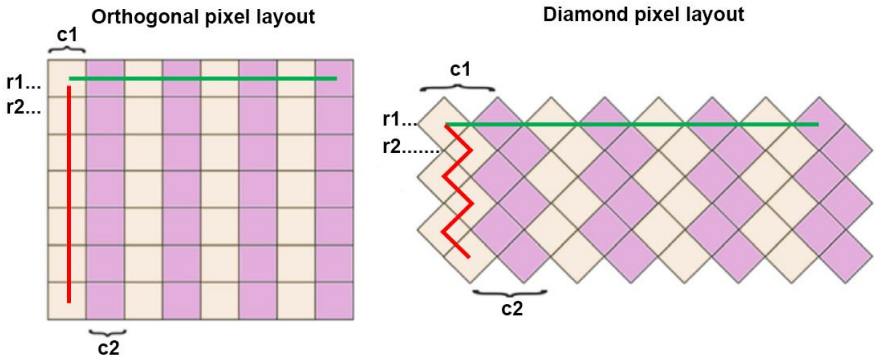

Figure 4.1. Graphical representation of the different coordinate systems for orthogonal pixel layout (left) and diamond pixel layout (right). (c1 and c2) Column 1 and column.2. (r1 and r2) Row 1 and row 2. Red and green lines represent a complete column and row respectively.

When these devices are used for video projection operation, these effects are not appreciable. However, when used to project light patterns in single-pixel imaging applications, artifacts are produced, because the real projected patterns differ from those used in the reconstruction process. To see this effects due to the miscoding of the patterns in image retrieval within the framework of SPI, we reconstructed the transmission mode of a negative USAF test chart (USAF 1951 $2" \times 2"$) using the experimental setup described later in section 4.3. The number of projected patterns (Walsh-Hadamard patterns) was 4096, with a resolution of 64×64 pixels, using no compression techniques. The result is shown in Figure 4.2.

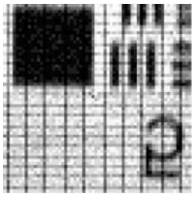

Figure 4.2. Experimental image reconstructed without pattern pre-distortion (64×64 pixels) for the transmission mode. Geometrical artifacts (phantom grid) due to the diamond layout are clearly noticeable.

To avoid these artifacts, before sending an image to the DMD, the information must be codified in a different way. The aspect ratio could be preserved pre-distorting the original image but this operation do not correct the zigzag edges artifact. A subtler coding is presented that preserves both the aspect ratio and edges of the original image. An example of the operation of our coding algorithm is presented in Figure 4.3 (a) and (b) for the case of a 2×2 image. Without correction, information codified in a 2×2 array provides a distorted image in the diamond layout as is shown in Figure 4.3(a). Our algorithm codifies the information in the array in such a way that the original image appears rotated but preserves the aspect ratio and straight edges, as shown in Figure 4.3(b). Figure 4.3(c) shows how the algorithm works to transform the array. In general, the algorithm transforms an $N \times N$ image (where N is even) into a $(2N-1) \times N$ array, following the next steps:

1. Diagonals are extracted from the initial image in the order shown in Figure 4.3(c).
2. Each row of the $(2N-1) \times N$ image is built by zero-padding each diagonal. The order of the rows matches the order of the extracted diagonals. If the row is even, it is padded to left and right of the diagonal with the same number of zeros. If the row is odd, an additional zero is needed to the left.

In this way, by means of this previous transformation, the coding of a square image is displayed as a square image rotated 45 degrees, preserving the original aspect ratio and edges.

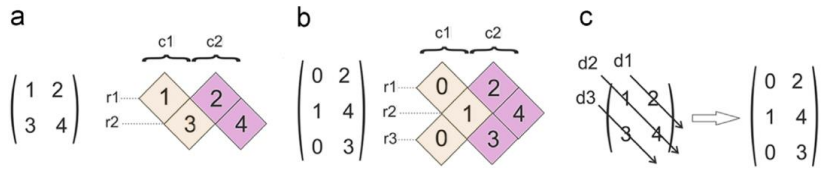

Figure 4.3. Graphical representation of the matrix transformation applied to the projected patterns to avoid artifacts.

On the other hand, in order to improve speed performance of commercial grade DMDs, commonly limited to operate with frequencies between 60 and 120 Hz, we can take advantage of the codification procedure used by the DLP for color video projection. In the standard video projection mode, the light source changes sequentially to red, green and blue colors. For each color, the display codifies 8 binary patterns. With this in mind, an improvement in speed can be done by codifying 24 binary patterns within a single 24-bit color depth image (see Figure 4.4) while illuminating the DMD screen with a single light source. This technique allows an improvement in the speed rate by a factor equal to 24, going from 60 -120 Hz to 1440 - 2880 Hz.

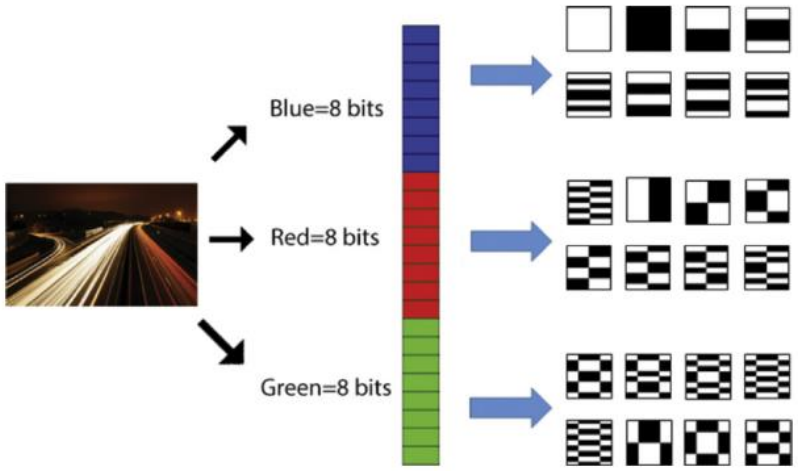

Figure 4.4. Codification of a 24-bit image with 24 Walsh-Hadamard patterns with 1-bit depth. This technique allows an improvement in speed rate of 24, going from 60–120 Hz to 1440–2880 Hz.

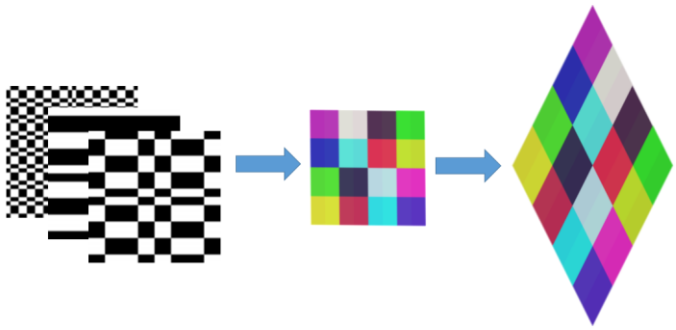

Figure 4.5. Summary of the coding and reshaping process of the Walsh-Hadamard patterns.

4.2.1 Synchronization signal

In addition to high temporal consistency, scientific grade DMDs feature TTL synchronous outputs. This allows, for example, synchronization with cameras or, in the case of SPI, to identify easily each intensity measurement with the projected pattern. Unlike scientific grade DMDs, in commercial grade DMDs the time lapse between 24-bit images is not accurate. This is because the video projector repeats each image several times (for visual purposes) before switching to the next 24-bit image. Besides, they are usually not equipped with TTL synchronization output signals. In most cases it will be possible to find a part of the hardware in the video projector that emits an electrical signal each time the video projector updates. However, because this repetition of the images is not reliable, here we propose a software solution consisting of encoding synchronization patterns embedded in the 24-bit images.

In Figure 4.6 we plot the temporal response of the transmission photomultiplier tube for a single 24-bit image. In this case, the first and last pattern encoded in the 24-bit image are a black pattern (green lines). Experimentally, 24-bit images encoded with black patterns in the first and last bit are alternated with 24-bit images with white patterns in the first and last bit. These synchronization patterns allow us to subsequently establish the measured signal for each pattern. The sampling patterns and the object

used to obtain the plot in Figure 4.6 were the same as those in the experiment seen in Figure 4.2.

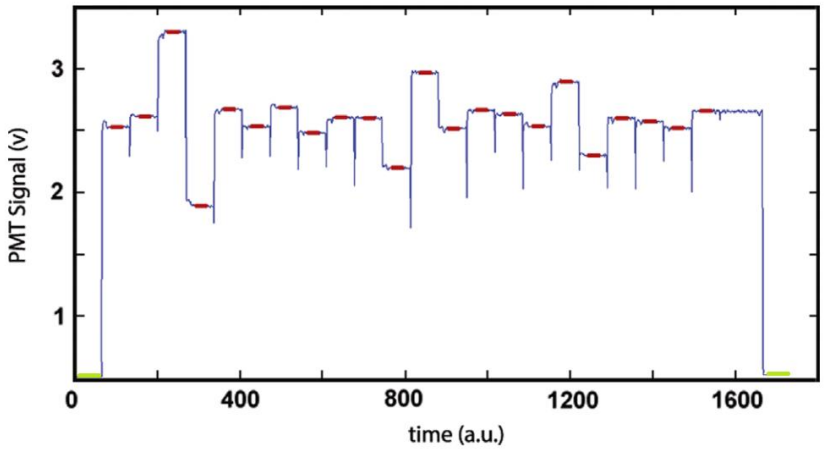

Figure 4.6. Photocurrent values for a single 24-bit depth image. In the graphic the different values for each 1-bit depth pattern codified in the 24-bit image are shown in red color. In this case, the first and last bits are use as reference values (green lines).

4.3 EXPERIMENTAL SETUP

In this section we describe how to adapt a commercial DMD for pattern illumination projection to a commercial inverted microscope. The DMD chosen was a commercial video projector based on DLP technology (DLP LightCrafter™ EVM 0.3 WVGA). The illumination system is composed by the same light source used in the previous experiment (LS, Nikon, Intensilight C-HGFI). In order to be able to illuminate the DMD screen directly with our light source, we first removed the optics and the illumination system of the video projector. The optical configuration of the pattern illumination system for an infinity-corrected microscope is shown in Figure 4.7 (A).

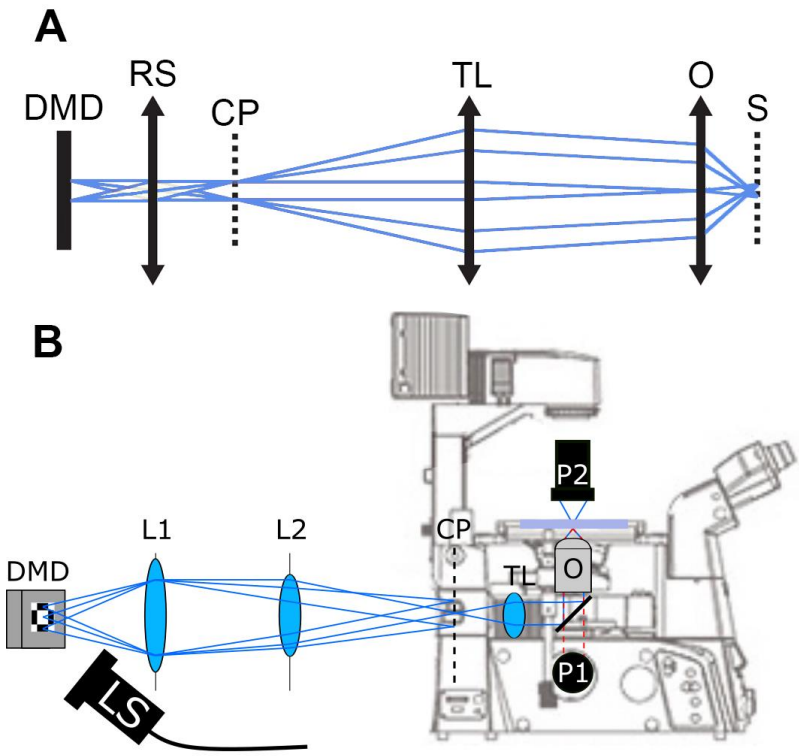

Figure 4.7. (A) Optical configuration for the illumination system for an infinity-corrected microscope. (B) Final optical configuration for the SPM. (LS) Light source. (L1) Lens 1. (L2) Lens 2. (RS) Relay system. (CP) Conjugated plane of the DMD and the sample. (TL) Tube lens. (O) Objective. (S) Sample. (P1) Reflection PMT. (P2) Transmission PMT.

First, we create an intermediate image of the DMD in the conjugated plane (CP) of the back port of a commercial microscope (Nikon Eclipse Ti-U, Figure 4.7 (B)) using a relay system (RS) formed by lenses L1 ($f = 100$ mm) and L2 ($f = 200$ mm), both achromatic doublets. The magnification of this relay system is determined by the ratio of the focal lenses ($M = f_{L2}/f_{L1}$) which will yield $M = 2$. In an infinity-corrected microscope, the objective lens (O) is combined with a tube lens (TL) to form a two lens system. Thus, to transfer the intermediate image of the DMD to the sample plane, an accessory tube lens (TL) has been used. The distance between the CP and the TL should be equal to the focal length of the TL, which for Nikon tube lenses is 200 mm. Furthermore, this TL is optically designed to

work with the objective lens used, O (Nikon LU Plan 20X). The two collection systems for reflection and transmission are composed by a condenser lens and a PMT (PMM01, Thorlabs Inc.). The reflection PMT is placed in a lateral port and the transmission PMT is placed above the stage of the microscope.

4.4 RESULTS

With the aim of analyzing the optical resolution in both transmission and reflection modes, a negative USAF test chart (USAF 1951 $2" \times 2"$) is employed as an object in the setup shown in Figure 4.7. The microscope objective is a 20X with 0.40 NA. Again, only the smallest groups of the USAF test, 6 and 7, were used to determine the resolution of the system. The results are shown in. Figure 4.8

In our experimental setup, the PMT can detect light signals at frequencies as high as 20 kHz. However, the maximum acquisition frequency is limited by the frame rate of the commercial grade DMD to 120 Hz for RGB images and, therefore, to 2880 Hz for binary images. To reduce the acquisition time even more, compressive sensing algorithms were used. Pictures (a) and (b) in Figure 4.8 show transmission and reflection images, respectively, by using approximately 25% of the total number of patterns (M=1012) for a resolution of 64×64 pixels while (c) and (d) have an approximate compression of 50% (M=2046) for the same resolution. Pictures (e) and (f) were obtained by projecting almost the total number of patterns (M=4092). The results show that the resolution obtained by transmission and reflection are almost identical (2.46 μm for the images with no compression) and that reducing the projected patterns to 50% does not significantly affect resolution (2.76 μm) but allows measuring twice as fast. These two resolution values are obtained from the last resolvable element of group 7 (5 and 4, respectively).

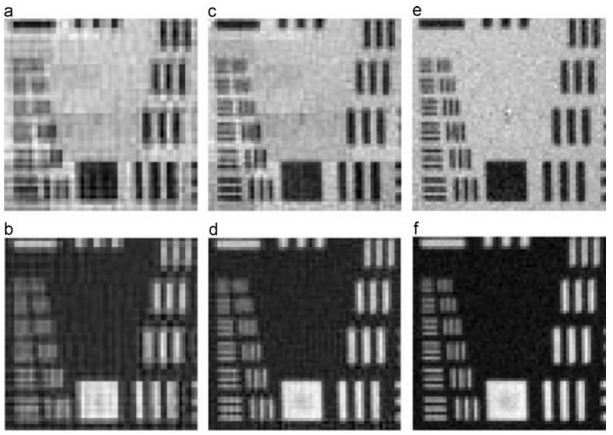

Figure 4.8. Experimental images of the USAF test (groups 6 and 7) obtained with the dual-mode single-pixel microscope in Figure 4.7 using compressive sensing algorithms with a different compression ratio. Pictures (a) and (b) show transmission and reflection images, respectively, by using only 25% of the total number of patterns for this resolution (64x64 pixels). Pictures (c) and (d) show the result by using 50% of the patterns while pictures (e) and (f) correspond to the images obtained by transmission and reflection with no compression. In all cases, the size of the image was 64x64 pixels and the field of view 192 μm x 192 μm.

As in section 3.2, the quality of the compressed images was tested using the standard peak signal-to-noise ratio (PSNR) as a function of the compression ration CR. The result of this analysis for the case of the reflection mode is shown in Figure 4.9. The figure shows a plot of the PSNR together with the reconstructed image for different compression ratios. The experimental results again show a good quality image (above 20 dB) for CR values of 2 and 3. So, in this case, it would be possible to increase the speed of the measurement by a factor 3 and still reconstruct an image with a high fidelity.

As a proof of concept, we have also tested the capability of the dual-mode SPI microscope to image biological samples with different reflective and transmissive imaging profiles. The results can be seen in Figure 4.10. The first row shows images of an *Anaphothrips obscurus* in both reflection (a) and transmission (b) modes taken simultaneously. The images have a resolution of 64×64 pixels (M=4096) and were obtained with a 20X microscope objective. In this case the transmission image shows only the silhouette of the insect because of its low transparency. The second row

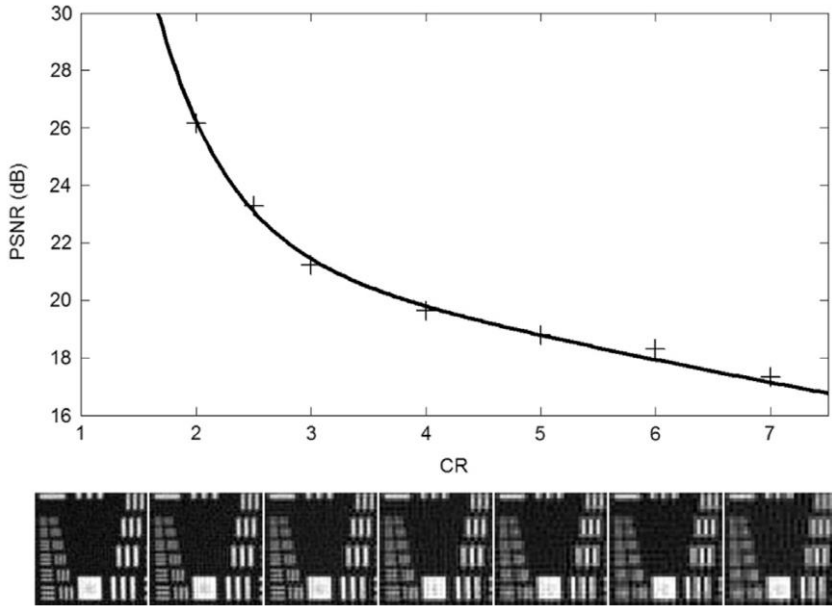

Figure 4.9. (Top) Plot of the standard peak signal-to-noise ratio (PSNR) in dB as a function of the compression ratio $(CR = N/M)$ *to show the quality of the recovered images for the case of the reflection mode. (Bottom) Images reconstructed with the different compression ratios associated with the PSNR plotted in the top figure with increasing CR from left to right.*

shows images of a *Zeuzera pyrina* wing taken with a single-pixel camera in reflection (c) and transmission (d) modes, respectively. Both images have a resolution of 128x128 pixels (M=16,384). In this case, the transmission image shows structures of the other side of the wing (hairs), hidden in the reflection images. The images of both modes are focused to the same plane of the sample and are automatically adjusted geometrically, that is, a pixel of the reflection mode image and the corresponding pixel of the transmission mode image, provide information of the same point of the object. This can be an advantage for biological structural studies. Image (e) shows the same area of the sample taken in reflection with a CMOS sensor located at the output port of the microscope. The resolution of the image is 200x200 pixels.

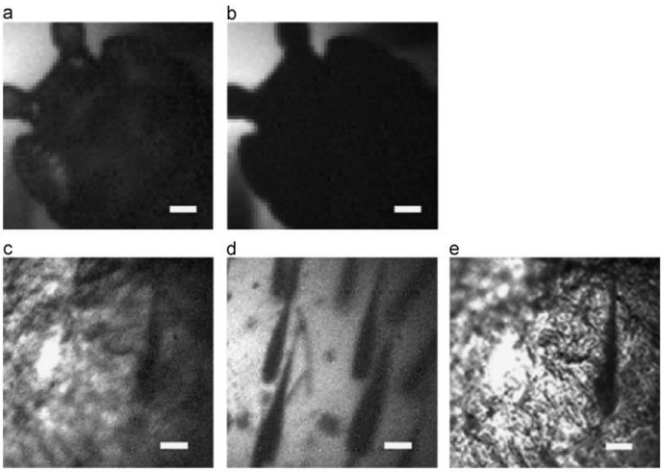

Figure 4.10. Experimental results. Anaphothrips obscurus in reflection (a) and transmission (b) modes obtained with the optical setup in Figure 4.7 using a 20X objective. The images have 64x64 px. Images of a Zeuzera pyrina wing in reflection (c) and transmission (d) modes. In this case the images have a resolution of 128x128 px. (e) Image in reflection taken with a CMOS sensor located at the output port of the microscope. (200x200 px). Scale bar: 25 μm.

In summary, in this chapter we have designed a dual-mode optical microscope based on single-pixel imaging capable of taking images of a sample simultaneously in reflection and transmission modes. This configuration, consisting on a single pattern projection system and two photodetectors, allows us to capture information of the object that, using only one detection mode (reflection or transmission), would be lost due to self-shadowing of the sample. In order to reduce the total cost of the system, a commercial video projector has been used as an SLM to codify the sampling patterns. These devices, designed for multimedia content, do not allow direct implementation of Walsh-Hadamard patterns. Therefore, we have developed a transformation matrix that allows a correct implementation of the patterns on the DMD screen, thus correcting artifacts produced by the diamond pixelated structure used on this type of devices. Moreover, we increase the projection speed by codifying 24 binary patterns within a single 24-bit color depth image, which allows us to send up to 2880 patterns per second. Besides, the use of compressive sensing also allows us to reduce by half the time necessary to recover the object while maintaining a good PSNR and resolution. The experimental results obtained with a

USAF resolution test chart show how the resolution obtained for both modes are identical and correspond exactly to the same part of the test chart. The results obtained with a biological sample show these same properties and provide information of the sample that is impossible to capture in a conventional imaging system working in reflection or transmission.

Chapter 5. Single-pixel Fourier ptychography

In this chapter we develop the counterpart for single-pixel microscopy of Fourier ptychography. We extend the capabilities of raster scanning and SPI by combining bucket detection with a low number of photodetectors with adapted Fourier ptychography algorithms in a SPM working in transmission. By using an iterative algorithm, similar to those used in phase retrieval, it is possible to combine the information from the different photodetectors all together and get a high-resolution image with a large FOV at the same time, extending virtually the numerical aperture of the system.

The principle of ptychography was first discussed in the 1960s, as a solution for phase-retrieval problems. Ptychography is a form of coherent diffractive imaging (CDI) technique. In a ptychographic system, a transmission object is illuminated by a coherent illumination beam (probe). Scattered radiation from this arrangement provides a diffraction pattern at a plane where only intensity is recorded. At least two such diffractive patterns are recorded with the probe shifted in the object plane by a known amount. The idea is to scan the sample while adjacent probe beams overlap significantly. This produces a redundancy of the diffracted data that is used by the ptychographical iterative engine algorithm (PIE) in order to reconstruct an estimation of the phase and amplitude changes generated by the object on the incident wave [152,153].

Experimentally, a ptychography system usually follows the scheme shown in Figure 5.1. A light beam (probe) illuminates a sample, and the diffraction pattern is captured with a CCD. To sequentially obtain the different diffraction patterns, the shift of the illumination function with respect to the sample can be performed by mounting the sample or the diaphragm limiting the light beam on a computer-controlled motorized x/y

stage. But other techniques could also be used to move the probe with respect to the sample, such as, for example, using galvanometric mirrors. This technique was first demonstrated in 1995 using high-energy electron microscopy at subnanometer resolution for a simplified case of a crystalline object [154]. Iterative phase-retrieval ptychography was demonstrated experimentally with visible light [155], hard-X-rays [155] and electrons [156].

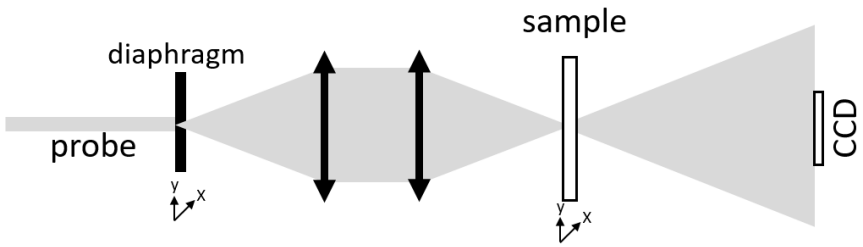

Figure 5.1. Experimental setup for ptychography. A sample is illuminated with a localized field of radiation (probe) and the radiation scattered by the sample is recorded at the Fraunhofer diffraction plane by a CCD. The probe is shifted with respect to the sample to recover two or more diffraction patterns.

Fourier ptychography (FP) is an imaging technique first developed to be used in microscopes [52]. In this technique, the specimen is sequentially illuminated with tilted plane waves with different angles. These tilted plane waves cause a shift in the spectrum of the object in the Fourier domain. Therefore, each image captured by the camera will carry information from different areas of the Fourier spectrum of the object. By using an iterative algorithm, similar to those used in phase retrieval, it is possible to combine the information from these areas of the Fourier domain all together and get a high resolution image with a large FOV at the same time. Using FP algorithms, in addition to producing a large FOV with a high resolution will give us the opportunity of recovering the phase of the object [157] and multi-slice reconstructions [158].

As already mentioned, in both ptychography and FP techniques the image is obtained from the reconstruction provided by the ptychography algorithm. That is, the image is not directly captured by conventional

optical methods. This eliminates the requirement for the customary objective lens. However, when ptychography is applied to a microscope, the use of a conventional microscope objective may be useful for collecting the wave transmitted by the sample. Using this geometry, localized areas of the image can be selected by scanning the light beam across the specimen or by translation of the specimen stage. In the last case the selection of the area of interest of the sample is done by placing a diaphragm in the back focal plane of the tube lens.

From an experimental point of view, Fourier ptychography has certain advantages over regular ptychography. While ptychography has moving parts, either the probe or the sample stage, in FP microscopy (FPM) an array of N LEDs is placed in a relatively far position from the object, which illuminates sequentially the object from different angles, thus avoiding the use of motorized stages. As the distance of the LEDs is assumed far enough from the object, the illumination of each LED can be regarded as a tilted plane wave with a different angle. Then, a low NA microscope objective is used to image the object onto a camera.

The FPM algorithm generates a high-resolution image I_h from a set of N low resolution measurements $I_{lm}(u^i, v^i)$ (with $i = 1,2, \dots, N$), where the spatial coordinates (x, y) of the images have been omitted for clarity and (u^i, v^i) denote the spatial frequency coordinates of each measurement i. The recovery process alternates between spatial and Fourier domains and it assumes that illuminating a thin sample by an oblique plane wave is equivalent to shifting the center of the sample's spectrum in the Fourier domain.

A visual representation of the iterative FPM algorithm is shown in Figure 5.2 [52]. The FPM method begins (1) by making an initial guess of the high-resolution object function in the spatial domain $\sqrt{I_h}e^{i\varphi_h}$. A good starting point is to select $\varphi_h = 0$ and I_h as any oversampled low-resolution image. The Fourier transform of the initial guess creates a broad spectrum in the Fourier domain (Figure 5.2, up).

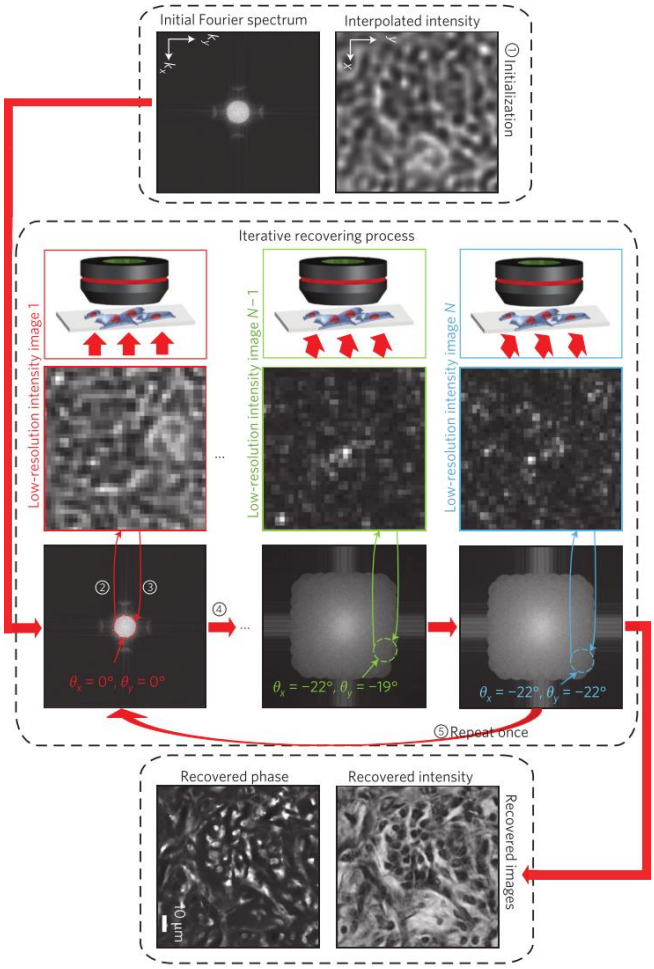

Figure 5.2. Iterative recovery procedure of FPM (five steps). N low-resolution intensity images captured under variable illumination are used to recover one high-resolution intensity image and one high-resolution phase map. Steps 1–5 illustrate the FPM algorithm, following principles from phase retrieval. Step 1: initialize the high-resolution image, $\sqrt{I_h}\, e^{i\varphi_h}$. *Step 2: generate a low-resolution image* $\sqrt{I_l}\, e^{i\varphi_l}$, *corresponding to an oblique plane-wave incidence. Step 3: replace* I_l *by the intensity measurement* I_{lm} *(that is,* $\sqrt{I_l}\, e^{i\varphi_l} \rightarrow \sqrt{I_{lm}}\, e^{i\varphi_l}$*), and update the corresponding region of* $\sqrt{I_h}\, e^{i\varphi_h}$ *in Fourier space (the area within the red circle). Step 4: repeat steps 2–3 for other plane-wave incidences (total of N intensity images). Step 5: repeat steps 2–4 once more* [52].

In the second step, we select a small subregion of this Fourier spectrum and apply Fourier transformation to generate a new low-resolution target image $\sqrt{I_l}e^{i\varphi_l}$ (2). The shape of this subregion is a circular pupil, whose characteristics are given by the coherent transfer function of the objective

lens, with a radius equal to $NA \times k_0$, where $k_0 = 2\pi/\lambda$ is the wavenumber in vacuum. The position of this low-pass filter is selected to correspond to a particular angle of illumination. Then, we replace the target image's amplitude component $\sqrt{I_l}$ with the square root of the low-resolution measurement obtained under illumination angle *i*, $\sqrt{I_{lm}}$, to form an updated low-resolution target image $\sqrt{I_{lm}}e^{i\varphi_l}$. We then apply Fourier transformation to this updated target $\sqrt{I_{lm}}e^{i\varphi_l}$ and replace its corresponding subregion of the high-resolution Fourier space (3). In other words, for $i = 1$, we updated the area enclosed by the red circle in Figure 5.2 with image $I_{lm} = (u^i, v^i)$ where $u^1 = 0$, $v^1 = 0$.

In the fourth step, we repeat steps 2 and 3 (select a small, circular region in Fourier space and update it with the measured image data) for other plane wave illuminations (green and blue circles in Figure 5.2, for example). Each shifted subregion corresponds to a unique, low-resolution intensity measurement $I_{lm}(u^i, v^i)$, and each subregion must overlap with neighbouring subregions to assure convergence. This iterative update continues for all N images, at which point the entire high-resolution image in Fourier space has been modified with data from all low-resolution intensity measurements.

Finally, steps 2-4 are repeated until a self-consistent solution is achieved. At the end of this iterative recovery process, the converged solution in Fourier space is transformed to the spatial domain to recover a high-resolution field $\sqrt{I_h e^{i\varphi_h}}$, offering an accurate image of the targeted two-dimensional sample (Figure 5.2, down) with high-resolution and wide FOV.

5.1 SINGLE-PIXEL DETECTION APPROACH

As already discussed in this work, in a conventional microscopy system, the object is illuminated by a uniform light source and the light reflected or transmitted by the object is recorded in a single shot by a pixelated detector. However, under certain conditions, for example, when

the amount of light is very low, it may be convenient to integrate the total intensity of the signal onto a single-pixel detector. This can be done by using raster scanning techniques or, alternatively, by projecting a sequence of microstructured light patterns, as is done in single-pixel microscopy. In these cases, the resolution of the final image is only limited by the wavelength and the numerical aperture (NA) of the optical system that projects the light patterns. A straightforward solution to improve the resolution is to use high-NA optical systems, but this is usually expensive and also reduces the image field of view (FOV). An alternative solution in order to increase resolution and maintain the FOV (that is, using a low NA objective) is to combine single-pixel imaging and Fourier ptychography techniques.

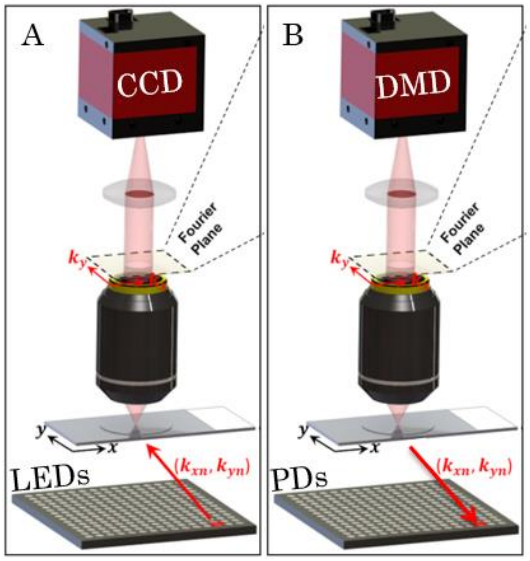

Figure 5.3. (A) Regular FPM configuration where an LED array sequentially illuminates the sample with different LED elements. Extracted from [157]. *(B) Our single-pixel Fourier ptychography proposal where a DMD sequentially illuminates the sample with different patterns while the intensity transmitted is collected by an array of PDs placed in the Fraunhofer diffraction plane.*

Taking advantage of the reversibility of light, here we propose to adapt the system of Fourier ptychography microscopy (Figure 5.3 A) for its operation with bucket detection by replacing the array of LEDs with an array of photodetectors located on the Fraunhofer diffraction plane (Figure 5.3 B). This new optical setup, that we call single-pixel Fourier

ptychography, allows us to project structured illumination patterns onto a sample and to measure the integrated transmitted intensity at the positions of each photodiode. In the next two sections we describe our single-pixel Fourier ptychography procedure for two types of structured illumination: raster scanning and Walsh-Hadamard illumination.

5.2 RASTER SCANNING FOURIER PTYCHOGRAPHY

Raster scan, or raster scanning, is a single-pixel imaging technique in which a laser beam is focused onto the sample. The laser beam sweeps horizontally left-to-right (for example) at a steady rate, then blanks and rapidly moves back to the left, where it turns back on and sweeps out the next line (Figure 5.4 left). Alternatively, the laser beam can remain turned on in its way back to the left, which allows to increase the speed of acquisition of the samples (Figure 5.4 right). The image is then built up pixel-by-pixel by collecting the reflected or transmitted photons from the sample onto a single-pixel detector.

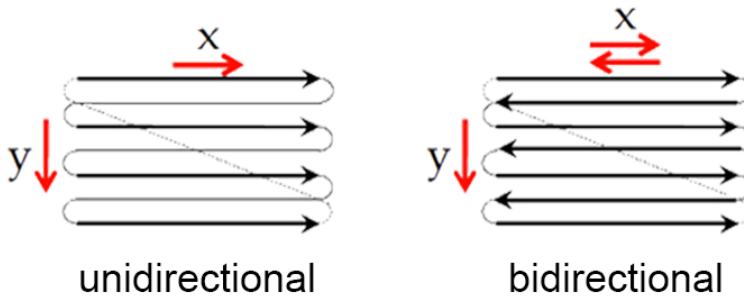

Figure 5.4. Laser beam path diagrams for unidirectional (left) and bidirectional (right) raster scanning modes.

In this section we propose a method to apply Fourier ptychography techniques to raster scanning microscopy, improving the resolution even when a low NA objective is used to generate the light point-source. To prove this statement, we performed computer simulations. In this simulations we use raster scanning to sample the object through a low NA objective, and an array of PDs to detect the diffracted light in Fourier domain.

The optical setup to perform raster scanning Fourier ptychography is shown schematically in Figure 5.5. The array of LEDs used in conventional Fourier ptychography has been substituted by an array of PDs. They are located at a distance from the object large enough to consider that they are at the Fraunhofer diffraction plane. The object is illuminated by a light spot focused by an objective with a low NA and scanned trough the sample. The scanning may be generated by a narrow light beam and a system of galvanometric mirrors or, alternatively, by using a SLM that scans pixel by pixel. In principle, the signal of a single PD, for example the central one, will be able to generate a low resolution image of the object. However, we propose to combine images obtained from different PDs, by using the Fourier ptychography algorithm, to obtain a high resolution image. Let us consider that the coherent PSF of the projection optical system is $a(x, y)$. Then, the complex amplitude reaching the PD located at spatial frequency coordinates (u, v) is

$$\alpha_{u,v}(x_i, y_i) = \sum_{x,y} a(x - x_i, y - y_i) \cdot O(x, y) \cdot e^{-j2\pi(ux+vy)}. \qquad (5.1)$$

The corresponding low resolution image $I_{lm}(u, v)$ is obtained by a simple superposition of the Dirac delta functions weighted by the intensity measured with the PD:

$$I_{lm}(u, v) = \sum_i \left|\alpha_{u,v}(x_i, y_i)\right|^2 \cdot \delta(x - x_i, y - y_i). \qquad (5.2)$$

Of course, because of the properties of the Delta function, this result is the same that the one obtained in equation (5.1), a low-resolution version of the object. This image will be equivalent to the one obtained by a camera in conventional Fourier ptychography when the corresponding LED at spatial frequencies (u, v) is on. Consequently, we can apply the same FP algorithm to obtain a high resolution image from the collection of low resolution images provided by the different PDs.

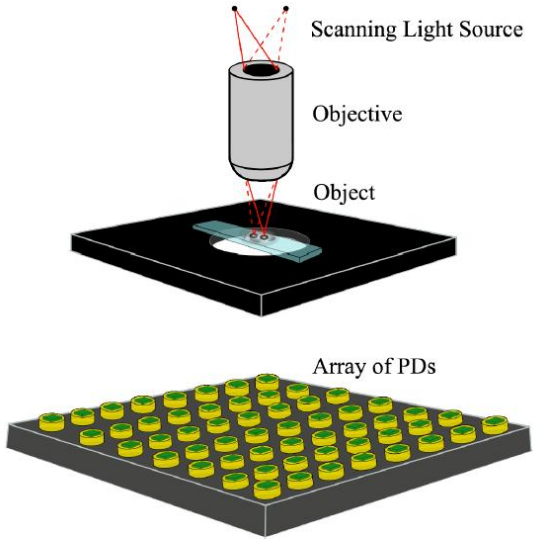

Figure 5.5: Schematic optical configuration for raster scanning Fourier ptychography.

To evaluate the behavior of our optical system for raster scanning FPM, we have simulated an array of 21×21 PDs with 2 mm separation between each two of them. The array was placed 200 mm far from the object and the object had a size of 0.1mm×0.1mm. Then, we captured images of the object using a low NA objective, which was simulated with a circular low-pass filter in Fourier domain. To put in context the results obtained with our raster scanning Fourier ptychography system, we have also carried out simulations of conventional raster scanning microscopy, using only one bucket detector exactly after the object, and conventional FPM (see Figure 5.6). For the conventional Fourier ptychography case, all the parameters were the same but now applied to an array of LEDs instead of photodiodes, and using a CCD camera detector conjugated with the object plane through the objective.

As we expected, the reconstructed image of raster scanning FP (Figure 5.6 c) and conventional FP (Figure 5.6 d) is exactly the same. Furthermore, both FP images have a much higher resolution than the image obtained by conventional raster scanning (Figure 5.6 b).

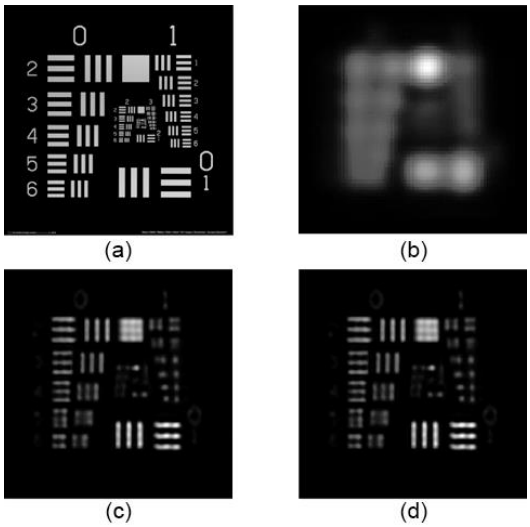

Figure 5.6. (a) Original object, a resolution test chart, and simulation results for (b) conventional raster scanning, (c) conventional Fourier ptychography and (d) raster scanning with Fourier ptychography, using in all cases a very low NA objective.

In summary, we have proposed a method to apply Fourier ptychography techniques to raster scanning microscopy, improving the resolution even when a low NA objective is used to generate the light point-source. In our method the LED array, typically used in FP techniques, is replaced by a PD array, and the CCD camera is replaced by a raster scanning technique. This proposal can provide high resolution images with large FOV, simultaneously, in raster scanning microscopy. Our technique can be interesting also in phase imaging techniques with raster scanning microscopy. However, raster scanning techniques may suffer from low efficiency, especially in cases where the amount of light projected onto the sample per unit area should be limited, for example to avoid damage in living samples or to reduce photobleaching in fluorescence applications. Single-pixel imaging techniques with structured pattern illumination can be the solution to this problem, as we discuss in the following section.

5.3 SINGLE-PIXEL FOURIER PTYCHOGRAPHY WITH PATTERN ILLUMINATION

Raster scanning techniques use a focused laser beam that allows the acquisition of digital images with very high resolution. This is due to the fact that the resolution is determined not by the PSF of the imaging system and the pixel size of the detector, as in conventional imaging, but by the size of the laser beam at the plane of the sample, which is determined by the PSF of the projection optics. However, under certain circumstances, for example when the sample cannot receive more than a certain amount of light per unit area (this is the case of biological or fluorescent samples) the signal reaching the detector may be insufficient to obtain an acceptable result. One way to increase light efficiency, without necessarily increasing the amount of light per unit area, is the use of wide-field illumination.

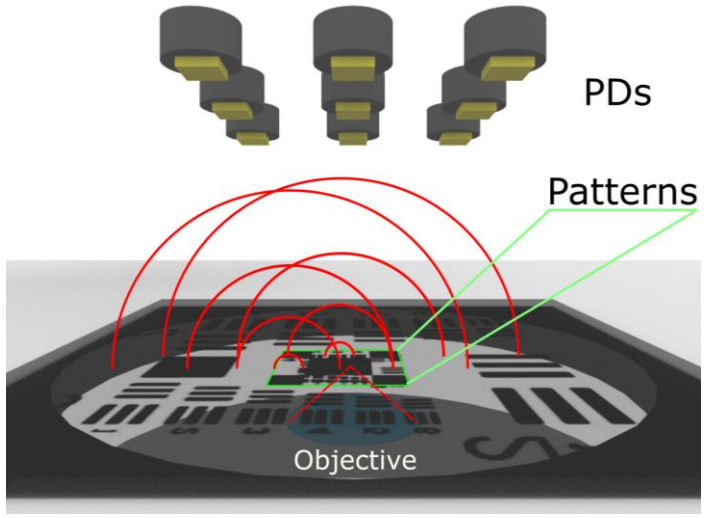

Figure 5.7. Schematic view of the projection system and measurement PDs in the single-pixel FP system. Only the ON pixels of the Hadamard patterns contribute to the complex summation of the light at the position of each PD.

In this section we propose the design of a new microscopy method based on the combination of Fourier ptychography techniques with wide-field microstructured illumination and integrated detection. As in the previous chapter, we use a digital micromirror device (DMD) designed to codify binary patterns (Walsh-Hadamard patterns) which are projected onto

the sample plane by a microscope optical system. The integrated detection is performed by an array of a low number of photodiodes or other single-pixel light detectors. In contrast with the raster scanning approach, now the standard FP algorithm cannot be applied directly, as we show next.

Let us consider the optical system sketched in Figure 5.8. As in the conventional single-pixel microscopy system described in the previous sections, an optical system is used to project microstructured light patterns onto the object plane. In this case, only the last element of the optical system, the microscope objective, is shown in Figure 5.8. The light field distribution at the object plane is given by

$$u_i(x,y) = [WH_i(x,y) \otimes a(x,y)] \cdot O(x,y) \qquad (5.3)$$

where $WH_i(x,y)$ is the *i*th Walsh-Hadamard pattern codified in the SLM; $a(x,y)$ is the coherent PSF of the projection optical system, and $O(x,y)$ is the transmittance of the object.

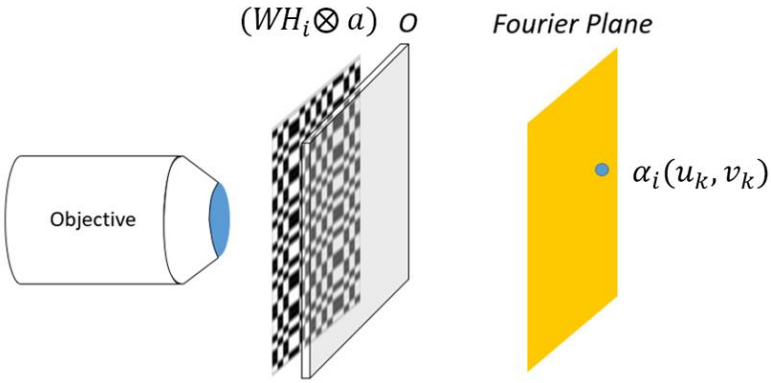

Figure 5.8. Schematic view of the projection system and measurement points in the single-pixel Fourier ptychography system.

In our approach, the detection system is constituted by an array of a low number of PDs located at the Fraunhofer diffraction plane of the optical system, in the same way as the LEDs are located in a conventional FP system. The complex amplitude distribution in this plane is just the Fourier transform of equation (5.3), i.e.,

$$\alpha_i(u_k, v_k) = \sum_{x,y} u_i(x,y) \cdot e^{-j2\pi(u_k x + v_k y)} = \sum_{x,y} [WH_i(x,y) \otimes a(x,y)] \cdot O_{u_k,v_k}(x,y)\,, \tag{5.4}$$

Note that $O_{u,v}(x,y) = O(x,y) \cdot e^{-j2\pi(ux+vy)}$ is the complex amplitude at the object plane $u_i(x,y)$ illuminated by tilted plane waves subtending angles θ_x and θ_y with the optical axis, and $u = k \sin\theta_x$ and $v = k \sin\theta_y$ represent frequency components along the x- and y-directions in a rectangular coordinate system. Equation (5.4) provides the complex amplitude of the light field arriving to the PD located at the spatial frequency coordinates (u_k, v_k), as is shown in Figure 5.8. By measuring experimentally the complex projections $\alpha_i(u_k, v_k)$, it will be possible to obtaining a low resolution version of the object as

$$O_{u_k,v_k}(x,y) = \sum_i \alpha_{u,v}(x_i, y_i) \cdot WH_i(x,y). \tag{5.5}$$

This would allow us to apply the conventional Fourier ptychography algorithm in a similar way as in the previous section. However, the PD measures just intensity $|\alpha_i(u_k, v_k)|^2$. This forces us to develop an algorithm for single-pixel Fourier ptychography adapted to work under wide-field structured illumination.

The first step is to measure $|\alpha_i(u_k, v_k)|$ but this is not straightforward because of the way we project the patterns experimentally. As each Walsh-Hadamard pattern WH_i contains positive and negative ± 1 values (see annex), it is not possible to codify them with a binary amplitude modulator. To this end, we codify positive patterns WH_i^+ and WH_i^- with only 0 and 1, in such a way that $WH_i = WH_i^+ - WH_i^-$. The coefficients associated to the Walsh-Hadamard pattern WH_i are then $\alpha_i = \alpha_i^+ - \alpha_i^-$, where α_i^+ is the value of the projection of WH_i^+, and α_i^- is the value of the projection of WH_i^-. From these two equations, we are able to calculate the module of the complex projection as follows:

$$|\alpha_i|^2 = |\alpha_i^+|^2 + |\alpha_i^-|^2 - 2(|\alpha_i^+|^2 \cdot |\alpha_i^-|^2),$$
$$|\alpha_1|^2 = |\alpha_i^+|^2 + |\alpha_i^-|^2 + 2(|\alpha_i^+|^2 \cdot |\alpha_i^-|^2), \quad (5.6)$$

where α_1 is the value of the projection when an all-white pattern, WH_1^+ is used. If we add $|\alpha_i|^2$ and $|\alpha_1|^2$, we obtain

$$|\alpha_i|^2 + |\alpha_1|^2 = 2(|\alpha_i^+|^2 + |\alpha_i^-|^2),$$
$$|\alpha_i| = \sqrt{2(|\alpha_i^+|^2 + |\alpha_i^-|^2) - |\alpha_1|^2}, \quad (5.7)$$

and since the square module of the complex projection is, by definition, the intensity, we obtain finally

$$|\alpha_i| = \sqrt{2(I_i^+ + I_i^-) - I_1}, \quad (5.8)$$

where I_i^+ and I_i^- are the *i*th intensity values measured by the photodiodes for the *i*th positive and negative Walsh-Hadamard patterns respectively.

The algorithm to obtain a high resolution image of the object from the single-pixel intensity measurements at the Fraunhofer plane is as follows. For each k-iteration, the algorithm (see Figure 5.9) receives two inputs: the object complex amplitude distribution, G^k (for simplicity we ignore the spatial coordinates (x, y) in the explanation of the algorithm), and the position of the detector in the Fraunhofer plane (u_k, v_k). As a starting point, we employ as initial guess G^0, the retrieved single-pixel image obtained from the measurements taken by the central PD. From this initial guess, we calculate the complex amplitude of the object as seen from the coordinates (u_k, v_k), that is, $O_{u_k,v_k}(1)$. From this first estimation of O_{u_k,v_k} we calculate numerically the complex values $\alpha_i(u_k, v_k)$ resulting from the projection of the different sampling patterns WH_i onto the object (2). In the next step, (3) we substitute the module of the complex value with the experimental measurement $|\alpha_{i,m}(u_k, v_k)|$, calculated with equation (5.8), while maintaining the phase. In this way, the experimental measurements allow us to update the value of the coefficients $\tilde{\alpha}_i(u_k, v_k)$ and therefore the complex distribution $O^I_{u_k,v_k}$ (4).

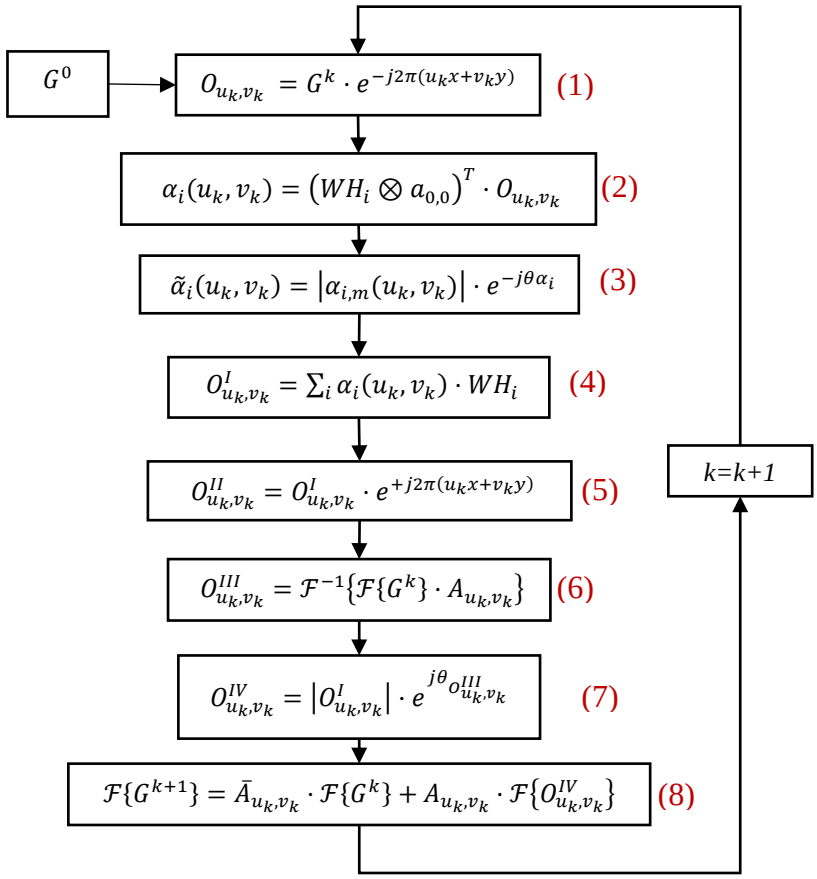

Figure 5.9. Iterative Single-pixel Fourier Ptychography algorithm.

Then, we calculate $O^{II}_{u_k,v_k}$ by multiplying $O^I_{u_k,v_k}$ with the linear phase $e^{+j2\pi(ux+uy)}$(5). In this way, $O^{II}_{u_k,v_k}$ is shifted back to its corresponding position in the Fourier plane. In step (6) we perform the Fourier transform of G^k and multiply it by a mask (A_{u_k,v_k}). This mask plays the role of the limited pupil aperture, the coherent transfer function, produced by the low aperture of the projection optical system. It selects only the information on the spatial-frequency plane in a circle with a size related with the NA of the projection system, shifted to the coordinates (u_k, v_k). Then we perform the inverse Fourier transform to complete the Fourier filtering operation. In the next step (7) we substitute in the previous estimation of the object $O^{III}_{u_k,v_k}$ the module of $O^I_{u_k,v_k}$ obtained in step (4), while keeping the phase,

obtaining a new provisional estimation of the object $O^{IV}_{u_k,v_k}$. Then, in Fourier space we substitute the information of $O^{IV}_{u_k,v_k}$ in the corresponding part of the Fourier space (by using the binary transfer function A_{u_k,v_k}), while leaving the rest intact ($\bar{A}_{u_k,v_k} = I_N - A_{u_k,v_k}$), where I_N is the $N \times N$ identity matrix (8). Finally, the inverse Fourier transform of (8) is considered as the guess for the following iteration.

In Figure 5.10 we show the result of a numerical simulation of a ptychographic SPM constituted by a light projection system, a low NA objective, and 9 PDs. The pictures show images retrieved from the measurements performed by the different PDs by using conventional single-pixel imaging techniques. For the reconstruction we use the real measurements $|\alpha|$ given by Eq. (5.8). We can see that high frequency information of the object is encoded in the off-axis images. The objective used in the simulation is a low NA objective with $NA = 0.4$. The simulated

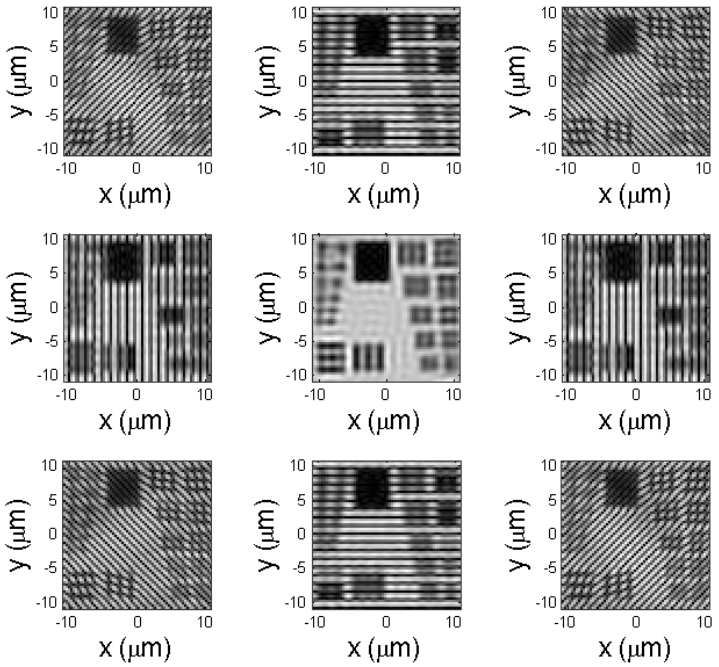

Figure 5.10. Simulation of the different images O_{u_k,v_k} (only amplitude) calculated from the signals measured by each of the 3x3 PDs using conventional SPI techniques. See text for details.

object is an USAF pattern with a resolution of 128×128 pixels and the projected patterns are Walsh-Hadamard functions obtained from Hadamard matrix $\mathcal{H}_{4096}$ (64×64 pixels) rescaled to 128×128 pixels.

The iterative single-pixel Fourier ptychography algorithm in Figure 5.9 is then applied to the set of measurements shown in Figure 5.10. The result of the simulation in shown in Figure 5.11. The left image shows the single-pixel image reconstructed with information from the central PD. The right image (ptychography image) shows the single-pixel Fourier ptychography image reconstructed with information from the array of 3x3 PDs. Note that in the single-pixel image, only element 1 of the biggest group is resolved. However, in the ptychographic image the element 6 of the same group is clearly resolved. This means a resolution increase factor of 1.8. These results have been obtained with 10 iterations of our algorithm. More iterations did not produce an image with better resolution.

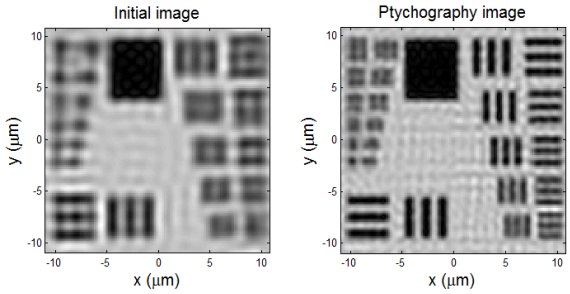

Figure 5.11. Results. (Left) Initial image obtained with the central PD. (Right) Fourier ptychography reconstruction using 3x3 PDs. The simulated objective is a 4X/0.4 NA and the images size 128×128 *pixels.*

In conclusion, in this chapter we have proposed a method to apply Fourier ptychography techniques to raster scanning and structured illumination single-pixel microscopy. Our system improves the resolution of the final images with respect those obtained with conventional single-pixel approaches even when a low NA objective is used to generate the structured illumination patterns. On one hand, the resolution of a raster scanning system has been improved using an array of photodetectors instead of only one, altogether with FP algorithms. Using numerical simulation, we have shown that the final image has a considerable higher

resolution with respect to conventional raster scanning, a resolution comparable with the one obtained by conventional Fourier ptychography techniques. On the other hand, we have shown that it is also possible to improve the resolution of structured illumination single-pixel microscopy using FP algorithms and an array of 3x3 photodetectors. By using a modified FP algorithm, we have shown that the final image obtained with the single-pixel Fourier ptychography technique has a factor of 1.8 better resolution than that one obtained with conventional single-pixel imaging. We believe that these ideas could be the key to improve the resolution and FOV in many other different applications of single-pixel imaging techniques.

Chapter 6. Conclusions

6.1 CONCLUSIONS

A challenge in microscopy is to capture high-resolution images at fast frame rates. Illumination plays an important role to achieve this goal. The last few decades have seen the evolution of new illumination techniques meant to improve certain imaging capabilities of the microscope. Confocal optical microscopy is a super-resolution technique that uses a single spot illumination pattern to scan the sample and a pinhole to reject out-of-focus light. Structured illumination and, more recently, image scanning microscopy have overcome the trade-off between lateral resolution and signal in confocal microscopy. These are examples of computational microscopy techniques where the final image is obtained computationally by combining the information contained in the whole dataset of the acquired signal either in the space or in the Fourier domain.

This thesis presented the principles and implementation of single-pixel imaging in microscopy. This approach is based on a patterned excitation of the sample combined with a point-detection of the signal so providing an improved signal-to-noise ratio. One of the main characteristics of the SPM is that it uses very simple sensors (bucket detectors such as photodiodes, photomultiplier tubes, ultrasonic transducers…) and mathematical algorithms to recover an image. SPM allocates the workload for spatial information over a set of microstructured spatial masks that are codified onto a DMD. DMDs offer high-resolution two-dimensional spatial light modulation based on an array of micromirrors. Although SLMs based on liquid crystal technology offer unprecedented control of amplitude and phase, they are typically limited to refresh rates of the order of 100 Hz. In contrast, micromirror devices are capable of at least 100 times faster switching, operating in the range of the tens of kHz. Another key feature is the broadband operation from the ultraviolet to the infrared. Current DMD technology offers data transfer speed to XGA chips of 52,5 kHz.

In this thesis we have designed and demonstrated several technologies for SPM. In particular:

•We have performed the analysis of the role of the point spread function in the illumination pathway corresponding to the objective lens of the projection system. In reality, the PSF acts as a low pass filter, meaning that the illumination patterns are smoother than the theoretical counterparts. This means that the retrieved computational image has the same resolution, both transversal and axial, than its widefield equivalent in conventional imaging.

•Our results also show that single-pixel systems applied to the field of microscopy can reduce the complexity of the optical collection system. We have demonstrated that there is no detrimental effect on the image quality for the point spread function in the collection pathway. In this way, we have demonstrated image transmission through scattering media; I mean the ability of the SPM to retrieve an image of the sample when there is a scattering layer between the sample and the detector.

•Compressive sensing allows one to acquire less data though still recover the same amount of information as traditional techniques, meaning less resources such as time, detector cost, power, data processing, and storage. We have demonstrated that compressive sensing allows to boost single-pixel microscopy to enable operating at video rates.

•We have demonstrated an optical design for a SPM that allows dual operation, meaning simultaneous imaging in transmission and reflection of the same area of the sample, with no need for calibration. In a traditional imaging system this should be done with a single illumination system and two identical, perfectly aligned imaging systems with the same optical characteristics. In this sense, we believe that our technique can play an important role in reducing the complexity of multimodal optical microscopy systems.

•Finally, we have proposed a novel algorithm to increase the transversal resolution in SPM through detection with a number of photosensors. To demonstrate the feasibility of our approach we use the

principle of light reversibility and the dual role between illumination in conventional imaging and detection in single-pixel imaging. Thus the discrete array of light sources in the conventional Fourier ptychography experiment is substituted by a discrete array of photosensors.

Although microscopy is a field that has been around for almost 400 years, the field of optical microscopy has new and exciting discoveries ahead. We firmly believe that the development of structured illumination techniques altogether with detectors with no spatial resolution is a hot area. Consequently, we are confident that the work presented in this thesis will shed light to improve of microscopy techniques based on single-pixel detection that will help reduce the complexity and cost of optical systems.

6.2 FUTURE WORK

In view of the satisfactory results achieved during the doctoral work, we foresee different lines for future research. On the one hand, optical imaging is an emerging sensing modality in the biomedical field due to its operational simplicity, no risk of ionizing radiation, high-resolution, and cost-effectiveness when compared with more conventional imaging tools such as ultrasound ecography, X-ray, MRI or PET (positron emission tomography). Despite the undeniable progress of imaging technologies, major challenges still remain. One of them is imaging deep inside complex (visually opaque) media. The problem is that visible and infrared light interact strongly with the tissue, preventing the formation of diffraction-limited images and limiting the penetration depth of light in tissues to roughly 1 mm. High-resolution microscopic imaging allows penetration depths smaller than 1 transport mean free path (TMFP), right beyond those achieved by the naked eye. Microscopic imaging techniques rely on the use of ballistic photons. Because of the statistical nature of light propagation, as the light travels through a diffusive medium, it is possible that some of the photons emerge without being scattered. By selecting these unscattered ballistic photons and rejecting the scattered (diffused) ones, it is possible to obtain high-resolution images that are the sharp shadows of targets buried in the diffusive medium. SPM and compressive sensing will allow to deal

with a number of questions that have to be addressed when using ballistic imaging in the mesoscopic region such as the exponential depletion of ballistic photons with the penetration depth or the loss of resolution due to the weakly scattered snake photons.

SPM relies on reconstruction algorithms that require a precise knowledge of the illumination patterns, with small errors in the latter yielding artifacts in the final high-resolution image. This important constraint cannot be overstated if illumination distortion induced by the sample or objective aberrations are present. Recently, it has been proposed a blind-SIM algorithm that is able to retrieve the sample without a priori knowledge of the illumination patterns in wide-field fluorescence imaging [159]. We foresee to develop its counterpart for single-pixel imaging. It would greatly extend the possibilities of SPM by eliminating the need of an a priori knowledge of the input patterns required in the current implementation.

6.3 LIST OF PUBLICATIONS

The following publications and works are part of this thesis. They will be cited using roman numerals. The published works are included at the end of this thesis.

Publications in Journals indexed in JCR

[I] A. D. Rodríguez, P. Clemente, E. Irles, E. Tajahuerce, and J. Lancis, (2014).
Resolution Analysis in Computational Imaging with Patterned Illumination and Bucket Detection.
Optics Letters, 39, 3888-91.

[II] A. D. Rodríguez, P. Clemente, E. Tajahuerce, and J. Lancis, (2016).
Dual-mode optical microscope based on single-pixel.

Optics and Lasers in Engineering, 82, 87-94.

In preparation for publication in Journals indexed in JCR

[III] E. Irles, P. Clemente, A. D. Rodríguez, E. Tajahuerce, B. Lochocki, A. Gambín, P. Artal, and J. Lancis,
Double-pass single-pixel imaging through scattering media.

[IV] A. D. Rodríguez, S.M.M. Khamousi, P. Clemente, E. Tajahuerce, and J. Lancis,
Single-pixel Fourier Ptychography.

[V] E. Salvador-Balaguer, A. D. Rodríguez, P. Clemente, E. Tajahuerce, and J. Lancis,
Single-pixel imaging with high-speed LED matrix projection.

Proceedings included in Web of Science

[VI] A. D. Rodríguez, E. Irles, P. Clemente, E. Tajahuerce, and J. Lancis, (2014).
Resolution Analysis in Computational Imaging with Patterned Illumination and Single-pixel Detection.
Proc. SPIE. 9286, Second International Conference on Applications of Optics and Photonics, 92864X. (August 22, 2014) doi: 10.1117/12.2063623

[VII] A. D. Rodríguez, P. Clemente, E. Salvador-Balaguer, E. Irles, E. Tajahuerce, F. Soldevila, and J. Lancis, (2014).
Resolution imaging in compressive multidimensional microscopy.
Proc. SPIE. 9330, Three-Dimensional and Multidimensional Microscopy: Image Acquisition and Processing XXII, 93301O. (March 09, 2015) doi: 10.1117/12.2079477

[VIII] V. Durán, P. Clemente, E. Irles, F. Soldevila, E. Tajahuerce, A. D. Rodríguez, P. Andrés, and J. Lancis, (2014).
Structured illumination enables image transmission through scattering media.
Proc. SPIE. 9335, Adaptive Optics and Wavefront Control for Biological Systems, 93350V. (March 10, 2015) doi: 10.1117/12.2079445

Attendance to national and international congresses

[IX] A. D. Rodríguez, P. Clemente, E. Irles, E. Tajahuerce, and J. Lancis,
Resolution Analysis in Computational Imaging with Patterned Illumination and Single-pixel Detection.
International Conference on Applications of Optics and Photonics (AOP 2014)

[X] A. D. Rodríguez, P. Clemente, E. Irles, E. Tajahuerce, and J. Lancis,
Resolution analysis in computational imaging with Hadamard illumination and single-pixel detection.
23rd International Commission for Optics (ICO23 2014).

[X] A. D. Rodríguez, P. Clemente, E. Irles, F. Soldevila, E. Salvador, E. Tajahuerce, and J. Lancis,
Resolution analysis in compressive multidimensional microscopy.
SPIE Biomedical Optics Conference (BIOS 2015)

[XI] V. Durán, P. Clemente, E. Irles, F. Soldevila, E. Tajahuerce, A. D. Rodríguez, P. Andrés, and J. Lancis,
Structured illumination enables image transmission through scattering media.
SPIE Biomedical Optics Conference (BIOS 2015)

[XII] A. D. Rodríguez, P. Clemente, E. Irles, E. Tajahuerce, M. Fernández-Alonso, and J. Lancis,
Dual collection mode optical microscope with single-pixel detection.
European Conferences on Biomedical Optics 2015 (ECBO 2015)

[XIII] S. M. M. Khamousi, S. H. Tavassoli, A. D. Rodríguez, P. Clemente, E. Tajahuerce, and J. Lancis,
Improving resolution in raster scanning microscopy using Fourier ptychography.
Computational Optical Sensing and Imaging (COSI 2016)

[XIV] A. D. Rodríguez, P. Clemente, S.M.M, Khamousi, S.H. Tavassoli, E. Tajahuerce, and J. Lancis,
Improving resolution in single-pixel microscopy by using Fourier ptychography
European Conferences on Biomedical Optics 2017 (ECBO 2017)

Others

[XX] Visitor student at Boston University. Computational Imaging System Lab. September 2016-December 2016. Advisor: Dr. Lei Tian.
Study of the improvement of spatial resolution in single-pixel sensor imaging techniques by implementing ptychography algorithms.

Annex: Hadamard Matrices, Walsh Functions, and Walsh -Hadamard Functions

A Hadamard matrix of order $\mathcal{H}_N$ is a $N \times N$ matrix of 1s and -1s that fulfills [160]

$$\mathcal{H}_N \cdot \mathcal{H}_N^T = N \cdot I_N, \qquad (A.1)$$

where T denotes transposed and I_N is the $N \times N$ identity matrix.

Among the large number of procedures for creating Hadamard matrices is the Sylvester construction, which obtains Hadamard matrices of order 1, 2, 4, 8… recursively from

$$\mathcal{H}_1 = (1) \qquad \text{and} \quad \mathcal{H}_{2N} = \begin{pmatrix} \mathcal{H}_N & \mathcal{H}_N \\ \mathcal{H}_N & -\mathcal{H}_N \end{pmatrix}. \qquad (A.2)$$

A frequency interpretation can be given to the Hadamard matrix. We call frequency to the number of sign changes that exist along each row. For example, in the matrix

$$\mathcal{H}_4 = \begin{pmatrix} +1 & +1 & +1 & +1 \\ +1 & -1 & +1 & -1 \\ +1 & -1 & -1 & -1 \\ +1 & -1 & -1 & +1 \end{pmatrix}, \qquad (A.3)$$

the frequencies of the rows are $f_1 = 0, f_2 = 3, f_3 = 1$ and $f_4 = 2$ respectively. Then, the set of rows can be considered as a basis of rectangular 1D functions, called Walsh functions. In this context, the Hadamard matrix merely performs the decomposition of a function into a

set of rectangular functions, much like the Fourier transform in a set of sinusoidal functions [161].

In digital image processing it is usual to consider a 2D image as a 1D vector, which expresses the set of image rows concatenated in a single vector. This correspondence can be applied between the Walsh (W) functions and the 2D functions, called Walsh-Hadamard (WH). Thus, for example, in H_4,

$$\begin{aligned} W_1 &= (+1 \quad +1 \quad +1 \quad +1) \quad \Leftrightarrow \quad WH_1 = \begin{pmatrix} +1 & +1 \\ +1 & +1 \end{pmatrix} \\ W_2 &= (+1 \quad -1 \quad +1 \quad -1) \quad \Leftrightarrow \quad WH_2 = \begin{pmatrix} +1 & -1 \\ +1 & -1 \end{pmatrix} \\ W_3 &= (+1 \quad +1 \quad -1 \quad -1) \quad \Leftrightarrow \quad WH_3 = \begin{pmatrix} +1 & +1 \\ -1 & -1 \end{pmatrix} \\ W_4 &= (+1 \quad -1 \quad -1 \quad +1) \quad \Leftrightarrow \quad WH_4 = \begin{pmatrix} +1 & -1 \\ -1 & +1 \end{pmatrix}. \end{aligned} \qquad \textit{(A.4)}$$

According to frequency interpretation, these Walsh-Hadamard functions have frequencies in two directions (x, y). For example, for WH_1, WH_2, WH_3 and WH_4 the frequencies are $f_1 = (0,0)$, $f_2 = (1,0)$, $f_3 = (0,1)$ and $f_4 = (1,1)$ respectively. In addition, it can also be said that the Hadamard matrix of $N \times N$ dimension contains the base of 2D Walsh-Hadamard function, the dimension of which is $\sqrt{N} \times \sqrt{N}$.

In the modulation of light beams through Walsh-Hadamard functions two cases are considered, depending on whether the electric field or intensity is modulated. In the first case, the implementation of Walsh-Hadamard functions is performed by a SLM that modulates only phase, assigning the phase 0 for the 1s of the function and π for the -1s. For this type of modulation both transmission and reflection SLM can be used. However, when modulating intensity, the implementation of the Walsh-Hadamard functions is not direct since the modulator has to be formed by elements of transmittance 1 and -1. Then, the modulator has to transmit part of the incident radiation and reflect the rest, or reflect the incident light beam in two different directions, as is done by a DMD, being necessary two photodetectors [160].

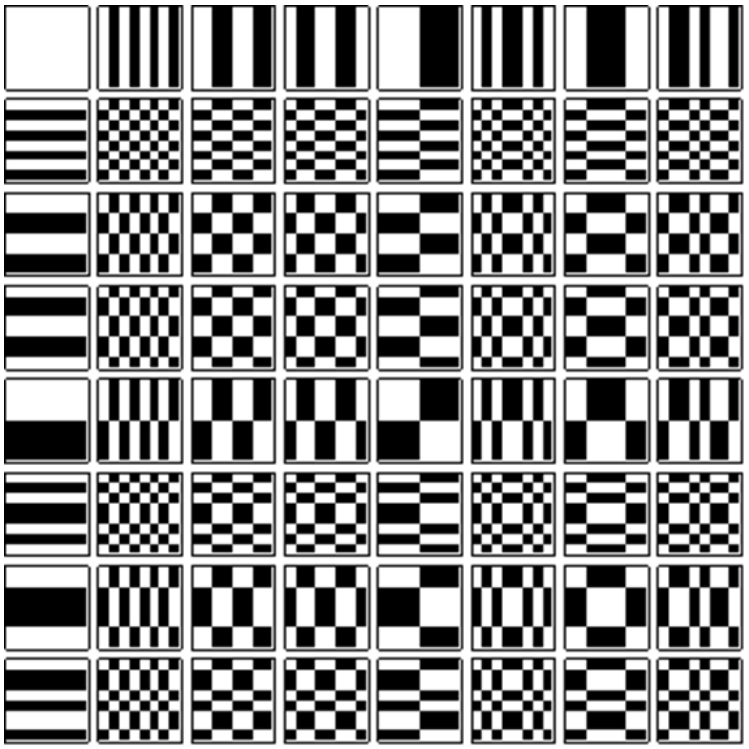

Figure A.1. Representation of Walsh-Hadamard functions obtained from the Hadamard matrix $\mathcal{H}_{64}$ as 8x8 pixel images. The 1s are represented by white pixels and the -1s by black pixels.

In contrast, if the modulator used only reflects or transmits radiation, it is necessary to decompose the Walsh-Hadamard functions into other functions implementable in the modulator. Thus, any Walsh-Hadamard function can be expressed as the subtraction of two complementary functions

$$WH_n = WH_n^+ - WH_n^-, \qquad (A.5)$$

where WH_n^+ is built from WH_n replacing the -1s by 0 and WH_n^- is the complementary of WH_n^+. These functions are easy to implement with an SLM since it only contains pixels of transmittance 1 or 0. In addition, from

the measured projections α^+ and α^- the projection associated with the WH function can be calculated as

$$\alpha = \alpha^+ - \alpha^-. \qquad (A.6)$$

The need of projection α_i^+ and α^- for each WH_n may mean a priori having to double the number of patterns sent experimentally. However, this is not always necessary. Since WH_n^+ and WH_n^- are complementary

$$WH_n^+ + WH_n^- = WH_1 \qquad n \neq 1, \qquad (A.7)$$

where WH_1 is the element of the basis of Walsh-Hadamard functions where all elements are 1. Thus, from equations (A.5) and (A.7)

$$WH_n = WH_n^+ - WH_n^- = 2 \cdot WH_n^+ - WH_1, \qquad (A.8)$$

and then, the projections of WH_n can be calculated as

$$\alpha_n = 2 \cdot \alpha_n^1 - \alpha_1 \qquad n \neq 1. \qquad (A.9)$$

In other words, if the total intensity is kept constant throughout the experiment (i.e., the light source does not oscillate), it is not necessary to double the number of patterns projected onto the object.

Resumen en español

MOTIVACIÓN Y OBJETIVOS DE LA INVESTIGACIÓN.

En microscopía es posible distinguir diferentes tipos de estrategias de formación de imágenes en términos de sus modos de excitación y detección (ver Tabla R.1). Por un lado, en microscopía de campo claro, se ilumina un área grande de la muestra y la luz difractada se registra mediante una serie de fotosensores montados sobre una plataforma digital, como un sensor CCD o CMOS. Por el contrario, en microscopía de barrido, se escanea un punto de luz a través de la muestra y se usa un solo fotosensor para detectar la señal pixel a pixel. Además, en microscopía de escaneo de imágenes (ISM), el detector puntual en un microscopio confocal convencional se reemplaza por una matriz de detectores para aumentar la extremadamente baja SNR [48,82].

El esquema de imagen con detección puntual (SPI) [83] ha ganado considerable atención como mecanismo de detección muy eficaz y ha desencadenado diversas aplicaciones donde las cámaras convencionales equipadas con millones de píxeles no dan una respuesta adecuada, incluida la microscopía óptica. En la microscopía de un solo pixel (SPM), la muestra se ilumina con patrones proyectados a través de un objetivo y la señal es colectada en un sensor puntual [84–90]. Las imágenes son reconstruidas computacionalmente a partir de las fotocorrientes correspondientes a un conjunto de patrones adecuadamente elegidos. La técnica de SPM ha permitido imágenes hiperespectrales a través del espectro visible en un microscopio de fluorescencia e imagen de microfluidos [60,70]. También se ha demostrado recientemente un prototipo de sistema de microscopía basado en SPI para imagen simultánea en infrarrojo y visible [69]. La longitud de onda juega un papel importante en la formación de imágenes biológicas. Por ejemplo, las longitudes de onda localizadas en el infrarrojo cercano tienen una penetración máxima en el tejido biológico. Esta ventana, también conocida como ventana terapéutica o ventana NIR, está limitada principalmente por la absorción de la luz por la sangre en longitudes de onda más cortas y por el agua en longitudes de onda más largas.

		Excitación	
		Campo claro	**Pixel a pixel**
Detección	**Matriz de detectores**	Microscopía de campo claro	Microscopía de escaneo de imagen
	Detector puntual	**Microscopía single-pixel**	Microscopía de barrido

Tabla R.1. Clasificación de las modalidades de microscopía según su configuración de iluminación y detección.

En esta Tesis, exploramos la técnica de SPM para diseñar y desarrollar experimentos de prueba de concepto donde la estrategia de detección de un solo pixel supera la detección convencional con sensores pixelados típica de la microscopía de campo claro. La capacidad de la estrategia de detección puntual para generar imágenes de un objeto oculto por medios con elevada dispersión ha sido demostrada recientemente. Sorprendentemente, un sensor sin resolución espacial es capaz de recuperar una imagen de alta resolución de una muestra oculta por un medio turbio, un problema que no puede resolverse con cámaras convencionales CCD o CMOS equipadas con millones de píxeles. De esta manera, recuperamos el equilibrio fundamental entre la profundidad de penetración, la sensibilidad y la velocidad de imagen de los microscopios actuales mediante un cambio en el paradigma de la estrategia de detección.

Además, se desarrolla el análogo a la microscopía con pticografía de Fourier pero empleando técnicas de imagen con detección de un solo píxel. Este método, es una combinación inteligente de técnicas de recuperación de fase y de apertura sintética. La técnica consiste en emplear una matriz de LEDs, en una posición relativamente alejada del objeto, que ilumina secuencialmente la muestra desde diferentes ángulos. Un objetivo de baja apertura numérica forma las imágenes del objeto sobre una cámara. Como la posición de los LEDs se asume lo suficientemente alejada del objeto, la iluminación de cada LED puede considerarse como una onda plana inclinada con un ángulo diferente. Estas ondas planas inclinadas

causarán un cambio en el espectro del objeto en el dominio de Fourier. Por lo tanto, cada imagen registra información de diferentes áreas del espectro de Fourier del objeto. Mediante el uso de un algoritmo iterativo, similar a los utilizados en las técnicas de recuperación de fase, es posible combinar la información contenida en estas áreas para obtener una imagen de alta resolución con un gran campo de visión (FOV). Además de alta resolución y un amplio FOV, este método permite obtener la distribución de fase del objeto.

La estructura de la Tesis es la siguiente:

I. En el **Capítulo 2** introducimos los conceptos básicos y herramientas matemáticas para entender SPI y CS, analizando las principales diferencias entre cámaras convencionales y cámaras de un solo pixel. Además, revisamos las principales características de los diferentes moduladores espaciales de luz y fotodetectores utilizados para construir nuestro SPM. En el **Capítulo 3**, describimos el sistema SPM y realizamos un análisis detallado de la resolución espacial, tanto en las coordenadas transversales como axiales, utilizando la óptica de Fourier.

II. En el **Capítulo 4** desarrollamos un microscopio dual que permite obtener imágenes de muestras en reflexión y transmisión de forma simultánea. La mayoría de diseños de microscopios ópticos hacen que la obtención simultánea de la imagen de una muestra en transmisión y reflexión sea ineficiente, restrictiva o incluso imposible. Aquí demostramos que la arquitectura de SPM es particularmente adecuada para esta operación dual, ya que ambas imágenes pertenecen, inequívocamente, al mismo plano de la muestra. El sistema se basa en el uso de un DMD perteneciente a un videoproyector comercial de bajo coste que utiliza un diseño de mosaico de píxeles en forma de diamante. Para hacer frente a las distorsiones geométricas generadas por este diseño de diamante, se hace necesario desarrollar un algoritmo para precompensar los patrones, asignando con precisión píxeles en la memoria del dispositivo.

III. En el **Capítulo 5** extendemos las capacidades de la microscopía de barrido y SPI combinando estas técnicas con algoritmos adaptados de pticografía de Fourier para desarrollar un sistema SPM de transmisión. En estos experimentos, extendemos virtualmente la apertura numérica del sistema usando una matriz de fotodetectores colocados en el plano de Fraunhofer. Finalmente, en el **Capítulo 6** resumimos las principales conclusiones de esta tesis doctoral y esbozamos las principales vías para el trabajo futuro.

CONCLUSIONES

Un desafío en microscopía es obtener imágenes de alta resolución con tasas de repetición altas. La iluminación juega un papel importante para conseguir este objetivo. Las últimas décadas han visto una evolución de nuevas técnicas de iluminación diseñadas para mejorar ciertas capacidades de los microscopios. La microscopía óptica confocal es una técnica de superresolución que utiliza un único patrón de iluminación puntual para escanear la muestra y un *pinhole* para rechazar la luz fuera de foco. Las técnicas de iluminación estructurada y, más recientemente, las de microscopía de escaneado de imagen, han superado el compromiso entre resolución lateral y nivel de señal en microscopía confocal. Estos son ejemplos de técnicas de imagen computacional donde la imagen final es obtenida computacionalmente combinando información contenida en el conjunto de datos de la señal adquirida ya sea en el dominio espacial o en el de Fourier.

En esta Tesis hemos descrito los principios y aplicaciones de las técnicas de SPI en microscopía. Este enfoque se basa en la iluminación de la muestra mediante patrones de luz combinada con la detección puntual de la señal, proporcionando así una relación señal-ruido mejorada. Una de las principales características de la técnica de SPM es el uso de sensores muy simples (detectores puntuales como fotodiodos, tubos fotomultiplicadores, transductores ultrasónicos…) y algoritmos matemáticos para recuperar una imagen. La microscopía basada en SPI determina la información espacial

mediante un conjunto de máscaras microestructuradas que están codificadas en un SLM. Los DMDs permiten la modulación de la luz con alta resolución mediante una matriz de microespejos. Aunque los SLMs basados en tecnología de cristal líquido ofrecen un control de amplitud y fase sin precedentes, están limitados típicamente a una tasa de refresco máxima del orden de los 100 Hz. Por el contrario, los dispositivos de microespejos son capaces de conmutar al menos 100 veces más rápido, operando en el rango de las decenas de kHz. Otra característica clave es su ancho de banda de operación desde el ultravioleta al infrarrojo. La tecnología actual de los DMD ofrece velocidades de transferencia de datos a chips XGA de 52,6 kHz.

En esta Tesis hemos diseñado y demostrado varias tecnologías para SPM. En particular:

- Hemos realizado un análisis del papel de la PSF en el sistema de iluminación que proyecta los patrones de luz micro-estructurados sobre la muestra mediante el objetivo de proyección. En realidad, la PSF actúa como un filtro pasa baja, lo que significa que los patrones de iluminación son más suaves que las funciones de la base teóricas. Esto significa que la imagen computacional recuperada tiene la misma resolución, tanto transversal como axial, que su equivalente en campo ancho obtenida con técnicas convencionales.

- Nuestros resultados también muestran que los sistemas de un solo pixel aplicados al campo de microscopía pueden reducir la complejidad del sistema óptico de colección. Hemos demostrado que no hay un efecto perjudicial sobre la calidad de imagen por la PSF en el sistema de colección. De esta manera, hemos comprobado la transmisión de imágenes a través de medios turbios. Con esto nos referimos a la capacidad de la técnica de SPM de recuperar una imagen de la muestra cuando hay una capa con dispersión elevada entre la muestra y el detector.

- Los métodos de CS permiten adquirir menos datos y, aun así, recuperar la misma cantidad de información que con técnicas convencionales, lo que se traduce en el consumo de menos recursos tales como el tiempo de medida, el coste del detector, la potencia eléctrica y el procesamiento de datos y almacenamiento de los mismos. Hemos demostrado que las técnicas de CS permite acelerar las operaciones de los sistemas de SPM, permitiendo el funcionamiento a velocidades de vídeo.

- Hemos desarrollado un diseño óptico para SPM que permite la operación dual, esto es, la imagen simultánea en transmisión y reflexión de la misma área de la muestra, sin necesidad de calibración. En un sistema tradicional de imagen esto debe hacerse con un sistema de iluminación y dos sistemas de imagen idénticos, perfectamente alineados y de las mismas características ópticas. En este sentido, creemos que nuestra técnica puede jugar un papel importante al reducir la complejidad en sistemas de microscopía multimodal.

- Finalmente, hemos propuesto un algoritmo nuevo para aumentar la resolución transversal de las técnicas de SPM a través de la detección con una matriz de fotodetectores. Para demostrar la viabilidad de nuestra propuesta, utilizamos el principio de reversibilidad de la luz y el papel dual entre la iluminación en sistemas de imagen convencional y la detección en sistemas de un solo pixel. Así, el conjunto discreto de fuentes de luz usado en pticografía de Fourier convencional es sustituido por una matriz discreta con un número reducido de fotodetectores.

Aunque la microscopía es un campo que ha existido durante 400 años, el campo de la microscopía óptica tiene descubrimientos nuevos y emocionantes por delante. Creemos firmemente que el desarrollo de

técnicas de iluminación estructurada en conjunto con detectores sin resolución espacial es un tema candente. En consecuencia, estamos seguros de que el trabajo presentado en esta Tesis arrojará luz para mejorar las técnicas de microscopia basadas en la detección con un solo pixel, lo que ayudará a reducir la complejidad y coste de estos sistemas ópticos.

References

1. R. Sheppard and T. Wilson, "Theory and Practice of Scanning Optical Microscopy," Acad. Press 331–342 (1984).

2. J. B. Pawley, "Confocal and two-photon microscopy: Foundations, applications and advances," Microsc. Res. Tech. **59**, 148–149 (2002).

3. R. Yuste, A. Konnerth, and B. R. Masters, "Imaging in Neuroscience and Development, A Laboratory Manual," J. Biomed. Opt. **11**, 19902 (2006).

4. R. Weissleder and M. J. Pittet, "Imaging in the era of molecular oncology," Nature **452**, 580–589 (2008).

5. C. K. Kao, W. S. Boyle, and G. E. Smith, "The Nobel Price in Physics," http://www.nobelprize.org/nobel_prizes/physics/laureates/2009.

6. J. W. Lichtman and J. Conchello, "Fluorescence microscopy," Nat. Methods **2**, 910–919 (2005).

7. M. Minsky, "Microscopy Apparatus," US Pat. 3013467 **3013467**, 5 (1957).

8. A. D. Rodriguez, "Impacto de las aberraciones en imágenes de microscopía multifotónica," Universidad de Murcia (2012).

9. W. Denk, J. H. Strickler, and W. W. Webb, "The Nobel Prize in Chemistry," https://www.nobelprize.org/nobel_prizes/chemistry/laureates/2014.

10. S. W. Hell and J. Wichmann, "Breaking the diffraction resolution limit by stimulated emission: stimulated-emission-depletion fluorescence microscopy," Opt. Lett. **19**, 780–782 (1994).

11. S. W. Hell, "Microscopy and its focal switch," Nat. Methods **6**, 24–32 (2009).

12. W. E. Moerner, "Single-molecule mountains yield nanoscale cell images," Nat. Methods **3**, 781–782 (2006).

13. E. Betzig, G. H. Patterson, R. Sougrat, O. W. Lindwasser, S. Olenych, J. S. Bonifacino, M. W. Davidson, J. Lippincott-Schwartz, et al., "Imaging intracellular fluorescent proteins at nanometer resolution," Science **313**, 1642–1645 (2006).

14. M. Saxena, G. Eluru, and S. S. Gorthi, "Structured illumination microscopy," Adv. Opt. Photonics **6**, 293–339 (2014).

15. M. G. Gustafsson, "Extended resolution fluorescence microscopy," Curr. Opin. Struct. Biol. **9**, 627–634 (1999).

16. F. Ströhl and C. F. Kaminski, "Frontiers in structured illumination microscopy," Optica **3**, 667 (2016).

17. A. Jost and R. Heintzmann, "Superresolution Multidimensional Imaging with Structured Illumination Microscopy," Annu. Rev. Mater. Res. **43**, 261–282 (2013).

18. J. R. Allen, S. T. Ross, and M. W. Davidson, "Structured illumination microscopy for superresolution," Chemphyschem **15**, 566–76 (2014).

19. P. A. Santi, "Light Sheet Fluorescence Microscopy A Review," J. Histochem. Cytochem. **59**, 129–138 (2011).

20. J. Andilla, R. Jorand, O. E. Olarte, A. C. Dufour, M. Cazales, Y. L. E. Montagner, R. Ceolato, N. Riviere, et al., "Imaging tissue-mimic with light sheet microscopy: A comparative guideline," Sci. Rep. **7**, 44939 (2017).

21. M. Shtrahman, D. B. Aharoni, N. F. Hardy, D. V. Buonomano, K. Arisaka, and T. S. Otis, "Multifocal fluorescence microscope for fast optical recordings of neuronal action potentials," Biophys. J. **108**, 520–529 (2015).

22. E. Conference, I. Quantum, E. Conference, C. Digest, E. Europe, and R. Permissions, "Scanless two-photon microscopy with a 30 fs laser by means of a diffractive dispersion compensation module," 2–3 (2013).

23. M. Dal Maschio, F. Difato, R. Beltramo, A. Blau, F. Benfenati, and T. Fellin, "Simultaneous two-photon imaging and photo-stimulation with structured light illumination," Opt. Express **18**, 18720 (2010).

24. K. Goda, K. K. Tsia, and B. Jalali, "Serial time-encoded amplified imaging for real-time observation of fast dynamic phenomena," Nature **458**, 1145–1149 (2009).

25. C. Maurer, A. Jesacher, S. Bernet, and M. Ritsch-Marte, "What spatial light modulators can do for optical microscopy," Laser Photon. Rev. **5**, 81–101 (2011).

26. V. Durán, *Optimización Del Funcionamiento de Un Modulador Espacial de Luz de Cristal Líquido Mediante El Modelo*

Retardador-Rotor. Aplicaciones En Óptica Adaptativa (Universitat Jaume I, 2008).

27. R. K. Tyson, *Principles of Adaptive Optics* (2010), Vol. 1.

28. E. J. Fernández, P. M. Prieto, and P. Artal, "Wave-aberration control with a liquid crystal on silicon (LCOS) spatial phase modulator," Opt. Express **17**, 11013–11025 (2009).

29. M. Cui, "Parallel wavefront optimization method for focusing light through random scattering media," Opt. Lett. **36**, 870 (2011).

30. M. J. Booth, D. Débarre, A. Jesacher, and D. D. and A. J. Martin J. Booth, "Adaptive Optics for Biomedical Microscopy," OPN Opt. Photonics News **23**, 22–29 (2012).

31. J. Tang, R. N. Germain, and M. Cui, "Superpenetration optical microscopy by iterative multiphoton adaptive compensation technique," Proc. Natl. Acad. Sci. **109**, 8434–8439 (2012).

32. J. M. Bueno, M. Skorsetz, R. Palacios, E. J. Gualda, and P. Artal, "Multiphoton imaging microscopy at deeper layers with adaptive optics control of spherical aberration," J. Biomed. Opt. **19**, 11007 (2014).

33. D. Huang, E. A. Swanson, C. P. Lin, J. S. Schuman, W. G. Stinson, W. Chang, M. R. Hee, T. Flotte, et al., "Optical coherence tomography," Science. **254**, 1178–1181 (1991).

34. J. Schmitt, "Optical Coherence Tomography (OCT): A Review," IEEE J. Sel. Top. Quantum Electron. **5**, 1205–1215 (1999).

35. V. Ntziachristos, "Going deeper than microscopy: the optical imaging frontier in biology," Nat. Methods **7**, 603–14 (2010).

36. I. M. Vellekoop and A. P. Mosk, "Focusing coherent light through opaque strongly scattering media," Opt. Lett. **32**, 2309–2311 (2007).

37. J. Bertolotti, E. G. van Putten, C. Blum, A. Lagendijk, W. L. Vos, and A. P. Mosk, "Non-invasive imaging through opaque scattering layers," Nature **491**, 232–234 (2012).

38. A. P. Mosk, A. Lagendijk, G. Lerosey, M. Fink, G. Lerosey, A. Lagendijk, and A. P. Mosk, "Controlling waves in space and time for imaging and focusing in complex media," Nat. Photonics **6**, 283–292 (2012).

39. B. Lee, "DMD 101: Introduction to Digital Micromirror Device (DMD) Technology," Appl. Rep. (2008).

40. Y. X. Ren, R. De Lu, and L. Gong, "Tailoring light with a digital micromirror device," Ann. Phys. **527**, 447–470 (2015).

41. D. Dan, M. Lei, B. Yao, W. Wang, M. Winterhalder, A. Zumbusch, Y. Qi, L. Xia, et al., "DMD-based LED-illumination Super-resolution and optical sectioning microscopy," Sci. Rep. **3**, 1116 (2013).

42. L.-C. Cheng, C.-H. Lien, Y. Da Sie, Y. Y. Hu, C.-Y. Lin, F.-C. Chien, C. Xu, C. Y. Dong, et al., "Nonlinear structured-illumination enhanced temporal focusing multiphoton excitation microscopy with a digital micromirror device," Biomed. Opt. Express **5**, 2526–2536 (2014).

43. M. Ducros, Y. Goulam Houssen, J. Bradley, V. de Sars, and S. Charpak, "Encoded multisite two-photon microscopy," Proc. Natl. Acad. Sci. U. S. A. **110**, 13138–13143 (2013).

44. P. J. Verveer, Q. S. Hanley, P. W. Verbeek, L. J. Van Vliet, and T. M. Jovin, "Theory of confocal fluorescence imaging in the programmable array microscope (PAM)," J. Microsc. **189**, 192–198 (1998).

45. Q. S. Hanley, P. J. Verveer, M. J. Gemkow, D. Arndt-Jovin, and T. M. Jovin, "An optical sectioning programmable array microscope implemented with a digital micromirror device," J. Microsc. **196**, 317–331 (1999).

46. A. Egner, V. Andresen, and S. W. Hell, "Comparison of the axial resolution of practical Nipkow-disk confocal fluorescence microscopy with that of multifocal multiphoton microscopy: Theory and experiment," J. Microsc. **206**, 24–32 (2002).

47. T. Tanaami, S. Otsuki, N. Tomosada, Y. Kosugi, M. Shimizu, and H. Ishida, "High-speed 1-frame/ms scanning confocal microscope with a microlens and Nipkow disks," Appl. Opt. **41**, 4704–4708 (2002).

48. C. B. Müller and J. Enderlein, "Image scanning microscopy," Phys. Rev. Lett. **104**, 198101–198104 (2010).

49. M. Kühnemund, Q. Wei, E. Darai, Y. Wang, I. Hernández-Neuta, Z. Yang, D. Tseng, A. Ahlford, et al., "Targeted DNA sequencing and in situ mutation analysis using mobile phone microscopy," Nat. Commun. **8**, 13913 (2017).

50. M. Levoy, R. Ng, A. Adams, M. Footer, and M. Horowitz, "Light field microscopy," in *ACM SIGGRAPH 2006 Papers on* -

SIGGRAPH '06 (2006), p. 924.

51. K. K. Chu, D. Lim, and J. Mertz, "Practical implementation of log-scale active illumination microscopy," Biomed. Opt. Express **1**, 236–245 (2010).

52. R. Horstmeyer, G. Zheng, C. Yang, R. Horstmeyer, C. Yang, G. Zheng, and C. Yang, "Wide-field, high-resolution Fourier ptychographic microscopy," Nat. Photonics **7**, 739–745 (2013).

53. L. Tian, X. Li, K. Ramchandran, and L. Waller, "Multiplexed coded illumination for Fourier Ptychography with an LED array microscope," Biomed. Opt. Express **5**, 2376–2389 (2014).

54. B. Enders, M. Dierolf, P. Cloetens, M. Stockmar, F. Pfeiffer, and P. Thibault, "Ptychography with broad-bandwidth radiation," Appl. Phys. Lett. **104**, 171104–5 (2014).

55. M. B. Wakin, J. N. Laska, M. F. Duarte, D. Baron, S. Sarvotham, D. Takhar, K. F. Kelly, and R. G. Baraniuk, "An architecture for compressive imaging," in *Proceedings - International Conference on Image Processing, ICIP* (2006), pp. 1273–1276.

56. J. H. J. H. Shapiro, "Computational ghost imaging," Phys. Rev. A - At. Mol. Opt. Phys. **78**, 61802–4 (2009).

57. S. M. Mahdi Khamoushi, Y. Nosrati, and S. H. Tavassoli, "Sinusoidal ghost imaging," Opt. Lett. **40**, 3452–3455 (2015).

58. P. Sen and S. Darabi, "Compressive dual photography," Comput. Graph. Forum **28**, 609–618 (2009).

59. Y. Wu, P. Ye, I. O. Mirza, G. R. Arce, and D. W. Prather, "Experimental demonstration of an Optical-Sectioning Compressive Sensing Microscope (CSM)," Opt. Express **18**, 24565–24578 (2010).

60. V. Studer, J. Bobin, M. Chahid, H. S. Mousavi, E. Candes, and M. Dahan, "Compressive fluorescence microscopy for biological and hyperspectral imaging," Proc. Natl. Acad. Sci. U. S. A. **109**, E1679–E167987 (2012).

61. V. Durán, P. Clemente, M. Fernández-Alonso, E. Tajahuerce, and J. Lancis, "Single-pixel polarimetric imaging," Opt. Lett. **37**, 824–826 (2012).

62. P. Ryczkowski, M. Barbier, A. T. Friberg, J. M. Dudley, and G. Genty, "Ghost imaging in the time domain," Nat. Photonics **10**, 167–170 (2016).

63. A. Kirmani, A. Colaço, F. N. C. Wong, and V. K. Goyal, "Exploiting sparsity in time-of-flight range acquisition using a single time-resolved sensor," Opt. Express **19**, 21485 (2011).

64. M.-J. Sun, M. P. Edgar, G. M. Gibson, B. Sun, N. Radwell, R. Lamb, and M. J. Padgett, "Single-pixel three-dimensional imaging with time-based depth resolution," Nat. Commun. **7**, 12010 (2016).

65. B. Javidi, A. Carnicer, M. Yamaguchi, T. Nomura, E. Pérez-cabré, S. María, M. S. Millán, N. K. Nishchal, et al., "Roadmap on optical security," J. Opt. **18**, 1–39 (2016).

66. B. Sun, M. P. Edgar, R. Bowman, L. E. Vittert, S. Welsh, A. Bowman, and M. J. Padgett, "3D computational imaging with single-pixel detectors," Science. **340**, 844–847 (2013).

67. E. Salvador-Balaguer, P. Clemente, E. Tajahuerce, F. Pla, and J. Lancis, "Full-Color Stereoscopic Imaging with a Single-Pixel Photodetector," J. Disp. Technol. **12**, 417–422 (2016).

68. B. Lochocki, A. Gambín, S. Manzanera, E. Irles, E. Tajahuerce, J. Lancis, and P. Artal, "Single pixel camera ophthalmoscope," Optica **3**, 1056–1059 (2016).

69. N. Radwell, K. J. Mitchell, G. GIbson, M. Edgar, R. Bowman, and M. J. Padgett, "Single-pixel infrared and visible microscope," Optica **1**, 285–289 (2014).

70. Q. Guo, H. Chen, Y. Wang, Y. Guo, P. Liu, X. Zhu, Z. Cheng, Z. Yu, et al., "High-Speed Compressive Microscopy of Flowing Cells Using Sinusoidal Illumination Patterns," IEEE Photonics J. **9**, 1–11 (2017).

71. C. M. Watts, D. Shrekenhamer, J. Montoya, G. Lipworth, J. Hunt, T. Sleasman, S. Krishna, D. R. Smith, et al., "Terahertz compressive imaging with metamaterial spatial light modulators," Nat. Photon. **8**, 605–609 (2014).

72. J. Greenberg, K. Krishnamurthy, and D. Brady, "Compressive single-pixel snapshot x-ray diffraction imaging," Opt. Lett. **39**, 111–114 (2013).

73. K. K. Tsia, K. Goda, D. Capewell, and B. Jalali, "Performance of serial time-encoded amplified microscope," Opt. Express **18**, 10016–10028 (2010).

74. O. Katz, P. Heidmann, M. Fink, and S. Gigan, "Non-invasive single-shot imaging through scattering layers and around corners via

speckle correlations," Nat. Photonics **8**, 784–790 (2014).

75. D. L. Donoho, "Compressed sensing," IEEE Trans. Inf. Theory **52**, 1289–1306 (2006).

76. E. J. Candes and M. B. Wakin, "An Introduction To Compressive Sampling," IEEE Signal Process. Mag. **25**, 21–30 (2008).

77. J. Haupt, R. Nowak, and R. Castro, "Adaptive sensing for sparse signal recovery," in *2009 IEEE 13th Digital Signal Processing Workshop and 5th IEEE Signal Processing Education Workshop, DSP/SPE 2009, Proceedings* (2009), pp. 702–707.

78. F. Soldevila, E. Salvador-Balaguer, P. Clemente, E. Tajahuerce, and J. Lancis, "High-resolution adaptive imaging with a single photodiode," Sci. Rep. **5**, 14300 (2015).

79. D. B. Phillips, M.-J. Sun, J. M. Taylor, M. P. Edgar, S. M. Barnett, G. M. Gibson, and M. J. Padgett, "Adaptive foveated single-pixel imaging with dynamic supersampling," Sci. Adv. **3**, e1601782 (2017).

80. E. J. Candès, J. Romberg, and T. Tao, "Robust uncertainty principles: Exact signal reconstruction from highly incomplete frequency information," IEEE Trans. Inf. Theory **52**, 489–509 (2006).

81. E. J. Candes and T. Tao, "Near-optimal signal recovery from random projections: Universal encoding strategies?," IEEE Trans. Inf. Theory **52**, 5406–5425 (2006).

82. M. Castello, C. J. R. Sheppard, A. Diaspro, and G. Vicidomini, "Image scanning microscopy with a quadrant detector," Opt. Lett. **40**, 5355–5358 (2015).

83. M. F. Duarte, M. a Davenport, D. Takhar, J. N. Laska, K. F. Kelly, R. G. Baraniuk, and J. Romberg, "Single-Pixel Imaging via Compressive Sampling," IEEE Signal Process. Mag. **25**, 14–20 (2008).

84. P. Taroni, G. Valentini, D. Comelli, C. D'Andrea, R. Cubeddu, D.-N. Hu, and J. E. Roberts, "Time-resolved microspectrofluorimetry and fluorescence lifetime imaging of hypericin in human retinal pigment epithelial cells.," Photochem. Photobiol. **81**, 524–528 (2005).

85. H. Chen, Z. Weng, Y. Liang, C. Lei, F. Xing, M. Chen, and S. Xie, "High speed single-pixel imaging via time domain compressive

sampling," Cleo 2014 JTh2A.132 (2014).

86. W. K. Yu, X. R. Yao, X. F. Liu, R. M. Lan, L. A. Wu, G. J. Zhai, and Q. Zhao, "Compressive microscopic imaging with “positive-negative” light modulation," Opt. Commun. **371**, 105–111 (2016).

87. N. Pavillon and N. I. Smith, "Compressed sensing laser scanning microscopy," Opt. Express **24**, 4982–4990 (2016).

88. B. T. Bosworth, J. R. Stroud, D. N. Tran, T. D. Tran, S. Chin, and M. A. Foster, "High-speed flow microscopy using compressed sensing with ultrafast laser pulses," Opt. Express **23**, 10521–10532 (2015).

89. J. Shin, B. T. Bosworth, and M. A. Foster, "Compressive fluorescence imaging using a multi-core fiber and spatially dependent scattering," Opt. Lett. **42**, 109–112 (2017).

90. Q. Guo, H. Chen, Z. Weng, M. Chen, S. Yang, and S. Xie, "Compressive sensing based high-speed time-stretch optical microscopy for two-dimensional image acquisition," Opt. Express **23**, 29639–29646 (2015).

91. W. Denk, J. H. Strickler, and W. W. Webb, "Two-photon laser scanning fluorescence microscopy," Science **248**, 73–76 (1990).

92. D. J. Brady, *Optical Imaging and Spectroscopy* (John Wiley & Sons, 2009).

93. P. X. Clemente, *Sistemes Formadors D ’imatges Multidimensionals Amb Detecció Integrada* (Universitat Jaume I, 2015).

94. J. Hunt, T. Driscoll, A. Mrozack, G. Lipworth, M. Reynolds, D. Brady, and D. R. Smith, "Metamaterial Apertures for Computational Imaging," Science. **339**, 310–313 (2013).

95. E. Martín-Badosa, M. Montes-Usategui, A. Carnicer, J. Andilla, E. Pleguezuelos, and I. Juvells, "Design strategies for optimizing holographic optical tweezers set-ups," J. Opt. A Pure Appl. Opt. **9**, S267–S277 (2007).

96. I. Moreno, J. a Davis, B. M. Pascoguin, M. J. Mitry, and D. M. Cottrell, "Vortex sensing diffraction gratings," Opt. Lett. **34**, 2927–2929 (2009).

97. M. S. Millán, E. Pérez-Cabré, L. A. Romero, and N. Ramírez, "Programmable diffractive lens for ophthalmic application," Opt. Eng. **53**, 61709–12 (2014).

98. M. Kreysing, D. Ott, M. J. Schmidberger, O. Otto, M. Schürmann, E. Martín-Badosa, G. Whyte, and J. Guck, "Dynamic operation of optical fibres beyond the single-mode regime facilitates the orientation of biological cells," Nat. Commun. **5**, 5481 (2014).

99. M. Takeda, W. Wang, and D. N. Naik, "Coherence Holography: A Thought on Synthesis and Analysis of Optical Coherence Fields," in *Fringe 2009* (Springer Berlin Heidelberg, 2009), pp. 1–8.

100. E. Frumker and Y. Silberberg, "Phase and amplitude pulse shaping with two-dimensional phase-only spatial light modulators," J. Opt. Soc. Am. B **24**, 2940–2947 (2007).

101. E. Frumker and Y. Silberberg, "Femtosecond pulse shaping using a two-dimensional liquid-crystal spatial light modulator," Opt. Lett. **32**, 1384–1386 (2007).

102. H. Chen, Z. Zheng, B.-F. Zhang, J. Ding, and H.-T. Wang, "Polarization structuring of focused field through polarization-only modulation of incident beam," Opt. Lett. **35**, 2825–2827 (2010).

103. F. Kenny, D. Lara, O. G. Rodríguez-Herrera, and C. Dainty, "Complete polarization and phase control for focus-shaping in high-NA microscopy," Opt. Express **20**, 14015–14029 (2012).

104. A. P. Mosk, "Imaging and focusing through turbid media," in *Bio-Optics: Design and Application, BODA 2013* (2013).

105. P. Clemente, V. Durán, L. Martínez-León, V. Climent, E. Tajahuerce, and J. Lancis, "Use of polar decomposition of Mueller matrices for optimizing the phase response of a liquid-crystal-on-silicon display," Opt. Express **16**, 1965–1974 (2008).

106. T. Fukano and A. Miyawaki, "Whole-field fluorescence microscope with digital micromirror device: imaging of biological samples," Appl. Opt. **42**, 4119–4124 (2003).

107. D. Xu, T. Jiang, A. Li, B. Hu, Z. Feng, H. Gong, S. Zeng, and Q. Luo, "Fast optical sectioning obtained by structured illumination microscopy using a digital mirror device," J. Biomed. Opt. **18**, 60503 (2013).

108. F. P. Martial and N. A. Hartell, "Programmable illumination and high-speed, multi-wavelength, confocal microscopy using a digital micromirror," PLoS One **7**, e43942 (2012).

109. E. Papagiakoumou, "Optical developments for optogenetics," Biol. Cell **105**, 443–464 (2013).

110. J. C. H. Gregory A. Howland, Daniel J. Lum, Matthew R. Ware, "Photon counting compressive depth mapping," Opt. Express **21**, 23822–23837 (2013).

111. B. M. Davis, A. J. Hemphill, D. C. Maltaş, M. a Zipper, P. Wang, and D. Ben-Amotz, "Multivariate hyperspectral Raman imaging using compressive detection," Anal. Chem. **83**, 5086–92 (2011).

112. *Photomultiplier Handbook* (Burle Industries, Inc., 1980).

113. H. Iams and B. Salzberg, "The Secondary Emission Phototube," Proc. Inst. Radio Eng. **23**, 55–64 (1935).

114. V. K. Zworykin, G. A. Morton, and L. Malter, "The Secondary Emission Multiplier-A New Electronic Device," Proc. IRE **24**, 351–375 (1936).

115. V. K. Zworykin and J. a. Rajchman, "The Electrostatic Electron Multiplier," Proc. IRE **27**, 558–566 (1939).

116. C. Zavaleta, "Photodiodes as Substitutes for Photomultiplier Tubes," (2003).

117. F. Soldevila, P. Clemente, E. Tajahuerce, P. Andrés, and J. Lancis, "Computational imaging with a balanced detector," Nat. Publ. Gr. 1–10 (2016).

118. B. Lochocki, A. Gambín, and P. Artal, "Performance evaluation of a two detector camera for real-time video," **55**, 10198–10203 (2016).

119. J. N. Laska, S. Kirolos, M. F. Duarte, T. S. Ragheb, R. G. Baraniuk, and Y. Massoud, "Theory and Implementation of an Analog-to-Information Converter using Random Demodulation," 2007 IEEE Int. Symp. Circuits Syst. 1959–1962 (2007).

120. M. Mishali and Y. C. Eldar, "Blind multiband signal reconstruction: Compressed sensing for analog signals," IEEE Trans. Signal Process. **57**, 993–1009 (2009).

121. W. Dai, M. a Sheikh, O. Milenkovic, and R. G. Baraniuk, "Compressive sensing DNA microarrays," EURASIP J. Bioinform. Syst. Biol. 162824 (2009).

122. M. Pourhomayoun, M. Fowler, and Z. Jin, "A novel method for medical implant in-body localization," in *Proceedings of the Annual International Conference of the IEEE Engineering in Medicine and Biology Society, EMBS* (2012), pp. 5757–5760.

123. F. J. Herrmann and G. Hennenfent, "Non-parametric seismic data recovery with curvelet frames," Geophys. J. Int. **173**, 233–248 (2008).

124. T. T. Y. Lin and F. J. Herrmann, "Compressed wavefield extrapolation," Geophysics **72**, SM77 (2007).

125. R. Baraniuk and P. Steeghs, "Compressive radar imaging," in *IEEE National Radar Conference - Proceedings* (2007), pp. 128–133.

126. L. C. Potter, E. Ertin, J. T. Parker, and M. ??etin, "Sparsity and compressed sensing in radar imaging," Proc. IEEE **98**, 1006–1020 (2010).

127. J. Bobin, J. L. Starck, and R. Ottensamer, "Compressed sensing in astronomy," IEEE J. Sel. Top. Signal Process. **2**, 718–726 (2008).

128. Y. Wiaux, L. Jacques, G. Puy, A. M. M. Scaife, and P. Vandergheynst, "Compressed sensing imaging techniques for radio interferometry," Mon. Not. R. Astron. Soc. **395**, 1733–1742 (2009).

129. W. U. Bajwa, J. Haupt, A. M. Sayeed, and R. Nowak, "Compressed channel sensing: A new approach to estimating sparse multipath channels," Proc. IEEE **98**, 1058–1076 (2010).

130. P. Zhang, Z. Hu, R. C. Qiu, and B. M. Sadler, "A compressed sensing based ultra-wideband communication system," in *IEEE International Conference on Communications* (2009).

131. J. Ma, "Compressed sensing for surface characterization and metrology," IEEE Trans. Instrum. Meas. **59**, 1600–1615 (2010).

132. J. Ma and F. X. Le Dimet, "Deblurring from highly incomplete measurements for remote sensing," IEEE Trans. Geosci. Remote Sens. **47**, 792–802 (2009).

133. X. X. Zhu and R. Bamler, "Super-resolution power and robustness of compressive sensing for spectral estimation with application to spaceborne tomographic SAR," IEEE Trans. Geosci. Remote Sens. **50**, 247–258 (2012).

134. D. Shamsi, P. Boufounos, and F. Koushanfar, "Noninvasive leakage power tomography of integrated circuits by compressive sensing," in *Proceeding of the Thirteenth International Symposium on Low Power Electronics and Design - ISLPED '08* (2008), p. 341.

135. M. Nagahara, T. Matsuda, and K. Hayashi, "Compressive Sampling for Remote Control Systems," IEICE Trans. Fundam. Electron. Commun. Comput. Sci. **E95**–**A**, 713–722 (2013).

136. T. Hu and D. B. Chklovskii, "Reconstruction of sparse circuits using multi-neuronal excitation (RESCUME)," Front. Neurosci. **4**, 1–9 (2010).

137. D. Gross, Y. K. Liu, S. T. Flammia, S. Becker, and J. Eisert, "Quantum state tomography via compressed sensing," Phys. Rev. Lett. **105**, 150401–4 (2010).

138. X. Andrade, J. N. Sanders, and A. Aspuru-Guzik, "Application of compressed sensing to the simulation of atomic systems," Proc. Natl. Acad. Sci. **109**, 13928–13933 (2012).

139. M. Lustig, D. Donoho, and J. M. Pauly, "Sparse MRI: The application of compressed sensing for rapid MR imaging," Magn. Reson. Med. **58**, 1182–1195 (2007).

140. J. Provost and F. Lesage, "The application of compressed sensing for photo-acoustic tomography," IEEE Trans. Med. Imaging **28**, 585–594 (2009).

141. E. J. Candès, J. K. Romberg, and T. Tao, "Stable signal recovery from incomplete and inaccurate measurements," Commun. Pure Appl. Math. **59**, 1207–1223 (2006).

142. E. Candès and J. Romberg, "Sparsity and incoherence in compressive sampling," Inverse Probl. **23**, 969–985 (2007).

143. R. G. Baraniuk, "Compressive sensing," IEEE Signal Process. Mag. **24**, 118–124 (2007).

144. J. M. Lustig, Michael and Donoho, David L and Santos, Juan M and Pauly, "Compressed sensing MRI," Signal Process. Mag. IEEE **25**, 72–82 (2008).

145. J.-E. Oh, Y.-W. Cho, G. Scarcelli, and Y.-H. Kim, "Sub-Rayleigh imaging via speckle illumination," Opt. Lett. **38**, 682–684 (2013).

146. W. Gong, Z. Bo, E. Li, and S. Han, "Experimental investigation of the quality of ghost imaging via sparsity constraints," Appl. Opt. **52**, 3510–3515 (2013).

147. Z. Zalevsky and D. Mendlovic, *Optical Superresolution*, Springer Series in Optical Sciences (Springer New York, 2004), Vol. 91.

148. Y. Choi, T. D. Yang, C. Fang-Yen, P. Kang, K. J. Lee, R. R. Dasari, M. S. Feld, and W. Choi, "Overcoming the diffraction limit using multiple light scattering in a highly disordered medium," Phys. Rev. Lett. **107**, 23902 (2011).

149. M. Lee, O. Yaglidere, and A. Ozcan, "Field-portable reflection and transmission microscopy based on lensless holography," Biomed. Opt. Express **2**, 2721–2730 (2011).

150. N. A. Talaikova, A. L. Kalyanov, and V. P. Ryabukho, "Diffraction phase microscopy with transmission and reflection illumination for refractive index measurements," Proc. SPIE **9529**, 95291D (2015).

151. P.-K. Wei, C.-C. Wei, J.-H. Hsu, and W.-S. Fann, "Simultaneous reflection and transmission modes near-field scanning optical microscope," Ultramicroscopy **61**, 237–239 (1995).

152. J. M. Rodenburg and H. M. L. Faulkner, "A phase retrieval algorithm for shifting illumination," Appl. Phys. Lett. **85**, 4795–4797 (2004).

153. J. M. Rodenburg, "Ptychography and related diffractive imaging methods," Adv. Imaging Electron Phys. **150**, 87–184 (2008).

154. P. D. Nellist, B. C. McCallum, and J. M. Rodenburg, "Resolution beyond the "information limit" in transmission electron microscopy," Nature **374**, 630–632 (1995).

155. J. M. Rodenburg, A. C. Hurst, and A. G. Cullis, "Transmission microscopy without lenses for objects of unlimited size," Ultramicroscopy **107**, 227–231 (2006).

156. F. Hüe, J. M. Rodenburg, A. M. Maiden, F. Sweeney, and P. A. Midgley, "Wave-front phase retrieval in transmission electron microscopy via ptychography," Phys. Rev. B - Condens. Matter Mater. Phys. **82**, 121415–4 (2010).

157. X. Ou, R. Horstmeyer, C. Yang, and G. Zheng, "Quantitative phase imaging via Fourier ptychographic microscopy," Opt. Lett. **38**, 4845–4848 (2013).

158. L. Tian and L. Waller, "3D intensity and phase imaging from light field measurements in an LED array microscope," Optica **2**, 104–111 (2015).

159. E. Mudry, K. Belkebir, J. Girard, J. Savatier, E. Le Moal, C. Nicoletti, M. Allain, and a. Sentenac, "Structured illumination microscopy using unknown speckle patterns," Nat. Photonics **6**, 312–315 (2012).

160. M. Harwit and N. J. Sloane, *Hadamard Transform Optics* (Acad. Press, 1979).

161. W. K. Pratt, J. Kane, and H. C. Andrews, "Hadamard transform

image coding," Proc. IEEE **57**, 58–68 (1969).

Publications

[I]

Resolution analysis in computational imaging with patterned illumination and bucket detection.

Optics Letters, Optics Letters, 39, 3888-91. 2014

Resolution analysis in computational imaging with patterned illumination and bucket detection

A. D. Rodríguez,[1,*] P. Clemente,[2] E. Irles,[1] E. Tajahuerce,[1] and J. Lancis[1]

[1]*Institut de Noves Tecnologies de la Imatge (INIT), Universitat Jaume I, Castelló 12071, Spain*

[2]*Servei Central d'Instrumentació Científica (SCIC), Universitat Jaume I, Castelló 12071, Spain*

**Corresponding author: jimeneza@uji.es*

Received April 1, 2014; revised May 8, 2014; accepted May 21, 2014;
posted May 23, 2014 (Doc. ID 209268); published June 24, 2014

In computational imaging by pattern projection, a sequence of microstructured light patterns codified onto a programmable spatial light modulator is used to sample an object. The patterns are used as generalized measurement modes where the object information is expressed. In this Letter, we show that the resolution of the recovered image is only limited by the numerical aperture of the projecting optics regardless of the quality of the collection optics. We provide proof-of-principle experiments where the single-pixel detection strategy outperforms the resolution achieved using a conventional optical array detector for optical imaging. It is advantageous in the presence of real-world conditions, such as optical aberrations and optical imperfections in between the sample and the sensor. We provide experimental verification of image retrieval even when an optical diffuser prevents imaging with a megapixel array camera.

OCIS codes: (110.0180) Microscopy; (110.1758) Computational imaging; (220.1000) Aberration compensation; (350.5730) Resolution.

http://dx.doi.org/10.1364/OL.39.003888

Despite ongoing improvements in optical array detector technologies such as charge-coupled devices (CCDs) and electron multiplying charge-coupled devices (EMCCDs) cameras, both point and line scanning methods provide the method of choice in several imaging devices as, for instance, in confocal or multiphoton microscopy. In the former, dot-by-dot illumination of the scene with a femtosecond laser pulse triggers spatially resolved multiphoton absorption, which is the key for optical sectioning. Single-pixel detection allows us to achieve low-light sensitivity as well as multidimensional capability through the use of specialized sensing.

Although systems that scan a single-element benefit from mature technology, they suffer from acquisition times linearly proportional to the spatial resolution. Significant per-pixel dwell times limit real-time performance to low resolution. A promising option is to use global illumination strategies while preserving a single-pixel "bucket" detector. To do this, the sample is obtained by imaging the scene through microstructured masks implemented onto a programmable spatial light modulator (SLM). In this approach, a single-pixel detector measures the transmitted or reflected power as the pattern generated in the SLM changes in a sequential manner. The programmed patterns are used as generalized measurement modes where the object information is expressed and the sample is recovered through algebraic optimization. This principle enables retrieval of the spatial information of an object in ghost [1,2] and compressive imaging [3]. Among the applications that benefit from the potential advantages of the so-called "single-pixel cameras" are fluorescence microscopy [4], hyperspectral imaging [5], and polarimetric imaging [6], to list only a few.

The fundamental reason why the bucket detection strategy can outperform conventional optical array detection is the use of a single channel detector that simultaneously integrates all the photons transmitted through the patterned scene. As a matter of fact, incoherent measurements used in imaging with patterned illumination use half the available light on average so that they match low-light level conditions. This requires large linear dynamic range photodetectors. However, this approach has been demonstrated to work at sub-picowatt light levels by using photomultiplier tubes and Geiger-mode avalanche photodiodes that provide shot-noise limited detection [7]. This type of sensor is difficult to integrate in an arrayed detector.

On the other hand, a main difference between the serial scanning and global illumination approaches is related to temporal resolution. While serial excitation is mainly limited by the dwell time at a given position, that is, the time to induce a detectable response, global illumination schemes demand a short refreshing rate for the SLM, which can be of the order of tens of kilohertz if a digital micromirror device (DMD) is used as an SLM. The multiplex advantage in single-pixel cameras has been successfully employed to acquire the collection of chemical images in less than 1 min in multivariate hyperspectral Raman imaging [8]. This represents a speed advantage of the order of 100.

Single-pixel cameras also benefit from the compressive detection strategy [9]. Most images of interest that are obtained in experiments or by numerical computation of natural phenomena are sparse. In compressive sampling (CS), it is possible to make use of this fact to recover an image from fewer measurements than those expected by the Nyquist sampling rate, often less than 10%. The approach is so named because it allows image compression to be performed during measurement rather than in the post-processing stage.

In this Letter, we focus on the analysis of resolution in optical imaging with patterned illumination and bucket detection. The reasons for our research are twofold. On the one hand, speckle illumination and second-order correlation measurement have shown to provide sub-Rayleigh limit imaging [10,11]. Imaging with patterned illumination and bucket detection is closely related to

the above technique in the sense that the information in incoherent measurements used for compressive sensing is contained in their deviation from the mean. Also, despite the commonly held opinion that algorithmic methods for subwavelength imaging are impractical, sparsity-based subwavelength imaging has demonstrated recovery of 100 nm features in a sample illuminated with light of wavelength of 532 nm [12]. This superresolution feature works for both coherent and incoherent light. In the same direction, virtually structured detection through mathematical processing of digital images has been proposed as the dual technique of structured illumination microscopy technique [13]. On the other hand, ghost imaging has been claimed as an alternative to carry out image transmission through an aberrating medium [14]. In the same context, the possibility for image transmission through highly scattering medium is of a high practical interest [15].

Our Letter makes two specific contributions within the field of single-pixel imaging through patterned illumination. First, we perform an analysis of the optical resolution of the computational image. This resolution is shown not to be limited at all by the optical quality of the collection optics. This result is proved by using a low NA microscope objective for imaging at a CCD camera. Spatial frequencies that are not transmitted through this low quality optics are demonstrated to be present in the retrieved image through patterned illumination. Second, we experimentally demonstrate the capability of our technique to properly recover an image even when an optical diffuser is located in between the sample and the bucket detector.

As mentioned above, most images of interest are sparse in some particular basis functions. Let us suppose that an N-pixel image has only S nonzero significant coefficients in a given basis. CS states that an M-random subset of coefficients of the image expressed in this basis contains enough information for image reconstruction with high accuracy [3,9]. The CS technique asserts the image can be retrieved if $M \geq S \log N$, overcoming the Nyquist sample rate and achieving a compression ratio $\mathrm{CR} = N/M$. In our experiment, a single-pixel detection system is implemented in order to measure these M coefficients by projecting the object onto the random subset of functions in an iterative acquisition process. The selection of these coefficients of the unknown image can be expressed as

$$\mathbf{y} = \mathbf{S}\mathbf{x}, \tag{1}$$

where $\mathbf{x}$ is the N-pixel unknown image expressed in the chosen basis, $\mathbf{y}$ is the subset of M-coefficients measured by projection process and $\mathbf{S}$ is the sensing matrix. The underdetermined matrix relation obtained after the measurement process has an infinite number of solutions. Assuming the sparsity of the solution, CS allows us to find a unique one. In our case, the approach to solve the problem is based on the minimization of the l_1-norm of $\mathbf{x}$ subjected to the constraint given by Eq. (1), that is

$$\min \|\mathbf{x}\|_{l_1} \quad \text{such that} \quad \mathbf{y} = \mathbf{S}\mathbf{x}, \tag{2}$$

where $\|\mathbf{x}\|_{l_1} = \sum_i |x_i|$. A suitable algorithm is used to find the minimum that leads to the solution, namely, the retrieved image. In our experiments, Walsh–Hadamard functions are chosen as the projection basis and the *l1eq-pd* programming code is employed in the off-line reconstruction [16].

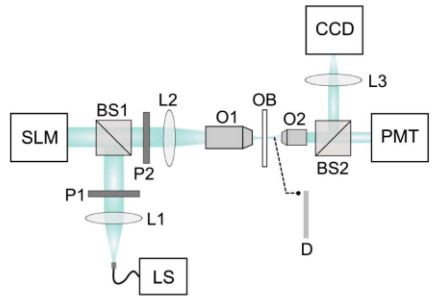

Fig. 1. Experimental setup for image resolution analysis via Hadamard illumination using a single-pixel architecture. See text for details.

A Walsh–Hadamard matrix of order n is a binary $n \times n$ matrix with ± 1 entries that satisfies $H_n^T H_n = n I_n$, where I_n is the identity matrix and H_n^T denotes transposed matrix. Walsh–Hadamard matrices form an orthonormal basis with an optimum weighting design for extracting information from random noise.

The single-pixel detection system used to analyze the resolution limit is shown in Fig. 1. The optical setup can be divided into two parts: the illumination system and the collection system, located left and right of the object OB, respectively. In the illumination system, the SLM generates binary patterns modulated on amplitude sequentially. These patterns are reduced and projected onto the object through an optical lens and a microscope objective. In the collection system, a microscope objective with low NA collects the light transmitted by the object for each pattern. A photomultiplier tube (PMT) integrates the light provided by the objective and returns the value of the coefficient associated to each pattern. Finally, the image is reconstructed by applying the optimization algorithm in Eq. (2) to this set of coefficients. To compare the optical resolution of our single-pixel system with that of a conventional one, a CCD captures a conventional image of the object by using the same low NA objective. The details of the optical elements in Fig. 1 are the following. The light source (LS) is a mercury lamp (Nikon, Intensilight C-HGFI). In order to achieve quasi-monochromatic signal, the light is filtered with a color filter (part of Pasco AP-9368). After passing through a collimator lens (L1), the light illuminates the SLM (a reflective liquid crystal on silicon display, Holoeye LC-R 2500) with XGA resolution and a pixel pitch of 19 μm. A beam splitter (BS1) allows this SLM to work at normal incidence. Both SLM and BS1 were sandwiched between crossed polarizers (P1 and P2) to get amplitude modulation. The light patterns are projected onto the object by the objective O1 (Nikon LU Plan 20X/0.40 WD 13). The outgoing light is collected with the microscope objective O2 (Nikon E Plan 4X/0.10 WD 30). A second beam splitter (BS2) permits us to both observe the light projection by a CCD (Basler A102fc, pixel size = 6.45 μm × 6.45 μm) and capture the intensity using a PMT (PMM01, Thorlabs

Inc.). With the aim of analyzing the optical resolution in both the conventional and the single-pixel system, a USAF test chart (OB, USAF 1951 2″ × 2″, Edmund Optics) is employed as the object.

The resolution of the illumination system is limited by diffraction by the aperture of O1 to 0.8 μm, while the resolution is limited geometrically by the pixel size of the SLM in the sample plane after the reduction produced by L2 and O1 to 1.68 μm. As the recording system is based on detecting fluctuations of the integrated intensity, instead of resolving the spatial information, the collecting system has no influence on the resolution. In this sense, the system resembles to some extent Type I scanning optical microscopes but with wide-field illumination [17]. Note that O2 is only necessary to form the image on the CCD. Indeed if O2 were removed and the PMT placed directly behind the sample, the imaging resolution would remain the same.

The experimental results are shown in Fig. 2. Figure 2(a) shows the portion of the USAF test imaged by our optical system. Only the smallest groups of the test, 6 and 7, are used to bound the resolution of the systems. The optical system is designed in such a way that the resolution is not restricted geometrically by the size of the pixels of the CCD. Therefore, in principle, the theoretical resolution of the conventional system is limited by diffraction to $\delta x = 0.61\lambda/\mathrm{NA} = 3.33$ μm because of the low NA objective O2. In fact, as shown in Fig. 2(b), the conventional image provided by the CCD allows us to distinguish up to the element 6-5 of the USAF test, corresponding to a resolution of 4.9 μm. This is also shown in blue profiles in Figs. 2(d) and 2(e) that correspond to elements 6-6 and 7-5. However, as can be seen in Fig. 2(c), the resolution shown by our single-pixel configuration allows us to distinguish the element 7-5 of the USAF test, corresponding to a resolution limit of 2.46 μm. This fact is clearly noticeable in the red plots in Figs. 2(d) and 2(e), which allow us to discriminate the lines in the elements 6-6 and 7-5 of the test. Therefore, the improvement of resolution with our single-pixel system is almost two times better than that provided by the conventional system. In Fig. 2(b) and more clearly in Fig. 2(c), a non-symmetry can also be observed between horizontal and vertical lines (CCD and single-pixel imaging respectively). This might be due to cylindrical aberration induced by the SLM. This aberration can be corrected but this is beyond the purpose of this work. These results show that the image obtained by computational imaging contains frequencies of the object that are above the frequency limit associated with the low-quality objective lens for conventional imaging. In other words, our single-pixel system is able to provide images with a resolution below the Rayleigh criterion. This is due to the spread of the spatial spectrum of the object produced by the projection of the high-frequency Hadamard patterns. The effect is similar to that produced by structured illumination in superresolution approaches based on spatial-frequency multiplexing [18].

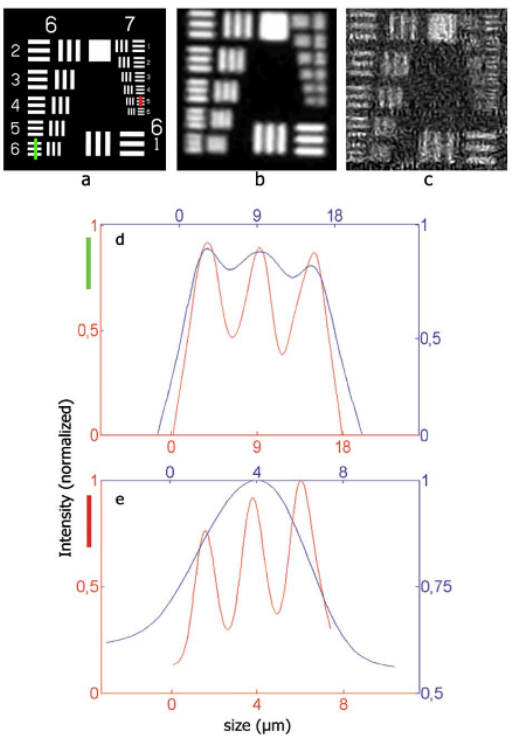

Fig. 2. Experimental results for image resolution analysis. (a) Part of the USAF test image. (b) Image obtained with CCD camera. (c) Reconstructed image of 128 × 128 pixels via single-pixel imaging (CR = 2). Panels (d) and (e) show intensity profiles for USAF elements 6-6 and 7-5, respectively. Blue lines correspond to the CCD camera and red lines to the single-pixel image. The curves have been smoothed.

To emphasize the fact that the resolution of the system does not depend on the collection system and is tolerant to some optical aberrations, next we prove that the system is able to recover images even when a diffuser distorts the light diffracted by the object. Figure 3(a) shows the image of the USAF test provided by the conventional imaging system when a commercial diffuser (D, Edmund Optics T54-497) is placed between the sample and the collection system. Note that the image is completely blurred by the action of the diffuser. Interestingly, the computational imaging approach based on single-pixel detection is able to reconstruct the image as can be seen in Fig. 3(b). In fact, the presence of the diffuser in the optical system in Fig. 1 can be advantageous because it improves the average ratio between low and high frequencies [19]. The combined action of the high-frequency patterns projected onto the object and the frequency mixture provided by the diffuser allow us to

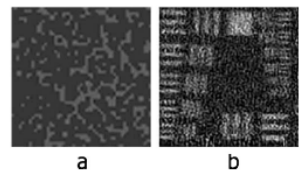

Fig. 3. Images taken through a commercial diffuser placed between OB and O2 (see Fig. 1). (a) Image obtained with CCD camera. (b) Reconstructed image via single-pixel imaging (CR = 2).

record frequencies of the object not resolved by conventional imaging systems.

The total time required to take image data increases with the number of measurements. The exact number M of measurements that allows to provide an accurate reconstruction of an object from an undersampled signal is not *a priori* known. In addition, this number strongly depends on the features of the object under consideration. For this reason, we tested the quality of the recovered images evaluating the standard peak signal-to-noise ratio (*PSNR*) and the acquisition time for different values of M. When $M = 8192$ (CR = 2), it exists as a trade-off between image quality and acquisition time because the time required for the sensing stage could be reduced by a factor of 2 while the *PSNR* is still higher than 20 dB, which indicates high image fidelity. In our experimental setup, the PMT can detect light signals at frequencies as high as 20 kHz. However, the acquisition frequency is limited to 60 Hz by the frame rate of the liquid crystal SLM. Furthermore, this kind of SLM provides amplitude values with slight temporal fluctuations, which are causing the noise in our experimental results in Figs. 2(c) and 3(b). These points can be easily improved by using DMD modulators, which can operate at much higher rates [7] and with better stability.

In conclusion, we have demonstrated that single-pixel imaging improves resolution of conventional imaging systems overcoming the Rayleigh criterion. This is due to the use of high-frequency Hadamard patterns in the projection system but also to the blindness of the collection system to optical aberrations. This blindness goes so far that we are able to reconstruct an image even when the light has been transmitted through a diffusing medium. The use of a PMT also allows imaging with very low light levels (a common situation in fluorescence microscopy) and produces an increase in signal-to-noise ratio due to the gain of this type of sensor. However, single-pixel imaging is not free from drawbacks, like the increase in acquisition time, limited in our case by the SLM sample rate.

This work was supported by the Generalitat Valenciana through projects PROMETEO/2012/021, ISIC/2012/013, and by the Universitat Jaume I through project P1-1B2012-55. A. D. Rodríguez acknowledges grant PREDOC/2012/41 from Universitat Jaume I.

References

1. J. H. Shapiro, Phys. Rev. A **78**, 061802 (2008).
2. B. I. Erkmen and J. H. Shapiro, Adv. Opt. Photon. **2**, 405 (2010).
3. M. F. Duarte, M. A. Davenport, D. Takhar, J. N. Laska, K. F. Kelly, and R. G. Baraniuk, IEEE Signal Process. Mag. **25**(2), 83 (2008).
4. V. Studer, J. Bobin, M. Chahid, H. S. Mousavi, E. Candes, and M. Dahan, Proc. Natl. Acad. Sci. USA **109**, E1679 (2012).
5. F. Soldevila, E. Irles, V. Durán, P. Clemente, M. Fernández-Alonso, E. Tajahuerce, and J. Lancis, Appl. Phys. B **113**, 551 (2013).
6. V. Durán, P. Clemente, M. Fernández-Alonso, E. Tajahuerce, and J. Lancis, Opt. Lett. **37**, 824 (2012).
7. G. A. Howland, D. J. Lum, M. R. Ware, and J. C. Howell, Opt. Express **21**, 23822 (2013).
8. B. M. Davis, A. J. Hemphill, D. Cebeci Maltaş, M. A. Zipper, P. Wang, and D. Ben-Amotz, Anal. Chem. **83**, 5086 (2011).
9. E. J. Candes and M. B. Wakin, IEEE Signal Process. Mag. **25** (5), 682 (2008).
10. J.-E. Oh, Y.-W. Cho, G. Scarcelli, and Y.-H. Kim, Opt. Lett. **38**, 682 (2013).
11. W. Gong, Z. Bo, E. Li, and S. Han, Appl. Opt. **52**, 3510 (2013).
12. A. Szameit, Y. Shechtman, E. Osherovich, E. Bullkich, P. Sidorenko, H. Dana, S. Steiner, E. B. Kley, S. Gazit, T. Cohen-Hyams, S. Shoham, M. Zibulevsky, I. Yavneh, Y. C. Eldar, O. Cohen, and M. Segev, Nat. Mater. **11**, 455 (2012).
13. R.-W. Lu, B.-Q. Wang, Q.-X. Zhang, and X.-C. Yao, Biomed. Opt. Express **4**, 1673 (2013).
14. T. Shirai, H. Kellock, T. Setälä, and A. T. Friberg, J. Opt. Soc. Am. A **29**, 1288 (2012).
15. A. P. Mosk, A. Lagendijk, G. Lerosey, and M. Fink, Nat. Photonics **6**, 283 (2012).
16. E. J. Candes, http://users.ece.gatech.edu/justin/l1magic.
17. T. Wilson, *Theory and Practice of Scanning Optical Microscopy* (Academic, 1984).
18. Z. Zalevsky and D. Mendlovic, *Optical Superresolution* (Springer, 2003).
19. Y. Choi, T. D. Yang, C. Fang-Yen, P. Kang, K. J. Lee, R. R. Dasari, M. S. Feld, and W. Choi, Phys. Rev. Lett. **107**, 023902 (2011).

[II]

Dual-mode optical microscope based on single-pixel imaging.

Optics And Lasers In Engineering, 82, 87-94. 2016

Optics and Lasers in Engineering 82 (2016) 87–94

Contents lists available at ScienceDirect

Optics and Lasers in Engineering

journal homepage: www.elsevier.com/locate/optlaseng

Dual-mode optical microscope based on single-pixel imaging

A.D. Rodríguez [a,*], P. Clemente [b], E. Tajahuerce [a], J. Lancis [a]

[a] Institut de Noves Tecnologies de la Imatge (INIT), Universitat Jaume I, Castelló 12071, Spain
[b] Servei Central d'Instrumentació Científica (SCIC), Universitat Jaume I, Castelló 12071, Spain

ARTICLE INFO

Article history:
Received 13 October 2015
Received in revised form
21 January 2016
Accepted 6 February 2016

Keywords:
Microscopy
Reflection
Transmission
Resolution
Computational imaging

ABSTRACT

We demonstrate an inverted microscope that can image specimens in both reflection and transmission modes simultaneously with a single light source. The microscope utilizes a digital micromirror device (DMD) for patterned illumination altogether with two single-pixel photosensors for efficient light detection. The system, a scan-less device with no moving parts, works by sequential projection of a set of binary intensity patterns onto the sample that are codified onto a modified commercial DMD. Data to be displayed are geometrically transformed before written into a memory cell to cancel optical artifacts coming from the diamond-like shaped structure of the micromirror array. The 24-bit color depth of the display is fully exploited to increase the frame rate by a factor of 24, which makes the technique practicable for real samples. Our commercial DMD-based LED-illumination is cost effective and can be easily coupled as an add-on module for already existing inverted microscopes. The reflection and transmission information provided by our dual microscope complement each other and can be useful for imaging non-uniform samples and to prevent self-shadowing effects.

1. Introduction

Optical microscopy techniques have become essential tools in basic and applied research. For instance, in the biological realm, fluorescence microscopy is the method of choice for imaging proteins and their nano-scale dynamic organization. Despite impressive improvements in optical resolution during the last decades [1–3], there is still room to improve a range of other features such as the trade-off between the field of view and the depth of field [4,5], 3D imaging of specimens [6], or the design of cost-effective, light-weight platforms that can operate in resource-limited settings for global health challenges [7,8], among others.

Structured illumination microscopy (SIM) stands out among the different optical microscopy techniques because it allows us to retrieve spatial frequency information inaccessible with standard uniform illumination schemes [9,10]. It is based on a standard wide-field optical microscope where the specimen is illuminated with a set of known sinusoidal patterns with different phase shifts. The object is reconstructed from multiple acquisitions by using dedicated algorithms. Additionally, this fringe-projection method is attractive because of its intrinsic optical sectioning capability that enables whole-field optically sectioned images [11,12].

In the conventional implementation of a SIM, a focal plane array detector detects variations in light intensities scattered by the sample with spatial resolution. Other structured illumination approaches have also been implemented for microscopy during the past few years. The single-pixel imaging (SPI) scheme [13] has gained considerable attention as a very effective sensing mechanism and has triggered diverse applications where conventional cameras equipped with millions of pixels fail to give an adequate response, including optical microscopy [14]. As a matter of fact, SPI allows imaging at previously undeveloped spectral bands [15,16], at the photon-counting regime [17], in presence of strong turbulence or scattering [18,19], and also through multimode optical fibers [20,21]. The combination of wide-field structured illumination altogether with a bucket detector has made hyperspectral imaging across the visible spectrum possible in a fluorescence microscope [22]. Also, a prototype microscope system based on SPI to image simultaneously in the visible and the short-wave infrared has been recently demonstrated [23].

In SPI the problem of spatial resolution is shifted away from the sensor to a set of a microstructured spatial masks that are codified onto a programmable spatial light modulator. The masks are optically projected onto the sample through the microscope objective and the whole intensity is collected onto a bucket (single-pixel) sensor. Measurements are sequential by changing of the spatial mask. If many different masks are used, their shapes and the intensity signals are combined to retrieve the sample. This generalized mask scanning offers several advantages, like signal-to-noise ratio enhancement and the possibility to reduce the

* Corresponding author.

http://dx.doi.org/10.1016/j.optlaseng.2016.02.004
0143-8166/

acquisition time through compressive sensing, over the traditional raster scan used in confocal microscopy where a single bright pixel is scanned to build up the image [24,25].

The nature of SPI enforces a reciprocal relationship between the frame rate and image size as the time required to capture an image scales with the number of pixels in the image. Two different approaches can be employed to deal with this issue. On the one hand, given some reasonable assumptions about the sparsity of the signal, compressive sensing dramatically reduces the number of measurements well below the number of pixels of the sample [26,27]. What is remarkable here is that with the only "a priori" knowledge about the sparsity of the sample it is possible to get rid off the measurement of the full-length signal, so it saves time. More recently, adaptive sensing has been introduced as a way to circumvent the computational complexity in convex optimization or greedy algorithms used in compressive sensing [23,28,29]. On the other hand, SPI usually relies on the use of fast spatial light modulators such as the digital micromirror device (DMD) to codify the projecting masks. DMDs permit highly flexible codification of binary masks at frame rates above 20 kHz. Extensive application of the DMD to microscopy has been reported in the past few years including conventional SIM microscopy with fringe projection [30], super-resolution and optical sectioning microscopy [31,32] and the programmable array microscope [33–35]. Interestingly, fast DMD and pattern illumination is at the core of optogenetics, a tool for noninvasive activation and silencing of neurons and muscles [36,37].

Along the same lines than SPI microscopy, here we demonstrate a dual-mode microscope that can image specimens in reflection and transmission modes simultaneously. Many specimens, such as biological samples, are weak reflectors but produce transmission images with good contrast. Inversely, other samples are very dense and provide poor transmission images or generate self-shadowing effects. Conventional optical microscope designs make the simultaneous collection of transmitted and reflected light inefficient, restrictive, or even impossible. In general they need different light sources for transmission and reflection, thereby preventing that both images be simultaneously measured in a single sensor. Alternatively they can work with several digital cameras, but then a careful calibration and geometric adjustment of both sensors is necessary. The usefulness of dual-mode microscopy for histopathology studies of skin tissue has been recently reported based on a lensless holographic setup [38,39] and near-field scanning optical microscopy [40].

Here, we demonstrate that the SPI architecture is particularly well-fitted for this dual operation recording both reflection and transmission information simultaneously with a single light source and a simple light sensor configuration constituted by two single-pixel detectors. The field of view, the optical resolution, and the focused plane are determined by the light projection system. Therefore, the reflection and transmission images obtained by each light detector are automatically adjusted geometrically with no need of calibration procedures. Furthermore both images are focused unequivocally to the same plane of the sample. In summary, in our microscope, reflection information complements the transmission one very efficiently, which can be very useful for imaging non-uniform samples and to prevent self-shadowing effects.

For the practical implementation, instead of using a high-end DMD as previous single-pixel microscopy techniques, we use of an off-the-shelf DMD from a cost-effective digital light projector. These devices utilize an offset diamond pixel layout which generates geometrical artifacts. In addition to prove the dual mode operation, in this work we demonstrate an algorithm to precisely allocate pixels in memory to deal with this problem.

2. Dual-mode single-pixel imaging

In a dual-mode SPI microscope, the DMD plane is relayed by a convenient optics onto the sample plane and the forward and backscattered light components are simultaneously collected onto dual single-pixel photodetectors located at the transmission and reflection ports of the microscope, respectively (see Fig. 1). A sequence of M sampling patterns is codified onto the DMD so that the irradiance striking the photodetector at the transmission port in the ith timestep is

$$Y_i = \langle \Psi_i(\vec{x}), T(\vec{x}) \rangle, \tag{1}$$

where $T(\vec{x})$ is the transmittance distribution of the sample, $\Psi_i(\vec{x})$ denotes the ith measurement pattern, and $\langle \Psi_i(\vec{x}), T(\vec{x}) \rangle$ represents the inner product between both functions. The state of the sampling projector $\Psi_i(\vec{x})$ is changed from one timestep to the next to implement a full set of measurements

$$\mathbf{Y} = \mathbf{ST}, \tag{2}$$

where $\mathbf{S}$ is a sensing matrix whose ith row is a one-dimensional reshaping of the ith sampling mask $\Psi_i(\vec{x})$, and $\mathbf{T}$ and $\mathbf{Y}$ are N-dimensional vectors representing a one-dimensional reshaping of the unknown transmittance distribution and the result of the measurements at the transmission port, respectively.

Equivalently, the measurements at the reflection port are concisely represented by the series of linear equations

$$\mathbf{Z} = \mathbf{SR}, \tag{3}$$

where $\mathbf{R}$ and $\mathbf{Z}$ are N-dimensional vectors representing a one-dimensional reshaping of the unknown reflectance distribution and the result of the measurements at the reflection port, respectively,

The problem of the measurement can be stated as: given the result of the measurements $\mathbf{Y}$ and $\mathbf{Z}$ derive the set of values $\mathbf{T}$ and $\mathbf{R}$ that best represent the transmittance and reflectance distributions $T(\vec{x})$ and $R(\vec{x})$ of the sample.

In the easiest implementation of the retrieval algorithm, which is possible for well-conditioned measurements systems, a number of measurements M equal to the number of pixels of the sample is required and both the transmission and the reflection images are retrieved through the inverse matrix as

$$\mathbf{T} = S^{-1}\mathbf{Y}, \quad \mathbf{R} = S^{-1}\mathbf{Z}. \tag{4}$$

Concerning the measurement patterns, various matrices can be employed. For instance, raster-scan style masks stem from the well-known raster-scan technique in which spatial pixels are measured sequentially. Random matrices can also be used in

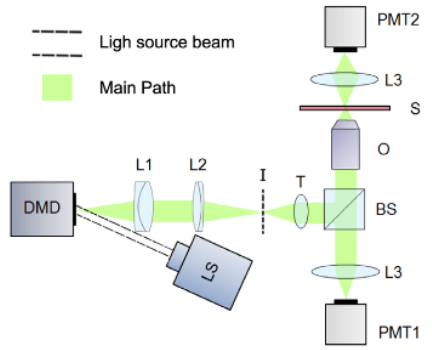

Fig. 1. Experimental set-up. (LS) Light source. (DMD) Digital micromirror device. (L1, L2) Relay lenses. (I) Intermediate image of the DMD. (T) Tube lens. (BS) Beam splitter. (S) Sample plane. (L3) Condenser lenses. (O) Projection objective. Reflection and transmission photomultiplier tubes (PMT1 and PMT2, respectively).

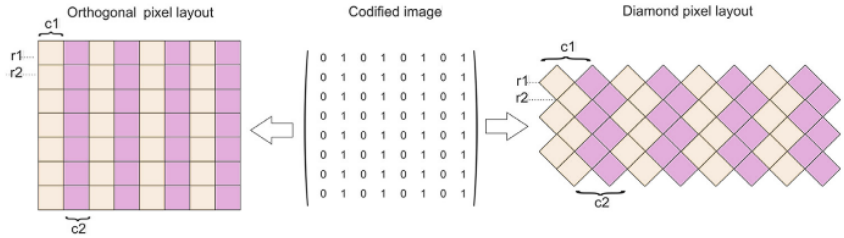

Fig. 2. Graphical representation of the different coordinate systems for orthogonal pixel layout (left) and diamond pixel layout (right).

which each mask has a random distribution of binary values. On the other hand the Hadamard S matrix provides a convenient codification framework because binary nonnegative elements can easily be displayed onto the DMD [41]. The Hadamard S matrix is defined through the equation

$$\mathbf{S}_N = \frac{1}{2}(1 - \mathbf{H}_N), \tag{5}$$

where

$$\mathbf{H}_N \mathbf{H}_N^T = N\mathbf{I}_N \tag{6}$$

with $\mathbf{H}_N$ the Hadamard matrix of order N, $\mathbf{H}_N^T$ the transposed matrix, and $\mathbf{I}_N$ the $N \times N$ identity matrix. Also the above choice provides minimum variance least-squares estimation of the unknown variables. Further, Hadamard measurements obtained by subtracting S-matrix measurements from complementary patterns produce a better result in a similar way to the results achieved through balanced detection [42,43].

2.1. Compressive sensing retrieval

Although there are some benefits of using SPI in optical microscopy, it increases image acquisition time over conventional imaging using focal plane array detectors due to the fact that measurements must be taken sequentially, rather than in parallel. To boost up the image acquisition, we take advantage of the ground-breaking theory of compressive sensing (CS), which makes it possible to recover an N-pixels image from $M < N$ measurements [24,25]. In CS, one takes samples of the N-dimensional transmission vector $\mathbf{T}$ using a matrix $M \times N$ matrix S', obtaining undersampled measurements $\mathbf{Y}' = S'\mathbf{T}$. Along this section, and with no lack of generality, we will refer to the transmission signal, where an identical relation holds for the reflection mode.

Although the above equation defines an underdetermined linear relation with a number of equations lower than the number of variables ($M < N$), the restricted isometry property guarantees that the right signal can still be reconstructed if we simply assume it has a low information content compared with its physical dimensions. In mathematical terms, we assume that the signal is sparse in some basis representation. The problem then becomes how to sample properly with a measurement matrix satisfying certain conditions. For random measurement matrices with independent standard Gaussian entries S', it is known that convex optimization $\min \|\mathbf{T}\|_1$ subject to $\mathbf{Y}' = S'\mathbf{T}$ typically finds the sparsest solution. In the above equation, $\|\cdot\|_1$ denotes the l_1 norm. Yet, there are different methods to retrieve the image such as basis pursuit methods and greedy pursuit methods.

Also, it has been shown that deterministic measurement ensembles exhibit the same behavior than Gaussian matrices via l_1 minimization. Analytically known matrices avoid the need to store the entire matrix as the entries can be computed on the fly and permit to use recovery algorithms with lower complexities. Note that operation at video rates is of paramount significance in applications of SPI in optical microscopy [21,27]. Further, partial Hadamard ensembles where the matrix S' is formed by uniform random selection of M rows of the Hadamard transform matrix allow us to acquire biologically relevant samples [20]. In this case, it is essential to enforce the sparsity of the reconstruction signal in some representation with a high level of dissimilarity with the elements of the measurement matrix.

Because measurements are noisy, it is better to relax the minimization constraints to

$$\min \|\mathbf{T}\|_1 \quad \text{subject to } \|\mathbf{Y}' = S'\mathbf{T}\|_2 < \epsilon,$$

and ask that the fit holds to the noise level ϵ. The full performance analysis of the compressive sensing methodology in terms of the dynamic range of the sensor, the bit depth of the A/D converter, and the amount of noise was conducted in Reference [13].

In our study, we utilized the l_1-magic solver [44] to reconstruct the images with partial Hadamard ensemble to form the measurement matrix. Yet, as the power spectrum of most biological images is generally concentrated at low frequencies, we employed a sampling strategy that favors this frequency range. While this is true, biological samples also have fine details that could be lost due to this sampling strategy. However, in this work, for low frequencies we refer to low Hadamard frequencies, which also include high frequencies in Fourier space.

3. Experimental set-up

In this section we describe how to setup the dual-mode single-pixel microscope by attaching a low-cost commercial DMD and two photodetectors to an inverted microscope. In order to have a low-cost DMD with standard video input control, we remove the optics and the illumination system of an off-the-shelf digital light projector (DLP). We use the illumination system of the commercial microscope and we project the display through the epi-fluorescence port of the microscope and transfer a demagnified image to the sample plane (Fig. 1). The inverted microscope used in the experiment is a Nikon Eclipse Ti-U. The system can be divided in two parts: the illumination system and the collection system. The illumination system is composed by a mercury lamp (Nikon, Intensilight C-HGFI), a DMD (DLP LightCrafter^{TM} EVM 0.3 WVGA), two relay lenses ($\varnothing = 2$ in achromatic doublets, with focal lengths 100 mm (L1) and 200 mm (L2)) producing a 2X magnification, a tube lens and the projection objective (Nikon LU Plan 20X/0.40 WD 13). The DMD is illuminated with a collimated light beam. An intermediate image of the DMD is projected onto the focal plane of the tube lens by the relay lenses and then demagnified by the projection objective onto the sample plane. The two collection systems for reflection and transmission are composed by a condenser lens and a photomultiplier tube PMT (PMM01, Thorlabs Inc.). The reflection PMT is placed in a lateral port and the transmission PMT is placed above the stage of the microscope.

3.1. Pattern codification on diamond shaped DMDs

The direct implementation of an $N \times N$ image onto the diamond pixel layout differs from the implementation onto the conventional orthogonal pixel layout. In an orthogonal layout the rows and the columns are straight lines, so the aspect ratio is preserved. However in the diamond layout meanwhile the rows are straight lines, the columns are zigzag lines. Thereby the direct implementation changes the original aspect ratio of the image. Moreover, straight edges are transformed on zigzag edges. Both consequences are shown in Fig. 2.

To appreciate the effects due to miscoding of the patterns in image retrieval within the framework of SPI, we reconstructed the transmission mode of a negative USAF test chart (USAF 1951 2×2) that was used as a sample in the optical setup of Fig. 1. The number of projected test patterns (Hadamard patterns) was 4096, with a resolution of 64×64 pixels, using no compression techniques. The result is shown in Fig. 3.

To avoid these artifacts, before sending an image to the DMD, the information must be codified in a different way. The aspect ratio could be preserved pre-distorting the original image but this operation do not correct the zigzag edges artifact. In this work a subtler coding is presented that preserves both the aspect ratio and edges of the original image. An example of the operation of our coding algorithm is presented in Fig. 4(a) and (b) for the case of a 2×2 image. Without correction, information codified in a 2×2 array provides a distorted image in the diamond layout as is shown in Fig. 4(a). Our algorithm codifies the information in an array in such way that original image appears rotated but preserves the aspect ratio and straight edges as shown in Fig. 4(b).

The array transformation produced by the algorithm is shown in Fig. 4(c). In general, the algorithm transforms an $N \times N$ image (where N is even) into a $(2N-1) \times N$ array, following the next steps:

1. Diagonals are extracted from the initial image in the order shown in Fig. 4(c).
2. Each row of the $(2N-1) \times N$ image is built by zero-padding each diagonal. The order of the rows matches the order of the extracted diagonals. If the row is even, it is padded to left and right of the diagonal with the same number of zeros. If the row is odd, an additional zero is needed to the left.

In this way, by means of this previous transformation, the coding of a square image is displayed as a square image rotated 45 degrees, preserving the original aspect ratio and edges.

3.2. Temporal multiplexing of binary patterns

Commercial DMDs from video projectors are slower than scientific DMDs created specifically for scientific applications, as they work only at video rates (60–120 Hz). To improve speed performance, we take advantage of the codification procedure used by the DLP for color video projection. In the standard video projection mode, the light changes sequentially to blue, red and green colors. For each color, the display codifies 8 binary patterns. An improvement in speed can be done by codifying 24 binary patterns within a single 24-bit depth image. This technique allows an improvement in speed rate of 24, going from 60–120 Hz to 1440–2880 Hz. A schematic overview of the codification is shown in Fig. 5. The DMD was fully controlled by software designed by our group in Labview™. The image processing was performed using Matlab™.

In Fig. 6 we plot the temporal response of the transmission photomultiplier tube for a single 24-bit image. The patterns projected and the object under measure were the same as in the experiment seen in Fig. 3. Each value for Y_i is obtained by averaging the values within the ranges marked by a red line. Because the number of patterns exceeds the projector's internal memory we have to send the patterns through commercial video stream.

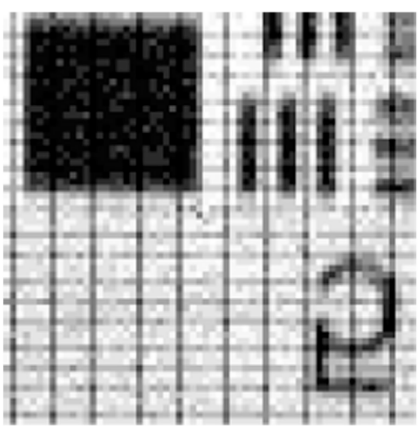

Fig. 3. Experimental image reconstructed without pattern predistortion (64×64 pixels) for the transmission mode. Geometrical artifacts (phantom grid) due to the diamond layout are clearly noticeable.

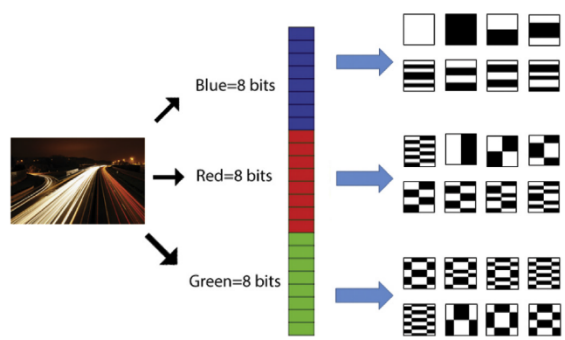

Fig. 5. Codification of a 24-bit image with 24 Hadamard patterns of 1-bit depth. This technique allows an improvement in speed rate of 24, going from 60–120 Hz to 1440–2880 Hz.

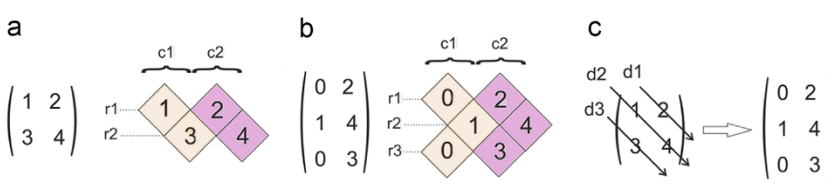

Fig. 4. Graphical representation of the matrix transformation applied to the projected patterns to avoid artifacts.

Through this channel, the video projector repeats each image 6 times (for visual purposes). The maximum speed rate reached was $1440/6 = 240$ Hz, allowing us to capture a 64×64 image (with no compression techniques) in 17 s.

4. Results

With the aim of analyzing the optical resolution in both transmission and reflection modes, a negative USAF test chart (USAF 1951 2×2) is employed as an object in the setup shown in Fig. 1. The microscope objective is a 20x with 0.40 NA. Only the smallest groups of the USAF test, 6 and 7, were used to bound the resolution of the system. The scales and dimensions of the bars are given by the expression $R\,(\mathrm{lp/mm}) = 2^{Group + (element\,-\,1)/6}$. For example, elements 4 and 5 of group 7 have a resolution of 181.0 lp/mm and 203.2 lp/mm, equivalent to a feature size of 2.76 μm and 2.46 μm, respectively. The images were obtained as follows. The patterns of the basis were projected onto the object plane by L1 and O, then the intensity transmitted and reflected by the object for each pattern were captured, simultaneously by the two PMTs. The experimental results are shown in Fig. 7. To boost the sensing stage, compressive sensing algorithms were used. Binning is performed by codifying each pixel of the Hadamard patterns with a group of 4×4 micromirrors in the DMD. Pictures (a) and (b) show transmission and reflection images, respectively, by using only 25% of the total number of patterns ($M = 1012$) for a resolution of 64×64 pixels while (c) and (d) have a 50% compression ($M = 2046$) for the same resolution. Pictures (e) and (f) were obtained by projecting the total number of patterns, without compression ($M = 4092$). The results show that the resolution obtained by transmission and reflection are almost identical (2.46 μm for the images with no compression) and that reducing the projected patterns to 50% does not significantly affect resolution (2.76 μm) but allows measuring twice as fast. These two resolutions values are obtained from the last resolvable element of group 7 (5 and 4, respectively). In our experimental set-up, the PMT can detect light signals at frequencies as high as 20 kHz. However, the acquisition frequency is limited to 60 Hz by the graphic card and, therefore, to 1440 Hz by the frame rate of the commercial grade DMD.

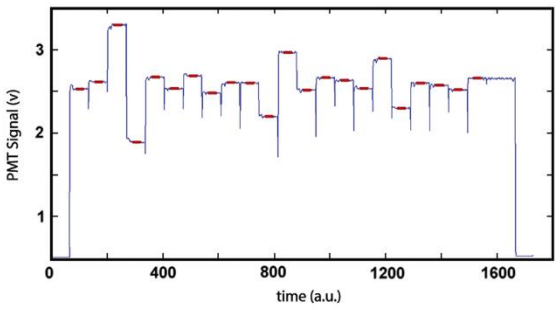

Fig. 6. Photocurrent values for a single 24-bit frame. In the graphic the different values for each 1-bit depth pattern codified in the 24-bit image are shown in red color. In this case, the first and last bits are use as reference. (For interpretation of the references to color in this figure caption, the reader is referred to the web version of this paper.)

The quality of the compressed images was tested using the standard peak signal-to-noise ratio, $PSNR = 10 \log (I_{max}^2/\mathrm{MSE})$, where I_{max} is the maximum pixel intensity value of the reference image and $\mathrm{MSE} = (\frac{1}{N}) \| \mathbf{I}_{ref}^{in} - \mathbf{I}_{rec}^{in} \|^2$, where $\mathbf{I}_{rec}^{in}$ is the undersampled image and $\mathbf{I}_{ref}^{in}$ is the image recovered from the whole measurement. The result of this analysis for the case of the reflection mode

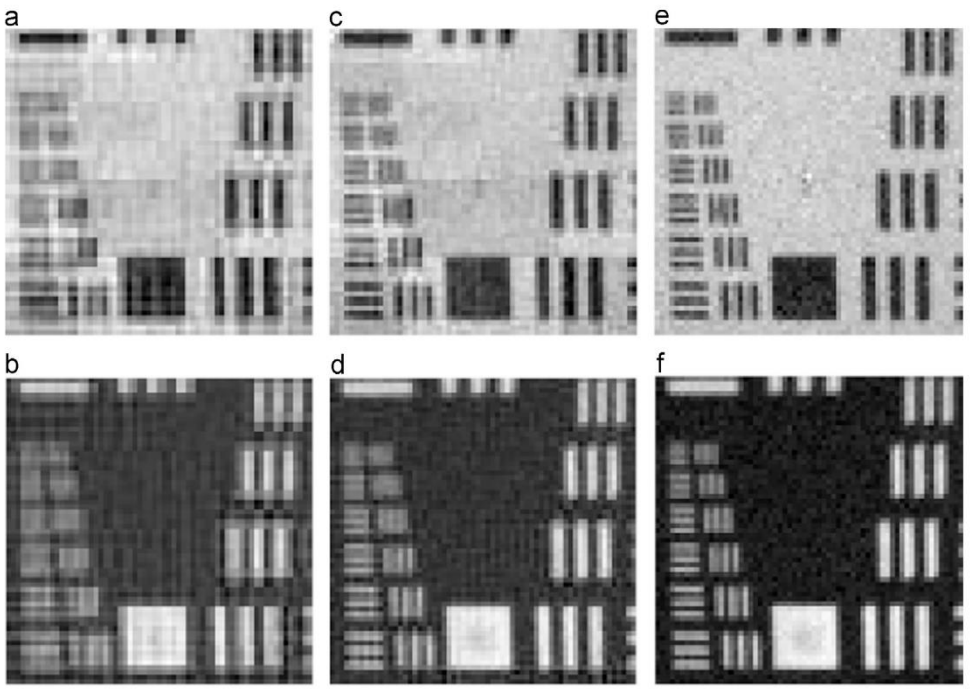

Fig. 7. Experimental images of the USAF test (groups 6 and 7) obtained with the dual-mode single-pixel microscope in Fig. 1 using compressive sensing algorithms with a different compression ratio. Pictures (a) and (b) show transmission and reflection images, respectively, by using only 25% of the total number of patterns for this resolution (64×64 pixels) and 50% (c) and (d) of the whole number of patterns. (e) and (f) Transmission and reflection images with no compression. In all cases, the size of the image was 64×64 pixels and the field of view 192 μm × 192 μm.

is shown in Fig. 8. The figure shows a plot of the PSNR together with the reconstructed image for different compression ratios.

As a proof of concept, we have also tested the capability of the dual-mode SPI microscope to image biological samples with different reflective and transmissive imaging profiles. The results can be seen in Fig. 9. The first row shows images of an *Anaphothrips obscurus* in both reflection (a) and transmission (b) modes taken simultaneously. The images have a resolution of 64×64 pixels ($M = 4096$, binning $= 4 \times 4$ micromirrors) and were obtained with a $20\times$ microscope objective. In this case the transmission image shows only the silhouette of the insect because of its low transparency. The second row shows images of a *Zeuzera pyrina* wing taken with a single-pixel camera in reflection (c) and transmission (d) modes, respectively. Both images have a resolution of 128×128 pixels ($M = 16{,}384$, binning $= 2 \times 2$ micromirrors). In this case, the transmission image shows structures of the other side of the wing (hairs), hidden in the reflection images. The images of both modes are focused to the same plane of the sample and are automatically adjusted geometrically. This can be an advantage for biological structural studies. Image (e) shows the same area of the sample taken in reflection with a CMOS sensor located at the output port of the microscope. This time the resolution of the image is 200×200 pixels.

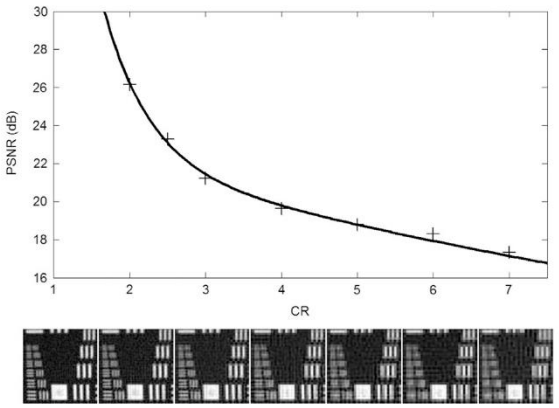

Fig. 8. (Top) Plot of the standard peak signal-to-noise ratio (PSNR) in dB as a function of the compression ratio ($CR = N/M$) to show the quality of the recovered images for the case of the reflection mode. (Bottom) Images reconstructed with the different compression ratios associated with the PSNR plotted in the top figure with increasing CR from left to right.

5. Conclusion

In conclusion, we have developed a dual-mode optical microscope by attaching a commercial DMD and two single-pixel detectors to an inverted microscope. We have designed an algorithm to modify the shape of the projected patterns that improves the resolution and prevents the artifacts produced by the so-called diamond pixel architecture. We have demonstrated that our system is able to retrieve images of reflection and transmission modes with the same field of view and from the same plane of the sample, revealing structures not visible easily by conventional microscopy techniques. This is done with no need of calibration procedures because the field of view, resolution, and focusing plane are controlled exclusively by the properties of the light patterns generated by the optical projection system. By recording transmitted and reflected information loss of data by self-shadowing is minimized which can be advantageous in non-uniform samples containing transparent and opaque regions. Both imaging modes benefit from

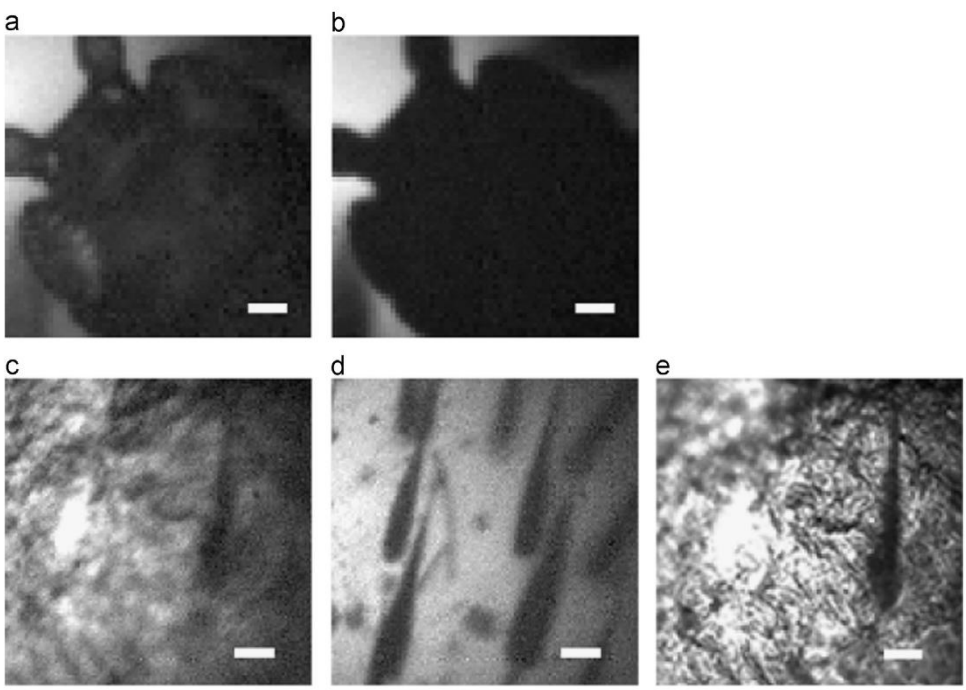

Fig. 9. Experimental results. Anaphothrips obscurus in reflection (a) and transmission (b) modes obtained with the optical setup in Fig. 1 using a $20\times$ objective. The images have 64×64 px. Images of a *Zeuzera pyrina* wing in reflection (c) and transmission (d) modes. In this case the images have a resolution of 128×128 px. (e) Image in reflection taken with a CMOS sensor located at the output port of the microscope. (200×200 px). Scale bar: 25 μm.

the advantages present in single-pixel imaging as low-light sensitivity as well as multidimensional capability through the use of specialized sensors. Single-pixel imaging can also be advantageous in the presence of optical aberrations and optical imperfections in between the sample and the sensor. In our case, this is a clear advantage as the mode of transmission has to go through the entire sample before reaching the sensor. Our system benefits also from the advantages of compressive sensing, reducing the measure time by 50% without strongly affecting the resolution of the system. This fact allows us to configure the system with a compromise between acquisition speed and resolution. Additionally, the simplicity of the detection system will allow us to record different spectral channels or polarization states in each imaging mode very easily, increasing the versatility of the system.

Acknowledgments

This work was supported by MINECO through projects FIS2013-40666-P, the Generalitat Valenciana PROMETEO/2012/021, ISIC/2012/013, and by the Universitat Jaume I P1-1B2012-55. A.D. Rodríguez acknowledges grant PREDOC/2012/41 from Universitat Jaume I. Thanks also to Dr. Tatiana Pina and Dr. Josep Jaques from Universitat Jaume I for providing us the biological samples.

References

[1] Hell SW, Wichmann J. Breaking the diffraction resolution limit by stimulated emission: stimulated-emission-depletion fluorescence microscopy. Opt Lett 1994;19(11):780–2. http://dx.doi.org/10.1364/OL.19.000780.

[2] Betzig E, Patterson GH, Sougrat R, Lindwasser OW, Olenych S, Bonifacino JS, et al. Imaging intracellular fluorescent proteins at nanometer resolution. Science (New York, N.Y.) 2006;313(5793):1642–5. http://dx.doi.org/10.1126/science.1127344.

[3] Moerner WEWE. Single-molecule spectroscopy, imaging, and photocontrol: foundations for super-resolution microscopy (nobel lecture). Angew Chem. (International ed. in English) 2015;54(28):8067–93. http://dx.doi.org/10.1002/anie.201501949 URL ⟨http://www.ncbi.nlm.nih.gov/pubmed/26088273⟩.

[4] Zheng G, Horstmeyer R, Yang C. Wide-field, high-resolution Fourier ptychographic microscopy. Nat Photonics 2013;7(9):739–45. http://dx.doi.org/10.1038/nphoton.2013.187 URL ⟨http://dx.doi.org/10.1038/nphoton.2013.187⟩.

[5] Tian L, Waller L. 3D intensity and phase imaging from light field measurements in an LED array microscope. Optica 2015;2(2):104–11. http://dx.doi.org/10.1364/OPTICA.2.000104.

[6] Prevedel R, Yoon Y-G, Hoffmann M, Pak N, Wetzstein G, Kato S, et al. Simultaneous whole-animal 3D imaging of neuronal activity using light-field microscopy. Nat Methods 2014;11(7):727–30. http://dx.doi.org/10.1038/nmeth.2964 arXiv:1401.5333 URL ⟨http://www.ncbi.nlm.nih.gov/pubmed/24836920⟩.

[7] Ozcan A. Mobile phones democratize and cultivate next-generation imaging, diagnostics and measurement tools. Lab Chip 2014:3187–94. http://dx.doi.org/10.1039/c4lc00010b URL ⟨http://www.ncbi.nlm.nih.gov/pubmed/24647550⟩.

[8] Coskun AF, Ozcan A. Computational imaging, sensing and diagnostics for global health applications. Curr Opin Biotechnol 2014;25:8–16. http://dx.doi.org/10.1016/j.copbio.2013.08.008 URL ⟨http://dx.doi.org/10.1016/j.copbio.2013.08.008⟩.

[9] Gustafsson MG. Surpassing the lateral resolution limit by a factor of two using structured illumination microscopy. J Microsc 2000;198(Pt 2):82–7. http://dx.doi.org/10.1046/j.1365-2818.2000.00710.x.

[10] Gustafsson MGL. Nonlinear structured-illumination microscopy: wide-field fluorescence imaging with theoretically unlimited resolution. Proc Natl Acad Sci U S A 2005;102(37):13081–6. http://dx.doi.org/10.1073/pnas.0406877102.

[11] Allen JR, Ross ST, Davidson MW. Structured illumination microscopy for superresolution. Chemphyschem: Eur J Chem Phys Phys Chem 2014;15(4):566–76. http://dx.doi.org/10.1002/cphc.201301086 URL ⟨http://www.ncbi.nlm.nih.gov/pubmed/24497374⟩.

[12] Saxena M, Eluru G, Gorthi SS. Structured illumination microscopy. Adv Opt Photonics 2015;7:241–75. http://dx.doi.org/10.1364/AOP arXiv:1303.6810 URL https://www.osapublishing.org/aop/abstract.cfm?uri=aop-7-2-241.

[13] Duarte MF, Davenport Ma, Takhar D, Laska JN, Kelly KF, Baraniuk RG, et al. Single-pixel imaging via compressive sampling. IEEE Signal Process Mag 2008;25(2):14–20 URL ⟨http://ieeexplore.ieee.org/lpdocs/epic03/wrapper.htm?arnumber=4472247⟩.

[14] Wu Y, Ye P, Mirza IO, Arce GR, Prather DW. Experimental demonstration of an optical-sectioning compressive sensing microscope (CSM). Opt Express 2010;18(24):24565–78.

[15] Watts CM, Shrekenhamer D, Montoya J, Lipworth G, Hunt J, Sleasman T, et al. Terahertz compressive imaging with metamaterial spatial light modulators. Nat Photon 2014;8:605. http://dx.doi.org/10.1038/nphoton.2014.139 URL ⟨http://www.nature.com/doifinder/10.1038/nphoton.2014.139⟩.

[16] Greenberg J, Krishnamurthy K, Brady D. Compressive single-pixel snapshot x-ray diffraction imaging. Opt Lett 2014;39(1):111–4. http://dx.doi.org/10.1364/OL.39.000111.

[17] van den Berg E, Candès E, Chinn G, Levin C, Olcott PD, Sing-Long C. Single-photon sampling architecture for solid-state imaging sensors. Proc Natl Acad Sci U S A 2013;110(30):E2752–61. http://dx.doi.org/10.1073/pnas.1216318110 arXiv:1209.2262v1 URL ⟨http://www.pubmedcentral.nih.gov/articlerender.fcgi?artid=3725070&tool=pmcentrez&rendertype=abstract⟩.

[18] Tajahuerce E, Durán V, Clemente P, Irles E, Soldevila F, Andrés P, et al. Image transmission through dynamic scattering media by single-pixel photodetection. Opt Express 2014;22(14):16945 URL ⟨http://www.opticsinfobase.org/abstract.cfm?URI=oe-22-14-16945⟩.

[19] Durán V, Soldevila F, Irles E, Clemente P, Tajahuerce E, Andrés P, et al. Compressive imaging in scattering media. Opt Express 2015;23(11):14424. http://dx.doi.org/10.1364/OE.23.014424 URL ⟨http://www.osapublishing.org/viewmedia.cfm?uri=oe-23-11-14424&seq=0&html=true⟩.

[20] Bianchi S, Rajamanickam VP, Ferrara L, Di Fabrizio E, Liberale C, Di Leonardo R. Focusing and imaging with increased numerical apertures through multimode fibers with micro-fabricated optics. Opt Lett 2013;38(23):4935–8. http://dx.doi.org/10.1364/OL.38.004935 arXiv:1405.7548v1 URL ⟨http://www.ncbi.nlm.nih.gov/pubmed/24281476⟩.

[21] Mahalati RN, Gu RY, Kahn JM. Resolution limits for imaging through multi-mode fiber. Opt Express 2013;21(2):1656–68. http://dx.doi.org/10.1364/OE.21.001656 URL ⟨http://www.ncbi.nlm.nih.gov/pubmed/23389151⟩.

[22] Studer V, Bobin J, Chahid M, Mousavi HS, Candes E, Dahan M. Compressive fluorescence microscopy for biological and hyperspectral imaging. Proc Natl Acad Sci U S A 2012;109(26):E1679–87. http://dx.doi.org/10.1073/pnas.1119511109 URL ⟨http://www.pubmedcentral.nih.gov/articlerender.fcgi?artid=3387031&tool=pmcentrez&rendertype=abstract⟩.

[23] Radwell N, Mitchell KJ, Gibson G, Edgar M, Bowman R, Padgett MJ. Single-pixel infrared and visible microscope. Optica 2014;1(5):285–9.

[24] Wilson T. Resolution and optical sectioning in the confocal microscope. J Microsc 2011;244(2):113–21. http://dx.doi.org/10.1111/j.1365-2818.2011.03549.x URL ⟨http://www.ncbi.nlm.nih.gov/pubmed/22004276⟩.

[25] Rodríguez AD, Clemente P, Irles E, Tajahuerce E, Lancis J. Resolution analysis in computational imaging with patterned illumination and bucket detection. Opt Lett 2014;39(13):3888–91 URL ⟨http://www.ncbi.nlm.nih.gov/pubmed/24978763⟩.

[26] Candès EJ, Romberg J, Tao T. Robust uncertainty principles: exact signal reconstruction from highly incomplete frequency information. IEEE Trans Inf Theory 2006;52(2):489–509. http://dx.doi.org/10.1109/TIT.2005.862083 arXiv:0409186.

[27] Donoho DL. Compressed sensing. IEEE Trans Inf Theory 2006;52(4):1289–306. http://dx.doi.org/10.1109/Tit.2006.871582 , arXiv:1204.4227v1 URL ⟨Go to ISI⟩://000236714000001$\$nhttp://ieeexplore.ieee.org/ielx5/18/33885/01614066.pdf?tp=&arnumber=1614066&isnumber=33885.

[28] Aßmann M, Bayer M. Compressive adaptive computational ghost imaging. Sci Rep 2013;3:1545. http://dx.doi.org/10.1038/srep01545 arXiv:1304.0243 URL ⟨http://www.pubmedcentral.nih.gov/articlerender.fcgi?artid=3607834&tool=pmcentrez&rendertype=abstract⟩.

[29] Edgar MP, Gibson GM, Bowman RW, Sun B, Radwell N, Mitchell KJ, et al. Simultaneous real-time visible and infrared video with single-pixel detectors. Sci Rep 2015;5:10669. http://dx.doi.org/10.1038/srep10669 URL ⟨http://www.nature.com/doifinder/10.1038/srep10669⟩.

[30] Fukano T, Miyawaki A. Whole-field fluorescence microscope with digital micromirror device: imaging of biological samples. Appl Opt 2003;42(19):4119–24. http://dx.doi.org/10.1364/AO.42.004119.

[31] Dan W, Lei Dan, Yao Ming, Wang Baoli, Winterhalder Wen, Zumbusch Martin, et al. DMD-based LED-illumination super-resolution and optical sectioning microscopy. Sci. Rep. 3 (2013). http://dx.doi.org/10.1038/srep01116.

[32] Xu D, Jiang T, Li A, Hu B, Feng Z, Gong H, et al. Fast optical sectioning obtained by structured illumination microscopy using a digital mirror device. J Biomed Opt 2013;18(6):060503. http://dx.doi.org/10.1117/1.JBO.18.6.060503 URL ⟨http://www.ncbi.nlm.nih.gov/pubmed/23757041⟩.

[33] Verveer PJ, Hanley QS, Verbeek PW, Van Vliet LJ, Jovin TM. Theory of confocal fluorescence imaging in the programmable array microscope (PAM). J Microsc 1998;189(3):192–8. http://dx.doi.org/10.1046/j.1365-2818.1998.00336.x.

[34] Hanley QS, Verveer PJ, Gemkow MJ, Arndt-Jovin D, Jovin TM. An optical sectioning programmable array microscope implemented with a digital micromirror device. J Microsc 1999;196(3):317–31. http://dx.doi.org/10.1046/j.1365-2818.1999.00602.x.

[35] Martial FP, Hartell NA. Programmable illumination and high-speed, multi-wavelength, confocal microscopy using a digital micromirror. PLoS One 2012;7(8):e43942. http://dx.doi.org/10.1371/journal.pone.0043942 URL ⟨http://journals.plos.org/plosone/article?id=10.1371/journal.pone.0043942⟩.

[36] Sakai S, Ueno K, Ishizuka T, Yawo H. Parallel and patterned optogenetic manipulation of neurons in the brain slice using a DMD-based projector. Neurosci Res 2013;75(1):59–64. http://dx.doi.org/10.1016/j.neures.2012.03.009 URL ⟨http://dx.doi.org/10.1016/j.neures.2012.03.009⟩.

[37] Papagiakoumou E. Optical developments for optogenetics. Biol Cell 2013;105(10):443–64. http://dx.doi.org/10.1111/boc.201200087.

[38] Lee M, Yaglidere O, Ozcan A. Field-portable reflection and transmission microscopy based on lensless holography. Biomed Opt Express 2011;2 (9):2721. http://dx.doi.org/10.1364/BOE.2.002721.

[39] Talaikova NA, Kalyanov AL, Ryabukho VP. Diffraction phase microscopy with transmission and reflection illumination for refractive index measurements, in: Ferraro P, Grilli S, Ritsch-Marte M, Stifter D, editors, SPIE optical metrology, International Society for Optics and Photonics; 2015. p. 95291D. http://dx.doi.org/10.1117/12.2181946 URL ⟨http://proceedings.spiedigitallibrary.org/proceeding.aspx?articleid=2344925⟩.

[40] Wei P-K, Wei C-C, Hsu J-H, Fann W-S. Simultaneous reflection and transmission modes near-field scanning optical microscope. Ultramicroscopy 1995;61 (1–4):237–9 URL ⟨http://www.sciencedirect.com/science/article/B6TW1-3YYV254-17/2/5b72fb980c73b72e2bac8bbae4119f40⟩.

[41] Sloane NJ, Harwit M. Masks for Hadamard transform optics, and weighing designs. Appl Opt 1976;15(1):107–14. http://dx.doi.org/10.1364/AO.15.000107.

[42] Yu W-K, Liu X-F, Yao X-R, Wang C, Zhai Y, Zhai G-J. Complementary compressive imaging for the telescopic system. Sci Rep 2014;4:5834. http://dx.doi.org/10.1038/srep05834 URL ⟨http://www.ncbi.nlm.nih.gov/pubmed/25060569⟩.

[43] Yu W-K, Yao X-R, Liu X-F, Li L-Z, Zhai G-J. Three-dimensional single-pixel compressive reflectivity imaging based on complementary modulation. Appl Opt 2015;54(3):363–7. http://dx.doi.org/10.1364/AO.54.000363 URL ⟨http://ao.osa.org/abstract.cfm?URI=ao-54-3-363⟩.

[44] Candes EJ. l_1−magic. URL ⟨http://users.ece.gatech.edu/justin/l1magic⟩.